EXCIMER LASER TREATMENTS OF IRON, ALUMINUM AND SILICON SUBSTRATES IN NITROGEN AND METHANE ATMOSPHERES

Dissertation
zur Erlangung der Doktorgrades
der Mathematisch-Naturwissenschaftlichen Fakultäten
der Georg-August-Universität zu Göttingen

vorgelegt von
Ettore Carpene
aus Feltre - Italien

Göttingen 2002

D 7

Referent:	PD Dr. Peter Schaaf
Korreferent:	Prof. Dr. Wolfgang Felsch
Tag der mündlichen Prüfung:	17.10.2002

"God created the light, men made it coherent".

EC

Contents

List of Figures

List of Tables

Chapter 1

Introduction

Material processing with laser beams is an expanding field with fascinating physics and attractive technological applications. An increasing number of laser-based treatments have been developed in the last decades: laser cutting [1] and welding [2], laser alloying [3], laser hardening [4] and cladding are few of the numerous examples. Large interest is also addressed to Laser-induced Chemical Vapor Deposition (LCVD, see Ref. [5], ch. 16) and Pulse Laser Deposition (PLD, see Ref. [5], ch. 22) as successful techniques to synthesize polymer films, high temperature superconductors, diamond-like carbon (DLC) and, more generally, metastable compounds. Besides their applications in laser drilling [6] and patterning [7], ultrafast (fs) lasers are nowadays becoming extremely promising for the production of collimated MeV ion beams [8]. Among all branches of laser processing, the irradiation of metals and semiconductors in reactive atmospheres is a relatively new technique. When the reactive gas contains nitrogen, the process is called *laser nitriding*. If a carbon-containing atmosphere is used, the laser treatment is termed *laser carburizing*. Nitriding and carburizing are common methods to improve the mechanical and tribological properties of metals [9]. The incorporation of nitrogen and carbon can be achieved by means of several standard methodologies, such as gas nitriding and carburizing [10, 11, 12, 13, 14], plasma processing [15, 16, 17, 18, 19, 20] and ion implantation [21, 22, 23, 24, 25, 26, 27], just to mention few of them. In the present work, iron, aluminum and silicon substrates have been treated in controlled nitrogen and methane atmospheres with a pulsed excimer laser ($\lambda = 308$ nm, $t_p = 55$ ns), aiming to initiate the reaction between the irradiated target and the atmospheric environment, thus incorporating nitrogen and carbon into the surface layers. The choice of the substrates has been motivated by the many technological applications of the pure materials as well as their nitrides/carbides counterparts. Iron laser nitriding has been the subject of many investigations in the last decade, and it is now well established how the laser can efficiently incorporate a considerable amount of nitrogen (> 30 at.%), leading to enhanced mechanical properties of the surface (see [28, 29, 30, 31] and references therein). Similarly to nitrogen, it will be shown here that also carbon can be successfully incorporated in the iron matrix, if the laser treatment is performed in methane atmosphere. Both aluminum nitride (AlN) and silicon carbide (SiC) have many outstanding properties and numerous structural, physical and thermal similarities, making them perfect candidates for the laser synthesis in reactive atmospheres, as it will be shown in the up-coming chapters. Among the advantages of the laser treatment in reactive atmospheres, the rapidity,

the simple experimental setup and the ability to modify only the surface layer (up to a few microns), leaving the bulk unchanged, should be mentioned. It is therefore an excellent tool for the synthesis of coatings, with the advantage that the modified surface layer is partially originating from the substrate itself, thus enhancing its adhesion to the underlying material. The technological importance of coatings is testified by the large number of conferences and journals dedicated to their characterization [32] and to the synthesis of protective [33, 34], tribological [35] and optoelectronics [36, 37] coatings. From a more general viewpoint, the present work could be allocated in the framework of the photon-induced surface processing that includes all surface treatments and modifications achieved by photon beams. In the following Chapter 2 a brief review on the main properties of the X-N and the X-C systems (X = Fe, Al, Si) will be given, with special attention to the phase diagrams. Chapter 3 will describe the basic physics governing the laser interaction with matter, focusing on the heat equation (section 3.1), the computational procedure (section 3.2) and the phenomena occurring on the surface of the irradiated targets (section 3.3). In Chapter 4 the experimental methods used to investigate the processed samples will be introduced: the specimens preparation and treatment (section 4.1), the Rutherford Backscattering Spectrometry (section 4.2), the Resonant Nuclear Reaction Analysis (section 4.3), the Mössbauer Spectroscopy (section 4.4), the X-ray Absorption Fine Structure (section 4.5), the X-ray Diffraction (section 4.6) and the nanoindentation method (section 4.7). Chapters 5, 6 and 7 will report the experimental results of the laser irradiation respectively of iron, aluminum and silicon substrates in nitrogen and methane gases. In particular, sections 5.1 and 6.1 will focus on the nitrogen mass transport mechanisms in iron and in aluminum, while sections 5.2 and 6.2 will discuss the laser treatment of iron and aluminum in methane. In sections 7.1 and 7.2 the analysis of the silicon substrates irradiated in methane and in nitrogen atmospheres, respectively, will be reported. The conclusions of the work and the outlooks for future developments and investigations will be drawn in Chapter 8.

Chapter 2

Materials properties: structures and phases

The subject of the present work is the laser irradiation of iron, aluminum and silicon substrates in nitrogen and methane atmospheres. As it will be shown, during the laser treatment, nitrogen and carbon are incorporated into the target, leading to the formation of nitrides and carbides. The basic feature of the binary systems X-N and X-C (X = Fe, Al, Si) will be described in the following sections with special emphasis on the features of the phase diagrams. The thermal and physical properties will be reported in Chapter 3, where the laser-material interaction is illustrated.

2.1 The iron-carbon and the iron-nitrogen systems

The Fe-C and the Fe-N binary systems have been extensively studied in the last century, due to their technological importance, especially in metallurgy. Their equilibrium phase diagrams are reported in Fig. 2.1 and Fig. 2.2. Both systems are characterized by the presence of solid solutions as well as stoichiometric compounds. The Fe-C system can be described in terms of the stable graphite or in terms of the metastable Fe_3C (dashed line in Fig. 2.1). The maximum solubility of carbon in α-Fe (bcc) is $\sim$0.1 at.% at 740°C, while it reaches the value of $\sim$9 at.% in γ-Fe (fcc) at 1153°C. The only iron-carbide predicted by the phase diagram is θ-Fe_3C (also known as cementite) that crystallizes in the orthorhombic structure Pnma. Under equilibrium conditions a carbon content higher than 25 at.% leads to the precipitation of graphite in the iron matrix. Other metastable Fe-C phases have been reported in the literature such as Fe_2C (in hexagonal and orthorhombic forms), χ-Fe_5C_2 (also known as Hägg carbide), Fe_7C_3, $Fe_{20}C_9$ and $Fe_{23}C_6$ [38, 39]. The hexagonal ϵ-Fe_xC can exist in a wide compositional range, typically with $2 < x < 6$ [39]. Most of them are considered transition carbides, i.e. during the tempering process of carbon steel the sequence of carbides formation can be described by the following scheme [39]:

$$\text{carbon clusters} \rightarrow \text{ordered } \epsilon \text{ phase} \rightarrow \chi \rightarrow \theta,$$

with cementite being the final product. θ-Fe_3C has great technological importance for the mechanical properties of steels and iron alloys, however it is hard to obtain as a

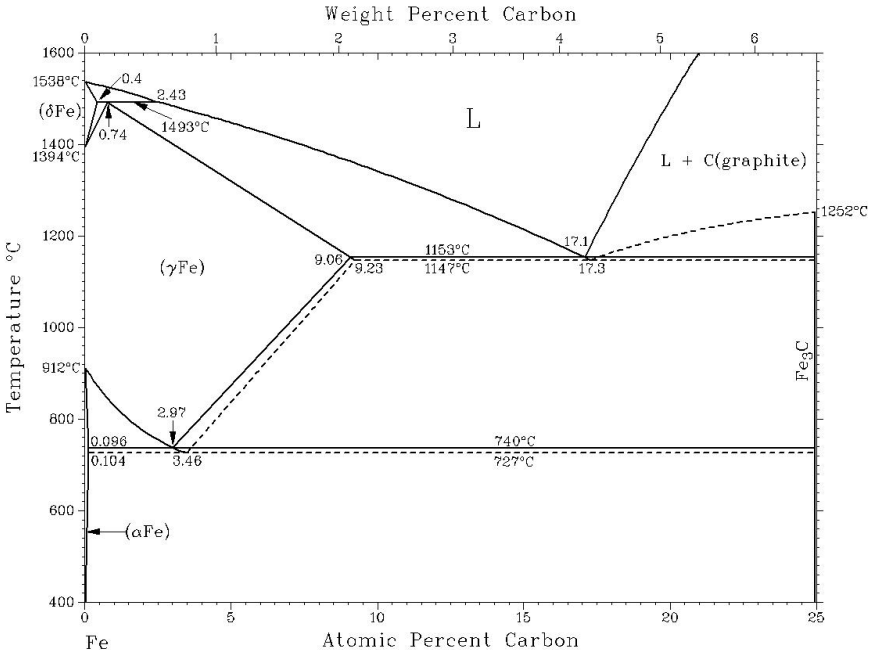

Figure 2.1: The iron-carbon phase diagram [38].

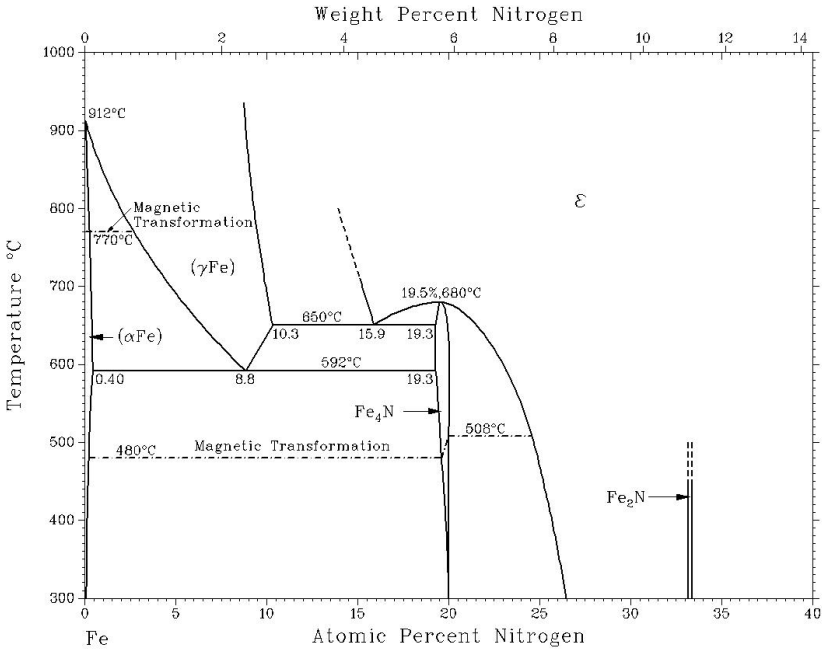

Figure 2.2: The iron-nitrogen phase diagram [38].

single phase, since it is typically embedded in the steel matrix. Due to this difficulty, only few investigations of the θ-Fe_3C electronic structure [40], its mechanical [41] and thermodynamical [42] properties can be found in the literature. Recently, a single-phase cementite film has been prepared by a special Physical Vapor Deposition technique [41], and no other method has yet been successful in synthesizing pure cementite. A thorough review on the iron-carbon system can be found in Ref. [39, 42]. Some crystallographic

Table 2.1: Crystallographic properties of the Fe-C and the Fe-N systems.

Phase	Space group	Lattice constants [Å]			ρ [g/cm^3]	T$_m$ [°C]	T$_b$ [°C]
		a	b	c			
α-Fe	Im3m	2.866			7.86	912$^{(a)}$	
γ-Fe	Fm3m	3.572			8.14	1394$^{(b)}$	
δ-Fe	——— (same as α-Fe) ———					1538	2750
α'-$FeC_{0.042}$	I4/mmm	2.856		2.960	7.47		
ϵ-Fe_2C	$P6_3/mmc$	2.754		4.349	7.19		
θ-Fe_3C	Pnma	5.091	6.743	4.526	7.68	1252	
χ-Fe_5C_2	C2/c	11.560	4.573	5.058	7.60		
Fe_7C_3	$P6_3/mc$	6.882		4.540	7.62		
γ'-Fe_4N	$P\bar{4}3m$	3.795			7.21	680$^{(c)}$	
α"-$Fe_{16}N_2$	I4/mmm	5.720		6.290	7.45		
ϵ-Fe_3N	$P6_322$	2.695		4.362	7.36		
ζ-Fe_2N	Pbnm	5.523	4.830	4.425	7.07	200$^{(d)}$	

$^{(a)}$ Transforms into γ phase.
$^{(b)}$ Transforms into δ phase.
$^{(c)}$ Transforms into ϵ phase.
$^{(d)}$ Dissolves.

and thermal properties are summarized in Table 2.1 (data from [38, 43, 44]). Similarly to carbon, nitrogen atoms occupy interstitial sites in the iron lattice. There are 5 equilibrium solid phases in the Fe-N system [45]: α-Fe(N), γ-Fe(N), γ'-Fe_4N, ζ-Fe_2N and the ϵ phase. In the α-Fe, the maximum nitrogen solubility is $\sim$0.4 at.% at 592°C, but it can reach $\sim$10.3 at.% at 650°C in the γ-Fe. The stoichiometric γ'-Fe_4N phase (also known as roaldite) exists in a narrow region that extends up to 680°C, crystallizing in the cubic $P\bar{4}3m$ structure. The hcp ϵ-Fe_xN phase is stable at elevated pressures and crystallizes with structure similar to the ϵ-Fe_xC carbide in a large compositional range. The existence of the metastable α"-$Fe_{16}N_2$ [39, 42] and the bct martensite phases has been reported as well [39].

2.2 The aluminum-carbon and the aluminum-nitrogen systems

Pure aluminum crystallizes in the fcc structure and has a rather low melting point (660°C), compared to other metals. The incorporation of carbon or nitrogen in the metal leads to a substantial increase of the melting temperature, but the extremely low solubilities of C and N in Al hinder the formation of solid solutions. Instead, stoichiometric compounds are formed. The equilibrium phase diagrams of the Al-C and the Al-N systems are reported in Fig. 2.3 and Fig. 2.4. The only stable aluminum carbide is Al_4C_3 with a melting point of 2173°C and hexagonal crystallographic structure (space group $R\bar{3}m$). The solubility of carbon in aluminum is controversial: the maximum value reported in the literature is

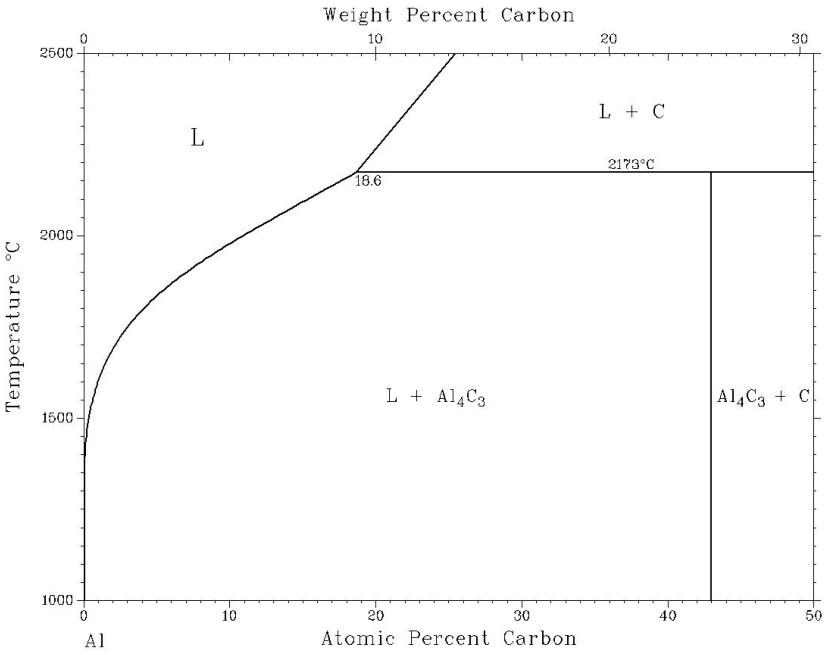

Figure 2.3: The aluminum-carbon phase diagram [38].

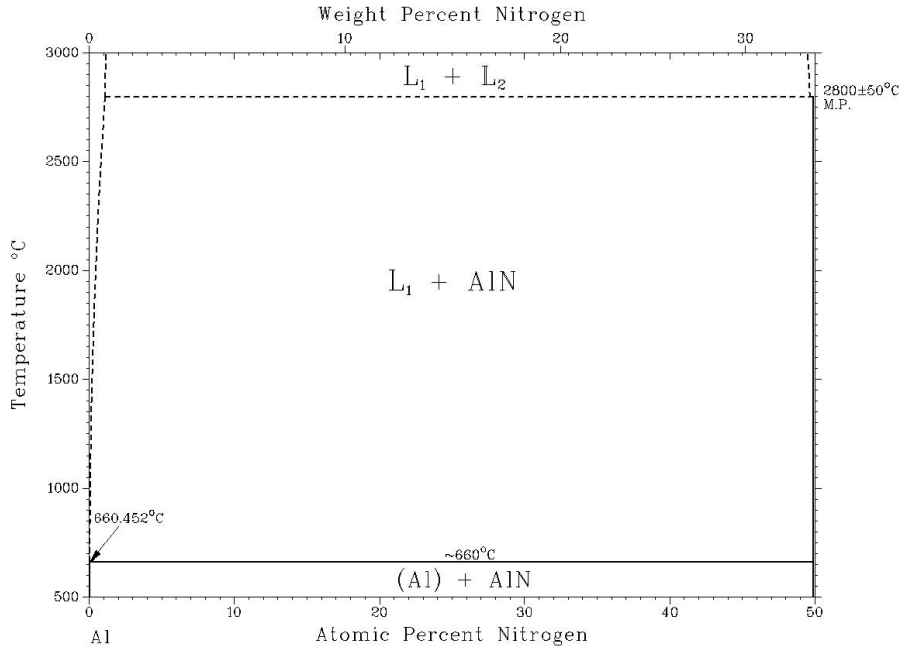

Figure 2.4: The aluminum-nitrogen phase diagram [38].

0.71 at.% (at 1200°C) [46], but it is believed to be unrealistically high [47]. The Al-N phase diagram is primarily qualitative, due to the lack of data on the composition range of the liquid and the solid phases. According to thermodynamic calculations, the solubility of nitrogen in aluminum at its melting point is about 10^{-11} at.%, but it is believed to increase to few at.% at the nitride melting point (2800°C [38]). AlN is known to dissociate at about 2100°C under standard conditions, but the dissociation temperature increases with the ambient pressure [48]. The stable nitride has wurtzite-type structure, transforming into NaCl-type at elevated pressures (several GPa [49]). The basic crystallographic properties

of pure Al, Al_4C_3 and AlN are reported in Table 2.2. AlN has several outstanding physical

Table 2.2: Crystallographic properties of the Al-C and the Al-N systems.

Phase	Space group	Lattice constants [Å]		ρ [g/cm^3]	T_m [°C]	T_b [°C]
		a	c			
Al	Fm3m	4.049		2.70	660	2457
Al_4C_3	$R\bar{3}m$	3.338	24.99	2.97	2173	
AlN (wurtzite)	$P6_3/mc$	3.111	4.979	3.26	2100$^{(a)}$	
AlN (NaCl-type)	Fm3m	4.045		4.11	2100$^{(a)}$	

$^{(a)}$ Dissolves.

properties, that makes it a very attractive material. It has high hardness (10.8 GPa [50]) and resistance to chemicals, high thermal conductivity κ (2 W/cm K at room temperature [43]) and wide band gap (6.2 eV [51]). Besides, the ability to form continuous alloys with GaN and InN opens a wide range of possibilities for tunable optical devices [51, 52].

2.3 The silicon-carbon and the silicon-nitrogen systems

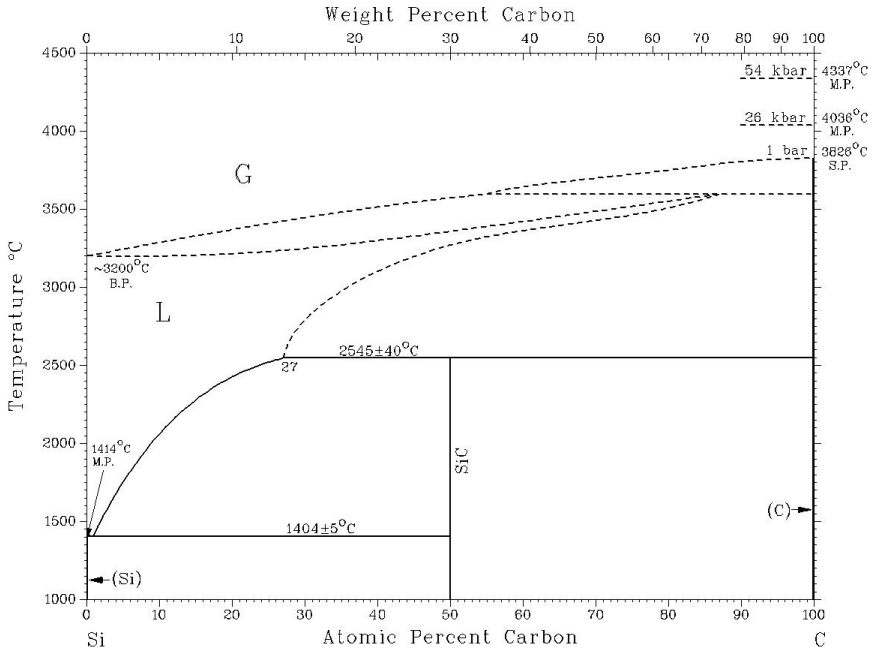

Figure 2.5: The silicon-carbon phase diagram [38].

Silicon is no doubt the most investigated material of the last century. All electronic devices of nowadays life are based on the silicon technology. It is a semiconductor (band gap of 1.12 eV [53]) that crystallizes in the characteristic diamond-type cubic cell. The equilibrium phase diagrams of the Si-C and the Si-N systems are reported in Fig. 2.5 and

Fig. 2.6. The solid solubilities of carbon and nitrogen in silicon are quite low ($\sim 10^{-3}$ at.%

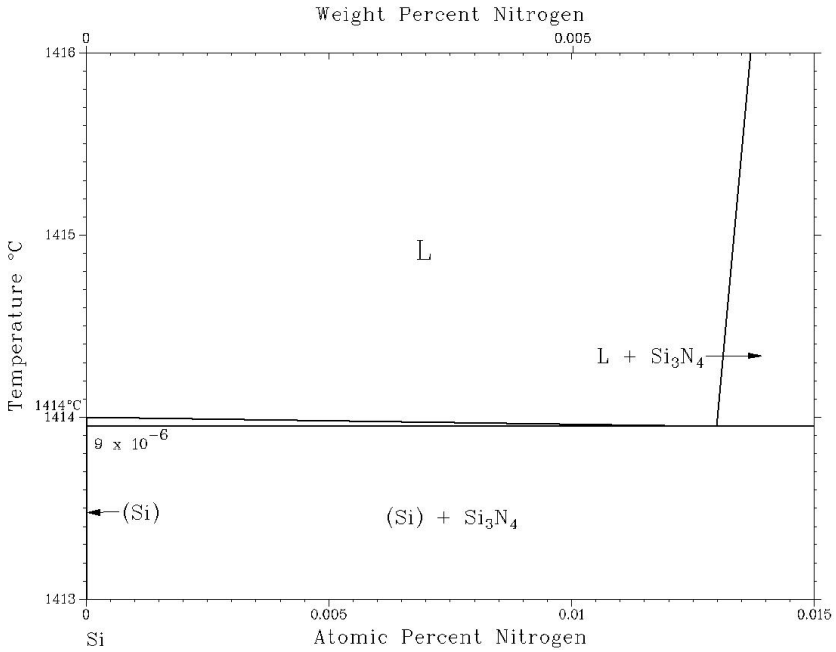

Figure 2.6: The silicon-nitrogen phase diagram [38].

of C at 1300°C and 0.02 at.% of N in liquid Si [38]). Carbon dissolves substitutionally in

Table 2.3: Crystallographic properties of the Si-C and the Si-N systems.

Phase	Space group	Lattice constants [Å]		ρ [g/cm^3]	T_m [°C]	T_b [°C]
		a	c			
Si	Fd3m	5.430		2.33	1410	2355
α-SiC (2H)	$P6_3/mc$	3.081	5.031	3.22	2830$^{(a)}$	
β-SiC (3R)	$F\bar{4}3m$	4.358		3.22	2900	
α-Si_3N_4	P31c	7.754	5.621	3.18	1900$^{(b)}$	
β-Si_3N_4	$P6_3m$	7.604	2.907	3.20	1900$^{(b)}$	
c-Si_3N_4	$Fd\bar{3}m$	7.760		3.93	430$^{(b)}$	

$^{(a)}$ Sublimates.
$^{(b)}$ Dissolves.

silicon, forming the stoichiometric SiC carbide with the hexagonal (α-SiC) or the cubic (β-SiC) structure, the former being less stable at any temperature below the peritectic point (2545°C, 27 at.% of C [38]). The hexagonal carbide is generally termed 2H, 4H or 6H according to the dimension of the lattice parameter c ($\sim$ 5, $\sim$ 10 or $\sim$ 15 Å, respectively). The only nitride phase of the Si-N system is Si_3N_4, existing in three polymorphs: α-Si_3N_4, β-Si_3N_4 (both hexagonal [38, 44]) and the cubic spinel c-Si_3N_4 [54]. The α phase is oxygen-stabilized, although the oxygen content necessary to have a stable compound is controversial [38]. The cubic phase was synthesized recently by laser heating of Si_3N_4 powder in a diamond cell under rather extreme conditions (2000 K, 15 GPa). Its crystallographic space group has been identified by selected-area electron diffraction as $Fd\bar{3}m$

with a lattice parameter of 7.76 Å [54]. Both SiC and Si_3N_4 (in all their polymorphs) are materials with many technological applications. The hexagonal SiC, in particular, is a wide band gap semiconductor (2.9 eV [52]) with an excellent chemical resistance and a high thermal conductivity (5 W/cm K [43]) that makes it attractive for high-temperature semiconductor applications. The crystallographic properties of SiC and Si_3N_4 are reported in Table 2.3.

Chapter 3

Laser interaction with matter

In the following chapter the main feature of the laser interaction with matter will be illustrated. The discussion will focus on the effects of the laser beam on the irradiated target, and the description will be carried out in terms of the one-dimensional heat equation.[1] In order to produce any effect on the material, the laser light must be absorbed. A laser-induced process is thermally activated if the thermalization of the excitation energy is fast compared to the initial processing step (i.e. the pulse duration) [5]. In such a case, the laser treatment is thermal and the laser can be simply considered a heat source. In metals, light is absorbed by the electrons in the conduction band: the time between electron-electron collisions is of the order of 10^{-14} s, while the electron-phonon relaxation time is 10^{-12} to 10^{-10} s [53]. In semiconductors like silicon, similar relaxation times are found for the electron-phonon interaction. In non-metals, interband excitations of electrons can last 10^{-12} to 10^{-6} s [5]. Therefore, for a laser pulse duration of a few tens of nanoseconds ($\sim 10^{-8}$ s), the laser-induced process in metals and semiconductors can be considered a purely thermal process.

3.1 The heat equation

As the laser energy is absorbed, the irradiated sample can undergo structural modifications (incorporation and diffusion of dopants, phase changes, melting, vaporization, etc.) that are correlated to the local temperature. The temperature distribution produced by the absorbed laser radiation can be calculated using the heat equation. In general, the temperature $T = T(\mathbf{r}, t)$ is function of the spatial coordinates $\mathbf{r}$ and the time t. In the absence of heat transport by convection or thermal radiation the heat equation has the following general form:

$$\frac{\rho c_p(T)}{M}\frac{\partial T(\mathbf{r},t)}{\partial t} = -\nabla J_{heat}, \tag{3.1}$$

where ρ [g/cm^3] is the mass density of the target, M [g/mole] is its molar mass, $c_p(T)$ [J K^{-1} mole^{-1}] is its molar specific heat, and J_{heat} includes all the sources of heat flux. For

[1] Terminology note: *fast* pulsed laser beam is refereed to a pulse duration t_p (full width at half maximum) typically in the nanosecond range. The laser beam of energy E is optically focused on an area A of the target, and the *irradiance* I_0 is defined as the power per unit area, i.e. $I_0 = E/At_p$, while the quantity $\phi = E/A$ is called *fluence*, although it is often termed energy density with an abuse of terminology.

the materials investigated in this work and considering that the overall duration of the laser-induced thermal effects is ~ 1 μs (see Fig. 3.2), it can be shown that the thermal diffusion length never exceeds a few μm. Since the dimension of the laser spot is several orders of magnitude larger (~ 5 mm), the one-dimensional approximation along the beam direction $\hat{z}$ (normal to the sample surface) can be used, and Eq. (3.1) becomes:

$$\frac{\rho c_p(T)}{M}\frac{\partial T(z,t)}{\partial t} = -\frac{\partial J_{heat}}{\partial z}. \tag{3.2}$$

The heat flux J_{heat} can be divided into two components: the flux J_{cond} due to the thermal conduction and the flux J_{laser} due to the absorbed laser radiation. The latter is simply:

$$J_{laser} = I_a(z,t), \tag{3.3}$$

with I_a being the portion of the total laser irradiance I_0 [W/cm^2] that is not reflected at the sample surface, and therefore $I_a = I_0(1-R_0)$, where $R_0 = R_0(\lambda, T)$ is the reflectivity of the target for the given laser wavelength λ at the temperature T. According to Beer's law [5],

$$\frac{\partial I_a(z,t)}{\partial z} = -\alpha I_a(z,t), \tag{3.4}$$

where $\alpha = \alpha(\lambda, T)$ is the linear absorption coefficient [cm^{-1}]. The typical value of α in the near UV wavelength range is about 10^6 cm^{-1} for silicon and several metals. Eq. (3.4) describes the attenuation of the laser beam inside the irradiated material and for a finite, temperature-independent α we have:

$$\frac{\partial I_a(z,t)}{\partial z} = -\alpha(1-R_0)I_0(t)e^{-\alpha z}. \tag{3.5}$$

In absorbing media, the reflectivity and the absorption coefficient are related to the complex refractive index $\mathbf{n} = n + ik$ by the following relations [3]:

$$R_0 = \frac{(n-1)^2 + k^2}{(n+1)^2 + k^2}; \tag{3.6}$$

$$\alpha = \frac{4\pi k}{\lambda}. \tag{3.7}$$

The values of R_0 and α, or alternatively n and k, are given in the literature for many pure solids and for a number of compounds in a wide range of laser wavelengths [5, 43]. The time dependence of the laser irradiance $I_0(t)$ is represented by the following analytical expression that matches the experimental pulse shape quite satisfactorily:

$$I_0(t) = \frac{\phi\, t}{\omega^2} e^{-\frac{t^2}{2\omega^2}}, \tag{3.8}$$

with ϕ being the laser fluence [J cm^{-2}], $t_p = 1.6\,\omega$ the pulse duration FWHM and $t \geq 0$. The heat flux due to the thermal conduction is simply:

$$J_{cond} = -\kappa(T)\frac{\partial T}{\partial z}, \tag{3.9}$$

where $\kappa(T)$ [W cm^{-1} K^{-1}] is the heat conductivity of the target as a function of the local temperature. When the solid-liquid phase transformation occurs, the molar latent heat

of melting L_m [J/mole] is an heat sink that must be included in the heat equation. A convenient way is to define a quantity that uniquely describes the state of the material as a function of the temperature [3]:

$$dH(T) = \begin{cases} c_p dT & \text{if } T < T_m; \\ c_p dT + L_m & \text{if } T \geq T_m. \end{cases} \tag{3.10}$$

where T_m is the melting point of the substrate. When the material changes phase, the extra heat sink L_m is "automatically" included in the heat equation. Eqs. (3.3) to (3.10) can be inserted in Eq. (3.2) obtaining the heat equation in the following explicit form:

$$\frac{\rho}{M}\frac{\partial H}{\partial t} = -\frac{\partial (J_{cond} + J_{laser})}{\partial z} = \frac{\partial}{\partial z}\left[\kappa(T)\frac{\partial T}{\partial z}\right] + \alpha(1-R_0)\frac{\phi\, t}{\omega^2} e^{-\frac{t^2}{2\omega^2}} e^{-\alpha z}. \tag{3.11}$$

The surface of the sample is a discontinuity that requires a boundary condition. When the temperature is high enough evaporation can take place, and neglecting the heat losses due to radiation, the average flux j [mole cm^{-2} s^{-1}] of material removed due to the liquid-vapor phase transition can be computed as follows [3]:

$$j = p(T)/\sqrt{2\pi RTM}, \tag{3.12}$$

with R being the gas constant and $p(T)$ the vapor pressure at the surface temperature T. $p(T)$ is obtained from the Clausius-Clapeyron equation [3]:

$$p(T) = p_0 \exp\left[\frac{L_{ev}}{R}\left(\frac{1}{T_b} - \frac{1}{T}\right)\right]. \tag{3.13}$$

where L_{ev} [J/mole] is the molar latent heat of evaporation and T_b the boiling point at the reference pressure p_0. The heat flux due to evaporation is simply:

$$J_{ev} = jL_{ev}, \tag{3.14}$$

leading to the following boundary condition at the target surface:

$$\kappa(T)\left.\frac{\partial T}{\partial z}\right|_{z=0} = J_{ev} = \left.\left(\frac{L_{ev}p_0}{\sqrt{2\pi RTM}} \exp\left[\frac{L_{ev}}{R}\left(\frac{1}{T_b} - \frac{1}{T}\right)\right]\right)\right|_{z=0}. \tag{3.15}$$

As it will be shown in the following sections, during the laser irradiation an enormous pressure ($\sim 10^2$ bar) is acting on the target surface. According to Eq. (3.13) the boiling point is shifted to a higher temperature and the liquid can be heated above T_b, making the transformation described in Eqs. (3.10) unnecessary for the liquid-vapor phase transition. Eq. (3.11) and Eq. (3.15) completely describe the temperature profile in the irradiated sample. Due to the temperature dependence of $\kappa(T)$ and $c_p(T)$ the analytical solution is not always available, and the equations must be solved numerically with the finite differences method [55].

3.2 Computation of the temperature profiles

With the finite differences method, the time t and space z are divided into discrete intervals $t^i = i\ \Delta t$ and $z_j = j\ \Delta z$ (i and j are integer numbers). The partial derivation in time is calculated as follows:

$$c_p(T)\frac{\partial T}{\partial t} = c_p(T_j^i)\frac{T_j^{i+1} - T_j^i}{\Delta t}. \tag{3.16}$$

The space derivative of the heat conduction flux J_{cond} (see Eq. (3.11)) is:

$$\frac{\partial}{\partial z}\left[\kappa(T)\frac{\partial T}{\partial z}\right] = \frac{1}{\Delta z}\left[\left(\frac{\kappa(T_{j+1}^i)+\kappa(T_j^i)}{2}\right)\frac{T_{j+1}^i - T_j^i}{\Delta z} - \left(\frac{\kappa(T_j^i)+\kappa(T_{j-1}^i)}{2}\right)\frac{T_j^i - T_{j-1}^i}{\Delta z}\right]. \tag{3.17}$$

In order to conserve the heat flux and to control the discontinuity points of κ (typically at any phase transition), the average value of κ for two adjacent layers has been used [56]. Since the space is now divided into finite slab, the derivative of the heat flux J_{laser} due to the absorbed laser energy (see Eq. (3.11)) is calculated as the average irradiance absorbed in one slab divided by the slab thickness:

$$\frac{\partial I_a(z,t)}{\partial z} = \frac{\langle I_a(z,t)\rangle|_{\Delta z}}{\Delta z} = \frac{\int_z^{z+\Delta z} I_a(z',t)dz'}{\Delta z} = -\frac{(1-R_0)I_0(t)e^{-\alpha z}(1-e^{-\alpha\Delta z})}{\Delta z}, \tag{3.18}$$

and in terms of finite differences:

$$\frac{\partial I_a(z,t)}{\partial z} = -\frac{(1-R_0)}{\Delta z}\frac{\phi\ i\ \Delta t}{\omega^2}e^{-\frac{(i\ \Delta t)^2}{2\omega^2}}e^{-\alpha(j-1)\Delta z}(1-e^{-\alpha\Delta z}). \tag{3.19}$$

The boundary condition (Eq. (3.15)) is included in the surface layer ($j = 1$):

$$\kappa(T)\frac{\partial T}{\partial z}\bigg|_{z=0} = \left(\frac{\kappa(T_2^i)+\kappa(T_1^i)}{2}\right)\frac{T_2^i - T_1^i}{\Delta z} = \frac{L_{ev}p_0}{\sqrt{2\pi R T_1^i M}}\exp\left[\frac{L_{ev}}{R}\left(\frac{1}{T_b}-\frac{1}{T_1^i}\right)\right]. \tag{3.20}$$

Eqs. (3.10) are implemented in the computation as follows: the temperature of a given layer j at a given time i will be T_j^i. During the heating of the sample, the temperature will increase with increasing time: $T_j^{i+1} \geq T_j^i$. When the melting point is reached $T_j^{i+1} \geq T_m \geq T_j^i$. If the amount of heat $\Delta H = c_p(T_j^i)(T_j^{i+1} - T_m) \leq L_m$, the layer j starts to melt, the new temperature is held to $T_j^{i+1} = T_m$ and the fraction $\Delta H/L_m$ of the slab is molten. On the other hand, if $\Delta H = c_p(T_j^i)(T_j^{i+1} - T_m) > L_m$ the whole slab is molten, the extra heat $\Delta H' = c_p(T_j^i)(T_j^{i+1} - T_m) - L_m$ can be written as $\Delta H' = c_p(T_j^i)(\widetilde{T}_j^{i+1} - T_m)$ and the new temperature of the layer is $\widetilde{T}_j^{i+1} > T_m$. In a similar way, during the solidification we will have $T_j^{i+1} \leq T_m \leq T_j^i$ and the procedure is repeated *mutatis mutandis*, with the proper signs. The melting depth vs. time is easily calculated, since at any time step i, all the layers j satisfying the condition $T_j^i \geq T_m$ are in the liquid phase. The heat equation in finite differences becomes an algebraic equation that can be solved with respect to T_j^{i+1}. Starting with initial condition $T_j^i = 298$ K (room temperature) for every i and j, the temperature is calculated iteratively for each layer at each time step. The values of Δz and Δt are not arbitrarily chosen, but they must satisfy the Neumann criterion [57]:

$$\Delta t < \Delta z^2\left[\frac{\rho c_p(T)}{2\kappa(T)}\right]_{minimum}, \tag{3.21}$$

in order to obtain convergent, physical solutions. The whole computational procedure has been implemented in a FORTRAN computer code using typical values of $\Delta z \sim 10$ nm, and $\Delta t \sim 1$ ps, depending on the thermal properties of the target. Table 3.1 reports the thermal and optical parameters of Fe, Al and Si used in the thermal calculations, while Fig. 3.1 shows the temperature dependence of $\kappa(T)$ and $c_p(T)$ for the pure iron, aluminum and silicon substrates. Fig. 3.2 represents the time evolution of the surface

Table 3.1: Thermal and optical parameters of iron, aluminum and silicon used in the heat equation (data from [43]).

	Fe	Al	Si
M [g/mole]	56	27	28
ρ [g/cm^3]	7.86	2.7	2.33
L_m [kJ/mole]	15	10.5	49.8
L_{ev} [kJ/mole]	350	296	420
T_m [K]	1810	933.5	1685
T_b [K]	3023	2740	2628
R_0 ($\lambda = 308$ nm)	0.53	$0.5^{(a)}$	0.6
α [cm^{-1}] ($\lambda = 308$ nm)	1×10^6	1.5×10^6	1.5×10^6

$^{(a)}$ Measured.

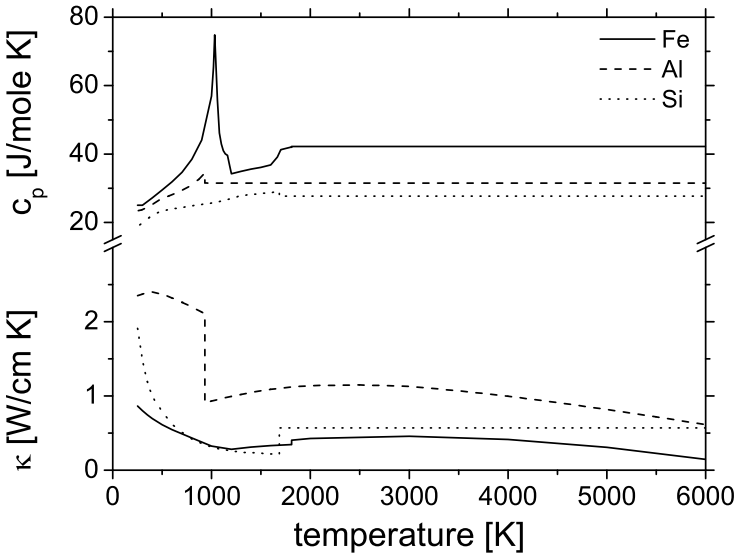

Figure 3.1: Temperature dependence of the molar specific heat (top) and the thermal conductivity (bottom) of iron (solid line), aluminum (dashed line) and silicon (dotted line). Data from [58].

temperature profiles T_1^i and the melting depths of the iron and the aluminum targets irradiated at a laser fluence $\phi = 4$ J/cm^2 with a laser pulse duration $t_p = 55$ ns (XeCl excimer laser). Although it is known that the optical reflectivity R_0 of metals decreases with increasing temperature [3], due to the lack of experimental data, it is assumed temperature-independent. In the case of the silicon substrate, the reflectivity of the solid is about 20% lower than the liquid (for near UV wavelength, $R_0(T < T_m) \simeq 0.6$ and $R_0(T \geq T_m) \simeq 0.75$ [5, 59, 60]) and different temperature profiles are obtained if the temperature dependence of R_0 is taken into account, as illustrated in Fig. 3.3. In particular, when the melting point is reached, the higher reflectivity of the liquid phase reduces the absorbed laser energy, leading to a decrease in the maximum surface

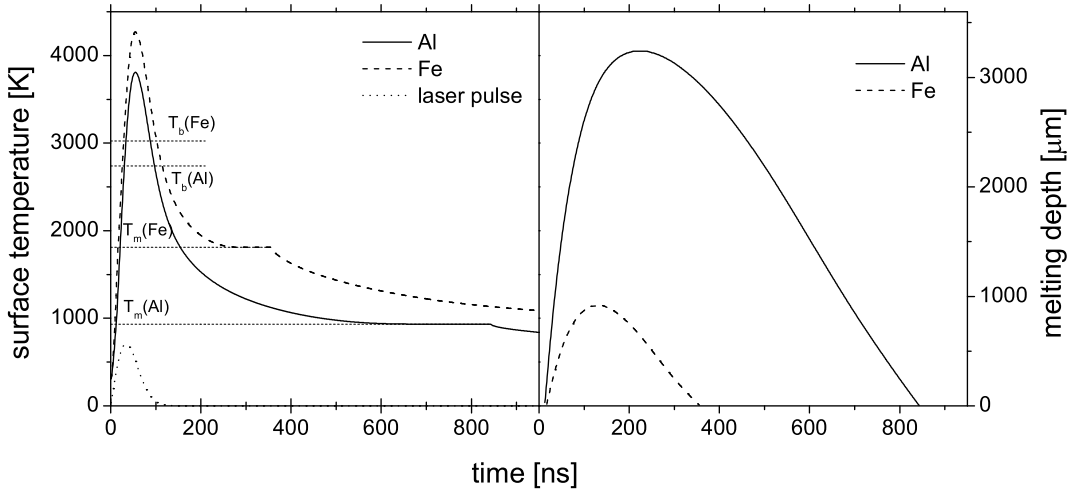

Figure 3.2: Time evolution of the surface temperature profiles (left) and the melting depths (right) of the iron and the aluminum substrates irradiated at 4 J/cm^2. The melting and the boiling points of each element are indicated.

temperature and in the melting time.

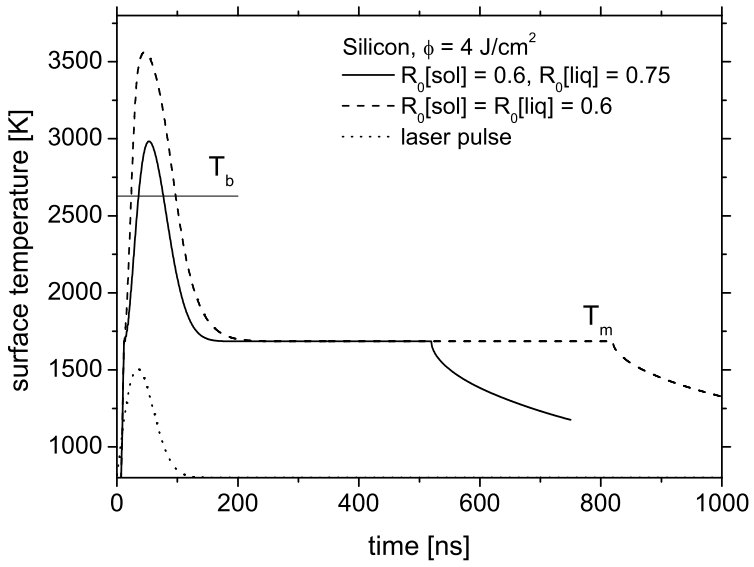

Figure 3.3: Comparison between the Si surface temperature profiles obtained using temperature-dependent (solid line) and temperature-independent (dashed line) reflectivities.

3.3 Phenomena occurring on the target surface

In the previous sections, the temporal evolution of temperature profiles and the related phase transformations *inside* the irradiated substrates have been described, but important phenomena take place also *on* the surface of the target, as illustrated in the following sections.

3.3.1 Vaporization

According to the previous discussion of the heat equation, the laser beam can be absorbed by the substrate causing melting and vaporization. In the case of strong evaporation, typically at fluences of several J/cm^2 and nanosecond pulse duration, the more proper boundary condition at the target surface would be to include the velocity v_{ev} of the evaporation front. Using Eq. (3.12) we can write [5]:

$$v_{ev} = \frac{M}{\rho} j = \frac{p(T)}{\rho} / \sqrt{2\pi RT/M}. \tag{3.22}$$

In the reference frame attached to the liquid-vapor interface moving with velocity v_{ev}, the heat equation Eq. (3.2) becomes:

$$\frac{\rho c_p(T)}{M} \left(\frac{\partial T(z,t)}{\partial t} - v_{ev} \frac{\partial T(z,t)}{\partial z} \right) = -\frac{\partial J_{heat}}{\partial z}. \tag{3.23}$$

Both cases of stationary and non-stationary evaporations can be treated with proper approximations [5], but the correct treatment should consider: (i) the hydrodynamic motion of the evaporated material, (ii) the decrease of the vapor temperature due to its expansion and (iii) the backward flux of the evaporated species. The vaporized atoms/molecules leave the substrate at temperature T_s with half-Maxwellian non-equilibrium velocity distribution (the velocity are initially in the direction normal to the target surface). Due to the collisions with other atoms/molecules, the vapor propagates with hydrodynamic speed v_v and the velocity distribution becomes Maxwellian (i.e. in thermodynamical equilibrium) [61]. The transformation from non-equilibrium to equilibrium distributions takes place in a thin layer of few mean free paths called *Knudsen layer*, as sketched in Fig. 3.4. The detailed mathematical analysis of the transformation was performed by Anisimov [62] with a proper definition of the velocity distribution and using the conservation of mass, momentum and energy across the Knudsen layer. The results show that the temperature T_v of the vapor beyond the Knudsen layer is lower than T_s, due to the partial transformation of thermal energy into kinetic energy of the expanding vapor plume. Besides, the number density of the vaporized species and the vapor pressure behind the Knudsen layer (subscript "v") can be related to the same values within the layer (subscript "s") as follows:

$$\begin{aligned} T_v &= T_s(1 - 0.33\ \Pi); \\ N_v &= N_s(T_s)/(1 + 2.2\ \Pi); \\ p_v &= N_v k_B T_v = p_s(T_s) \frac{1 - 0.33\ \Pi}{1 + 2.2\ \Pi}, \end{aligned} \tag{3.24}$$

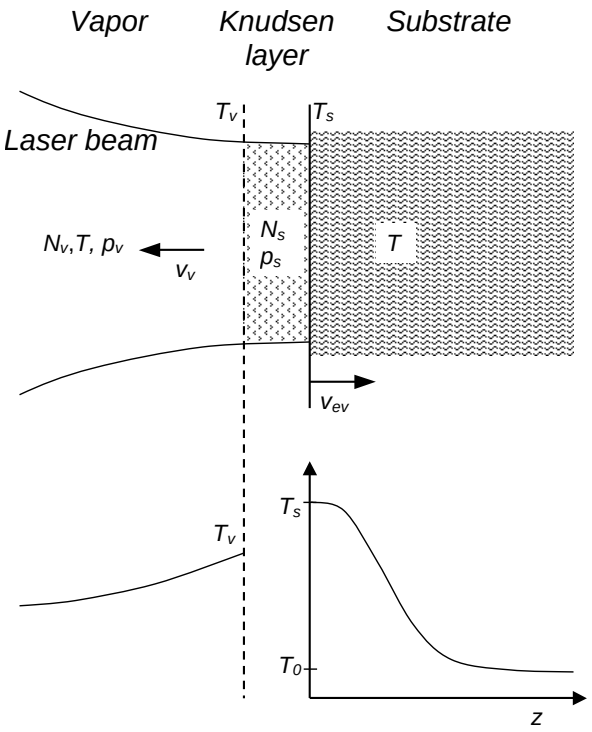

Figure 3.4: Irradiation geometry (top) and temperature profiles within the target and the ambient medium (bottom): effect of the Knudsen layer.

where the *Mach number* Π determines the expansion velocity v_v of the species beyond the Knudsen layer: in general $v_v = \Pi c_s$, where c_s is the speed of sound. For a vapor expanding in vacuum, $\Pi = 1$ [61], but if the laser irradiation takes place in a gaseous medium, Π (with $0 < \Pi < 1$) must be calculated theoretically or measured experimentally [5].

3.3.2 Recondensation

Using Eqs. (3.24) and considering the vapor as an ideal gas, it can be verified that the vapor beyond the Knudsen layer is strongly supersaturated: in fact, $N_v = N_s(T_s)/(1 + 2.2\,\Pi) > N_s(T_v) = p_s(T_v)/k_B T_v$. An example is reported in Fig. 3.5. The ratios $N_v/N_s(T_v)$ and $p_v/p_s(T_s)$ for an iron target at $T_s = 4500$ K are plotted as a function of the Mach number Π. The supersaturation is always present ($N_v/N_s(T_v) > 1$), and it is much stronger for high values of Π (i.e. for low ambient pressures). Therefore, the recondensation of the evaporated species may start beyond the Knudsen layer. Besides, in the presence of a reactive atmosphere, the chemical reaction between the vapor and the ambient gas might lead to the formation and the subsequent condensation of chemical compounds. The pressure acting on the target surface is the pressure inside the Knudsen layer, that is the saturated vapor pressure p_s at the temperature T_s, given by the Clausius-Clapeyron equation (Eq. (3.13)). For an Fe substrate at $T_s = 4500$ K, we have $p_s(T_s) \simeq 10^2$ bar. The dramatic effect of the surface temperature on the saturated vapor pressure is illustrated in Fig. 3.6: the surface temperature profiles of the silicon target already shown in Fig. 3.3 have been used to compute the vapor pressure vs. time according to the Clausius-Clapeyron equation. A moderate increment of the surface temperature

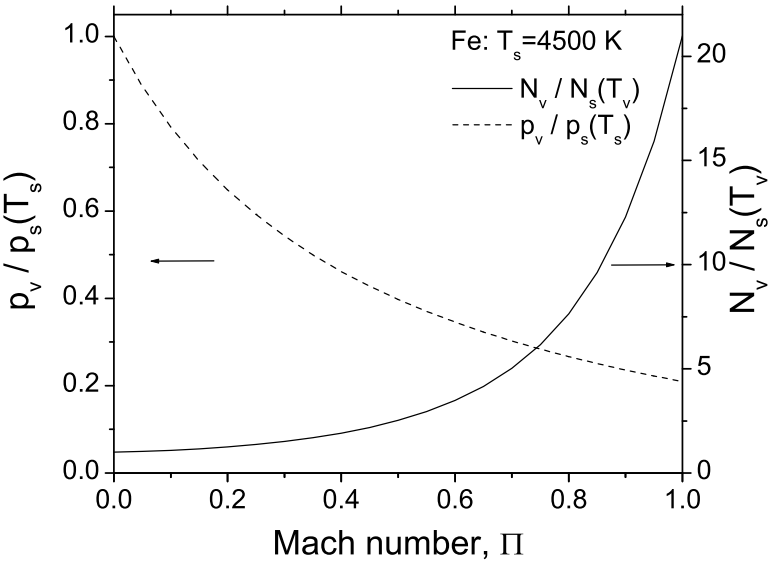

Figure 3.5: Ratios of the vapor pressures within and beyond the Knudsen layer (dashed line) and the densities of the vaporized species obtained from the Anisimov analysis and from Clausius-Clapeyron equation (solid line) as a function of the Mach number.

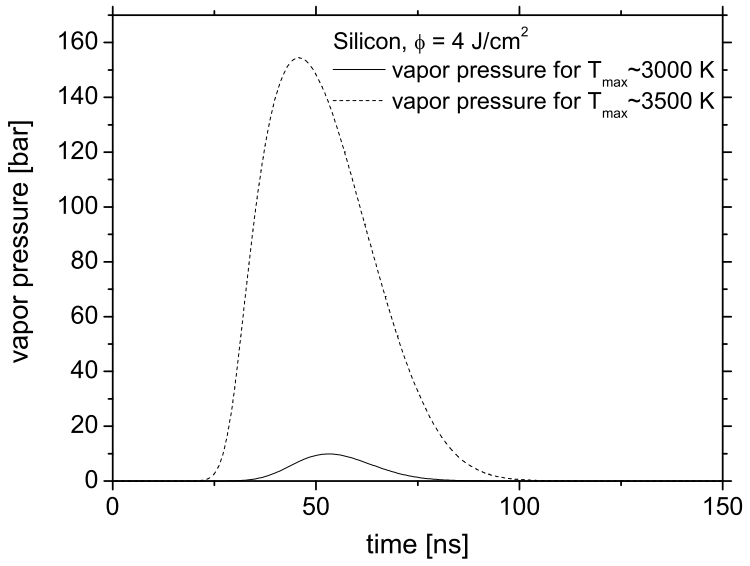

Figure 3.6: Influence of the Si surface temperature on the saturated vapor pressure (the temperature profiles shown in Fig. 3.3 have been used to calculate the vapor pressures).

from 3000 K to 3500 K leads to the enormous increase of the vapor pressure from 10 bar to almost 160 bar.

3.3.3 Plasma formation

When the laser intensity is high enough, the vapor or the ambient gas can become ionized, and properly described as a *plasma*. Within a gas at temperature T_g the collisions between thermal electrons and vaporized species produce a certain degree of ionization given by the Saha equation [5]. The ionized gas strongly absorbs the laser radiation and expands within the laser beam channel, thus shielding the substrate from the laser light. The propagating plasma is generally termed laser-supported absorption wave (LSAW). If the LSAW moves with subsonic velocity with respect to the ambient medium, it is called laser-supported combustion wave (LSCW). As the laser intensity increases, the LSAW can exceed the sound speed becoming a laser-supported detonation wave (LSDW). The typical irradiance necessary to ionize a gas with a free propagating laser (i.e. without any target) is of the order of $10^9 - 10^{11}$ W/cm^2, but it can decrease by several orders of magnitude in front of a solid or liquid target [3, 5]. The theories of LSC and LSD waves have been developed in the '70 [63, 64, 65, 66] obtaining quantitative evaluations of the propagation velocity of the wave front and the pressure behind it. In the case of LSC wave, the laser-light is absorbed within the plasma and dissipated in the ambient medium via heat conduction and thermal radiation. The energy balance can be written as [66]:

$$k^{eff}\Delta T/d = d(\alpha_p I_0 - J^{loss}), \tag{3.25}$$

where k^{eff} is an effective thermal conductivity, α_p is the absorption coefficient of the plasma, ΔT is the temperature jump across the LSC wave, d is the thickness of the wave front, I_0 is the laser irradiance and J^{loss} is the volumetric energy loss [J/cm^3] of the plasma, due to radiation/conduction. Using the heat equation, we obtain [66]:

$$\frac{\rho_p c_p}{M_p}\frac{\partial T}{\partial t} = \frac{\rho_p c_p}{M_p} v_{LSC}\frac{\Delta T}{\Delta x} = v_{LSC}\frac{\rho_p c_p}{M_p}\frac{\Delta T}{d} = k^{eff}\frac{\Delta T}{d^2} \tag{3.26}$$

where ρ_p, c_p and M_p are the mass density, the molar specific heat and the molar mass of the heated gas, while v_{LSC} is the velocity of the wave front. Using Eq. (3.25) in Eq. (3.26) to eliminate d, the LSCW front velocity becomes [66]:

$$v_{LSC} = \frac{M_p k^{eff}}{\rho_p c_p}\sqrt{\frac{\alpha_p I_0 - J^{loss}}{k^{eff}\Delta T}}. \tag{3.27}$$

For intense laser beams ($I_0 \gg J^{loss}/\alpha_p$), we have $v_{LSC} \propto I_0^{1/2}$ and typical values of 10^3 to 10^4 cm/s [3]. On the other hand, if $I_0 \approx J^{loss}/\alpha_p$, we have $v_{LSC} \approx 0$ and the LSCW becomes a stationary wave called *plasmatron* [67, 68]. If the velocity of the propagating wave exceeds the sound velocity of the medium, a supersonic LSD wave is produced. Treating such a wave as a hydrodynamic discontinuity, and using the conservation of mass, momentum and energy, its velocity can be estimated as [63]:

$$v_{LSD} = [2(\gamma^2 - 1)I_0/\rho_0]^{1/3} \propto I_0^{1/3}, \tag{3.28}$$

where γ is the adiabatic coefficient and ρ_0 is the mass density of the ambient gas. The gas pressure behind the wave is [63]:

$$p_{LSD} = \frac{\rho_0\, v_{LSD}^2}{\gamma + 1} \propto I_0^{2/3}. \tag{3.29}$$

For a laser irradiance $I_0 = 72$ MW/cm^2 (i.e. our excimer laser, see next chapter) and considering air in standard conditions ($\rho_0 \approx 1.3$ kg/m^3 and $\gamma \approx 7/5$) as a medium, we obtain $v_{LSD} \approx 10^6$ cm/s and $p_{LSD} \approx 5 \times 10^2$ bar. It is now clear that in both cases of pure vaporization and plasma formation, the pressure acting on the target surface is of the order of 10^2 bar. As already mentioned, this effect rises the boiling point of the target, and the melt can be heated well above T_b. Therefore, the latent heat of evaporation L_{ev} does not play the same role of heat sink as the latent heat of melting L_m, and Eqs. (3.10) are unnecessary for the liquid-vapor phase transition.

Chapter 4

Experimental methods

The following sections describe the experimental details of the samples preparation, samples treatment and analyses via ion beam techniques (Rutherford Backscattering Spectrometry, Resonant Nuclear Reaction Analysis), X-ray techniques (X-ray Absorption Spectroscopy, X-ray Diffraction), Mössbauer Spectroscopy and nanoindentation hardness measurements. Each technique will be described briefly. For more detailed explanations, the specific literature will be reported.

4.1 Samples preparation and laser treatments

Armco iron (purity 99.85%) and aluminum (purity 99.9%) rods have been cut into slices of 1-1.5 mm thickness, mechanically polished with SiC grinding paper (1200, 2400, 4000 mesh) and then with 1 μm diamond paste in order to obtain mirror-like metal surfaces. Single crystalline, boron-doped wafer, <100> and <111> oriented, 0.5 mm thick, have been used as silicon substrates without any further treatment. The laser irradiations have been performed with a Siemens XP 2020 XeCl excimer laser: its basic characteristics are reported in Table 4.1. The samples were placed inside a chamber equipped with a quartz

Table 4.1: Basic features of the Siemens XP 2020 excimer laser.

Parameter	Value
Laser gas	XeCl
Wavelength λ [nm]	308
Maximum pulse energy E_{max} [J]	2
Pulse duration t_p FWHM [ns]	55
Maximum pulse frequency f_p [Hz]	10

window and mounted on a X-Y stage. In order to reduce the oxygen contaminations, the chamber was evacuated to a residual pressure $< 10^{-8}$ bar, and then filled with the desired gas (typically at pressures between 0.1 bar and 10 bar). Natural nitrogen (purity 99.999%) and methane (purity 99.5%) have been used for most of the treatments, but

in some cases the use of isotopic gas was required: ^{15}N enriched nitrogen gas (∼18% enrichment, i.e. 49 times larger than in the natural gas) was used for the detailed analysis of the nitrogen depth profiles by means of Resonant Nuclear Reaction Analysis (more details on the isotopic experiments will be found in the next chapter). The laser beam was focused through a flat-concave quartz lens with focal length of 190 mm, obtaining the so-called raw beam. The distance between the lens and the sample was adjusted in order to irradiate an area A of about 25 mm^2. Since the energy profile obtained with this lens is quite inhomogeneous, leading to a strong convection on the irradiated targets, most of the laser treatments have been performed employing a fly-eye homogenizer lens with focal length of 140 mm. At the optimal distance between the homogenizer and the sample, a square spot of area $A = 5{\times}5$ mm^2 is produced, with minimized surface roughness compared to the raw beam [31]. The laser energy E was measured with a pyroelectric joulemeter and the energy fluence ϕ was determined as $\phi = E/A$ (the area of the laser spot was estimated experimentally with the help of a surface profiler). Since the area A was fixed, the laser fluence was varied changing the laser energy E by means of an additional attenuator (a semitransparent mirror) placed between the laser and the lens: varying the angle between the normal to the mirror and the laser direction, the amount of reflected/transmitted light could be easily modified. The laser experimental setup is sketched in Fig. 4.1. Two kinds of laser treatments have been performed: with the *single*

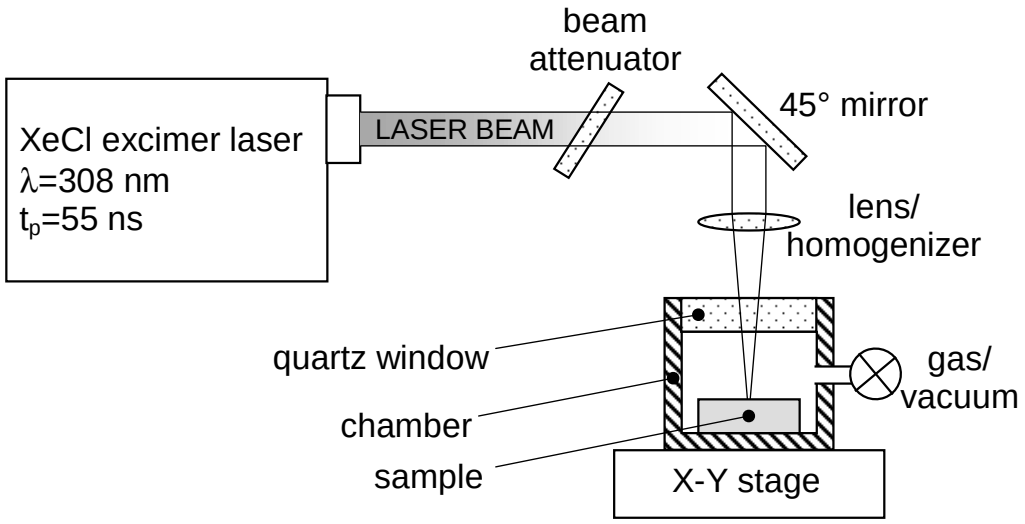

Figure 4.1: Sketch of the laser irradiation experimental setup.

spot irradiation, the same spot on the target was irradiated with the desired number of laser shots (typically from 1 to ∼500); with the *meandering* treatment, the sample was shifted after each laser pulse in such a way that the displacement was a fraction of the spot size. The pictorial explanation is reported in Fig. 4.2: if a is the size of the laser spot, the sample shift $\Delta x = a/n$ in the x direction and $\Delta y = a/m$ in the y direction lead to the meander treatment termed $n \times m$, i.e. each square of area a^2 on the sample surface is irradiated $n \cdot m$ times in toto.

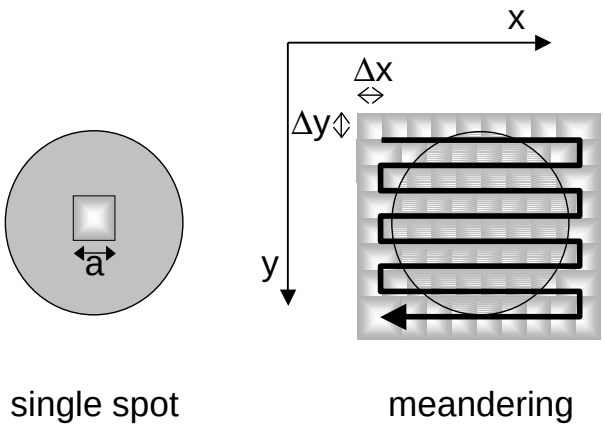

Figure 4.2: Sketch of the single spot and the meandering treatments.

4.2 Rutherford Backscattering Spectrometry

The Rutherford Backscattering Spectrometry (RBS) is based on the elastic scattering of an ion beam (α particles with MeV energy) at the target nuclei. The detection and energetic analysis of the backscattered particles allow to measure the elemental depth profile of the target. The principle of the technique is sketched in Fig. 4.3. All RBS

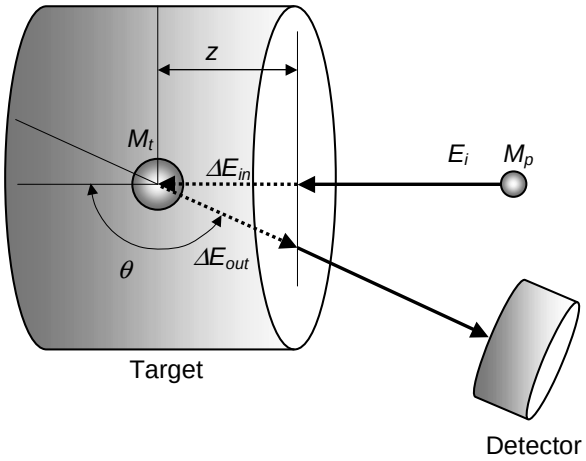

Figure 4.3: Sketch of the RBS experiment.

measurements have been carried out at the IONAS accelerator facility in Göttingen [69]. The α particle beam (M_p=4 amu) with energy E_i of 0.9 MeV is scattered at the target element of mass M_t and detected at a scattering angle θ of 165°. The energy E_i of the incident beam is reduced after the collision by the so called *kinematic factor* $K(M_t, \theta)$ as follows [70]:

$$E_s = K(M_t, \theta)E_i = \left(\frac{M_p \cos\theta + \sqrt{M_t^2 - M_p^2 \sin^2\theta}}{M_p + M_t} \right)^2 E_i. \tag{4.1}$$

If the scattering process takes place at the surface of the probe, the α beam is detected with energy E_s as given by the previous equation. If the scattering process takes place at

a depth z from the surface of the sample, the α beam will loose an amount of energy ΔE_{in} penetrating the sample due to the stopping power of the target. After the scattering, the beam with energy $K(E_i - \Delta E_{in})$ will travel a distance $z/\cos(\pi - \theta)$ in the direction of the target surface, loosing an amount of energy ΔE_{out}, and the α particle will be detected with final energy $E_s(z)$ given by:

$$E_s(z) = K(E_i - \Delta E_{in}) - \Delta E_{out} = K\left(E_i - \int_0^z \frac{dE}{dz}dz\right) - \int_0^{\frac{z}{\cos(\pi-\theta)}} \frac{dE}{dz}dz. \tag{4.2}$$

The quantity $\frac{dE}{dz}$ is called *stopping power* and it represents the energy loss per distance traveled in the target. It is correlated to the *stopping cross section* ε, defined as the energy loss per atom per areal density of the target (usual units eV/10^{15} atoms cm^{-2}) [70]:

$$\varepsilon = \frac{1}{N}\frac{dE}{dz}, \tag{4.3}$$

where N is the atomic density of the target. Since the stopping cross section of a α particle beam is tabulated as function of its energy for all the elements of the periodic table, it can be calculated for any compound A_xB_y according to the Bragg's rule [71]:

$$\varepsilon_{A_xB_y} = x\varepsilon_A + y\varepsilon_B, \tag{4.4}$$

with ε_A and ε_B being the stopping cross sections of the pure elements A and B. The corresponding stopping power to be used in Eq. (4.2) is then:

$$\left(\frac{dE}{dz}\right)_{A_xB_y} = N_{A_xB_y}(x\varepsilon_A + y\varepsilon_B), \tag{4.5}$$

where $N_{A_xB_y}$ is the molecular density of the compound A_xB_y. The probability to detect a backscattered α particle is proportional to the total cross section σ averaged over the solid angle Ω of the detector:

$$\sigma(E_i, \theta) = \frac{1}{\Omega}\int \frac{d\sigma}{d\Omega}d\Omega. \tag{4.6}$$

The quantity $\frac{d\sigma}{d\Omega}$ is called *differential cross section* and it depends on the incident energy E_i of the beam, its scattering angle θ, the masses and the nuclear charges of the atoms involved in the scattering [70]:

$$\frac{d\sigma}{d\Omega} = \left(\frac{Z_pZ_te^2}{4E_i}\right)^2 \frac{4}{\sin^4\theta} \frac{\left[\sqrt{1-(M_p/M_t)^2\sin^2\theta} + \cos\theta\right]^2}{\sqrt{1-(M_p/M_t)^2\sin^2\theta}}. \tag{4.7}$$

Since the target has typically atomic species much heavier than the α particles ($M_p << M_t$) the previous equation can be simplified as follows:

$$\frac{d\sigma}{d\Omega} = \left(\frac{Z_pZ_te^2}{4E_i}\right)^2 \frac{1}{\sin^4(\theta/2)}. \tag{4.8}$$

For a α beam impinging at normal incidence on a uniform target, the total number H of detected particles can be written as [72]:

$$H = \sigma\Omega Q \cdot Nd, \tag{4.9}$$

where Q is the total number of particles hitting the sample, Nd is the number of target atoms per unit area and σ is calculated from Eqs. (4.6) and (4.8). When σ and Ω are known, and the numbers of detected and incident particles are measured, the number of atom per unit area Nd can be determined. Besides, if the atomic density N of the target is known, the physical thickness d can be found. For a multielemental compound A_xB_y, the extension of Eq. (4.9) is straightforward, since

$$H_{A_xB_y} = H_A + H_B, \tag{4.10}$$

where $H_A = \sigma_A \Omega \; Q \cdot \; N_A \; d_A$ and $H_B = \sigma_B \Omega \; Q \cdot \; N_B \; d_B$. Being $N_A = x \; N_{A_xB_y}$ and $N_B = y \; N_{A_xB_y}$, form Eq. (4.10) we obtain [72]:

$$\frac{H_A}{H_B} = \frac{\sigma_A \Omega Q x N_{A_xB_y} d}{\sigma_B \Omega Q y N_{A_xB_y} d} = \frac{\sigma_A x}{\sigma_B y}, \tag{4.11}$$

and the stoichiometric ratio of the compound is readily found:

$$\frac{x}{y} = \frac{H_A \sigma_B}{H_B \sigma_A}. \tag{4.12}$$

Eq. (4.9) and Eq. (4.12) reveal how the RBS is a suitable technique for measuring the depth profile and the elemental composition of the target. An example of a RBS spectrum is reported in Fig. 4.4. A thin Fe film (90 nm) deposited by Physical Vapor Deposition (PVD) on a Si substrate has been analyzed by RBS with a 900 keV He^{++} beam. The

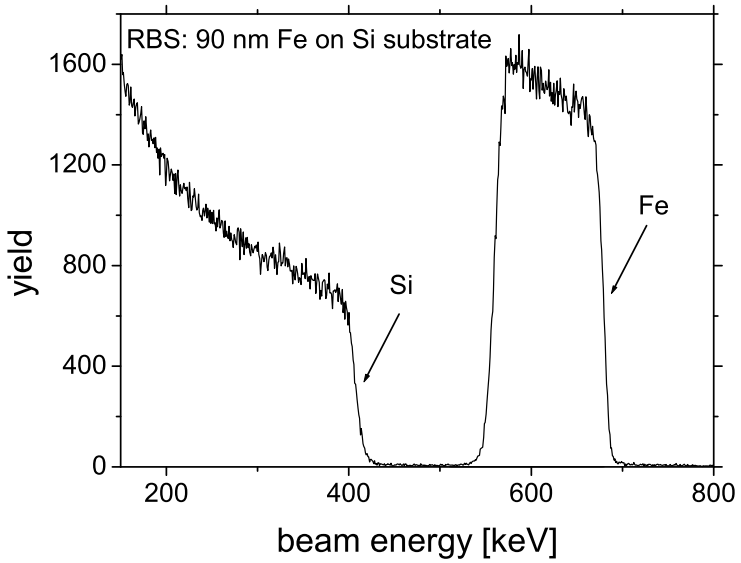

Figure 4.4: RBS spectrum of a thin Fe film (90 nm) deposited on a Si substrate. The arrows indicate the energy positions of the Fe and the Si surface/interface.

depth resolution of RBS is limited by: (i) the energy width of the incident α beam, (ii) the detector resolution and (iii) the energy straggling. The first two contributions are instrumental effects. The beam energy width at the IONAS accelerator has a gaussian

shape with width ω_{beam} depending on the energy and the charge of the accelerated particle: for a 0.9 MeV α beam we have $\omega_{beam} = 79$ eV [69], while the typical energy resolution ω_{res} of a solid state silicon detector is of the order of 12 keV. On the other hand, the beam straggling is a physical effect. As the charged particles traverse the target, the statistical fluctuations of the collision processes produce a spreading of the beam energy. Bohr [73] formulated the beam straggling in the limit of high ion velocity where the energy loss is mostly electronic:

$$\omega_B^2[\mathrm{keV}^2] = 0.26 Z_p^2 Z_t N d[10^{18}\mathrm{at./cm}^2]. \tag{4.13}$$

ω_B^2 is the variance of the energy loss fluctuations. Lindhard and Sharff [74] extended the validity of Eq. (4.13) to beam energies E [keV/amu] below 75 Z_t:

$$\omega_{LS}^2 = \begin{cases} f(E)\omega_B^2 & \text{if } E < 75 Z_t; \\ \omega_B^2 & \text{if } E \geq 75 Z_t, \end{cases} \tag{4.14}$$

with $f(E) = 0.136(E/Z_t)^{1/2} - 0.000064(E/Z_t)^{3/2}$. The total beam energy spreading can be quantified as:

$$\omega_{tot} = \sqrt{\omega_{beam}^2 + \omega_{LS}^2 + \omega_{res}^2} \tag{4.15}$$

and it can be related to the depth resolution Δz using the definition of ε (Eq. (4.3)):

$$\Delta z = \omega_{tot}/\varepsilon N \tag{4.16}$$

The RBS data analysis has been performed with the RUMP code [75], that enables to take into account the stopping cross section, the beam straggling and the detector resolution.

4.3 Resonant Nuclear Reaction Analysis

The Resonant Nuclear Reaction Analysis (RNRA) is a powerful tool for chemical depth profiling, due to its sensitivity to specific isotopes. The principle of the technique is sketched in Fig. 4.5. When the proton beam hits the target containing the isotope of

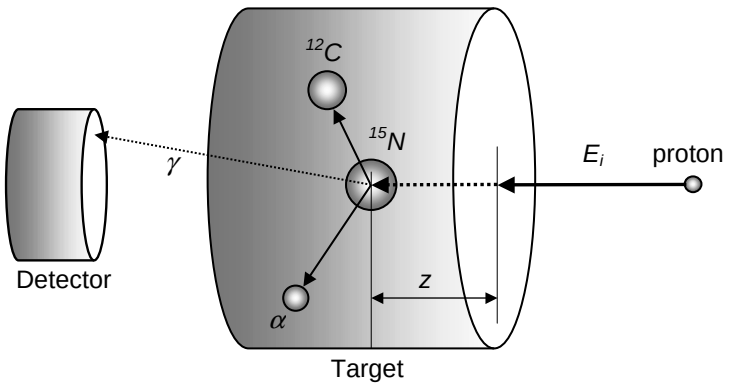

Figure 4.5: Sketch of the ^{15}N(p,$\alpha\gamma$)^{12}C RNRA experiment.

interest, the nuclear reaction can occur, leading to the emission of γ-rays. The photon yield can be used to estimate the average concentration of the corresponding element. If the energy of the analyzing beam corresponds to the energy E_r of a narrow resonance, the

reaction takes place at the surface of the target. At a higher beam energy, the resonant energy E_r is reached at a certain depth z in the target, when the proton has lost the exceeding energy. The γ-ray yield as a function of the incident beam energy E_i (with $E_i \geq E_r$) resembles the concentration depth profile of the isotope. In practice, the yield can be converted into atomic concentration with the use of a calibration sample, and the energy can be converted into depth when the stopping power of the target is known. The nuclear reaction of interest in the present work is ^{15}N(p,$\alpha\gamma$)^{12}C that has been used to measure the nitrogen depth profiles in the laser-irradiated substrates. The main physical properties of the reaction are reported in Table 4.2. In the generic sample of stoichiometry

Table 4.2: Main physical properties of the ^{15}N(p,$\alpha\gamma$)^{12}C nuclear reaction [76].

Reaction	Resonance energy [keV]	γ-ray energy [MeV]	Cross section [mb]	Width [keV]
^{15}N(p,$\alpha\gamma$)^{12}C	429.6	4.43 (100%)	300	0.124

$A_f B_{1-f}$, the element to be profiled is A and its atomic fraction is f (with $0 \leq f \leq 1$). The *normalized* γ-ray yield Y_Q (i.e. the yield Y divided by the number of incident protons Q) of the investigated target is compared with the normalized yield Y_{cal} of the calibration sample containing the same isotope of interest in a known fraction with a known depth profile (a TiN film deposited by magnetron sputtering on a Si substrate has been used). In general, the following relation holds [77]:

$$\frac{f_{cal}}{Y_{cal}\varepsilon_{cal}} = \frac{f}{Y_Q \varepsilon}, \tag{4.17}$$

where f_{cal} is the atomic fraction of the element A in the calibration sample and ε_{cal} is the stopping cross section of the proton beam. Since the atomic fraction f_{cal} is known, ε_{cal} can be calculated with the Bragg's rule (see Eq. (4.4)). The stopping cross section in the sample under investigation can be computed as:

$$\varepsilon = f\varepsilon_A + (1-f)\varepsilon_B = f(\varepsilon_A - \varepsilon_B) + \varepsilon_B, \tag{4.18}$$

with ε_A and ε_B being the stopping cross sections of the pure elements A and B. Inserting Eq. (4.18) in Eq. (4.17) we obtain:

$$\frac{f_{cal}}{Y_{cal}\varepsilon_{cal}} = \frac{f}{Y_Q[f(\varepsilon_A - \varepsilon_B) + \varepsilon_B]}, \tag{4.19}$$

and solving with respect to f, the atomic fraction of the element A as a function of the measured γ-ray yield Y_Q becomes:

$$f = \frac{f_{cal} Y_Q \varepsilon_B}{Y_{cal}\varepsilon_{cal} + f_{cal} Y_Q(\varepsilon_B - \varepsilon_A)}. \tag{4.20}$$

For non homogeneous specimens, the atomic fraction f is a function of the depth z, i.e. $f = f(z)$. In order to have the concentration depth profile, Y_Q (and therefore the atomic fraction f) is measured at various energies $E \geq E_r$ (i.e. various depths):

$$f(E) = \frac{f_{cal} Y_Q(E)\varepsilon_B(E_r)}{Y_{cal}\varepsilon_{cal}(E_r) + f_{cal} Y_Q(E)[\varepsilon_B(E_r) - \varepsilon_A(E_r)]}. \tag{4.21}$$

Since the calibration sample is homogeneous, f_{cal} and Y_{cal} are independent of the beam energy. The energy scale is then converted to depth scale z [in 10^{15} at./cm^2] using the relation (see also Eq. (4.3)):

$$z = \int_{E_r}^{E} \frac{dE'}{\varepsilon(E')} = \int_{E_r}^{E} \frac{dE'}{f(E')[\varepsilon_A(E') - \varepsilon_B(E')] + \varepsilon_B(E')}, \tag{4.22}$$

where Eq. (4.18) has been used to evaluate the stopping cross section in the investigated sample. The stopping cross section of a proton beam in N, Al and Fe are reported as an example in Fig. 4.6 in the energy range 10-1000 keV. In practice, the γ-ray yield

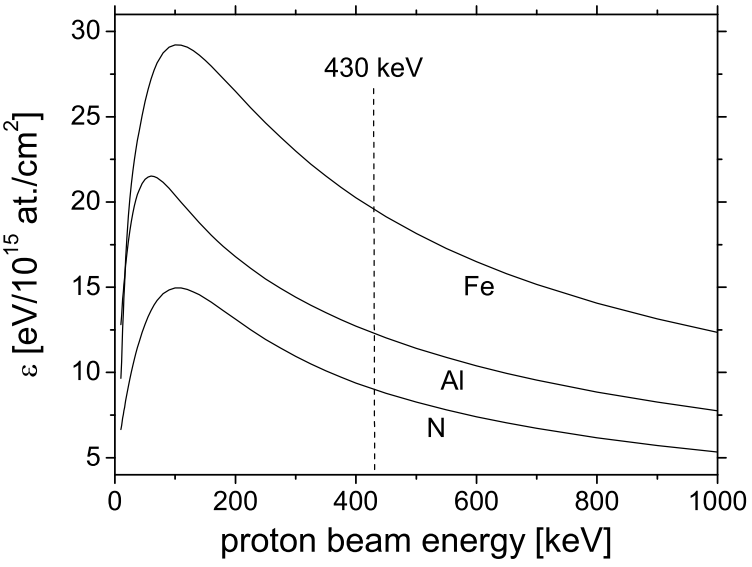

Figure 4.6: Stopping cross sections of a proton beam with 10-1000 keV energy in pure Fe, Al and N (gas). The resonance energy of the ^{15}N(p,$\alpha\gamma$)^{12}C reaction is marked by the vertical dashed line.

is measured at discrete energies E_k (with $E_k \geq E_r$) and the integral in Eq. (4.22) is calculated numerically with the trapezoid rule:

$$z_k = \sum_{j=1}^{k} \frac{(E_{j+1} - E_j)}{2} \left(\frac{1}{\varepsilon(E_{j+1})} + \frac{1}{\varepsilon(E_j)} \right), \tag{4.23}$$

where $E_1 = E_{res}$. Finally, the depth scale can be converted from 10^{15} at./cm^2 to nanometers if the atomic density N[at./cm^3] of the sample is known as a function of f:

$$z[nm] = 10^7 z[10^{15} at./cm^2]/N(f)[at./cm^3]. \tag{4.24}$$

Eqs. (4.18) to (4.24) can be easily implemented in a spreadsheet and the γ-ray yield vs. beam energy $Y_Q(E)$ can be transformed into atomic concentration vs. depth $f(z)$, as shown in Fig. 4.7. A number of factors can affect the depth resolution of the RNRA: (i) the width of the nuclear resonance, (ii) the energy width of the proton beam, (iii) the

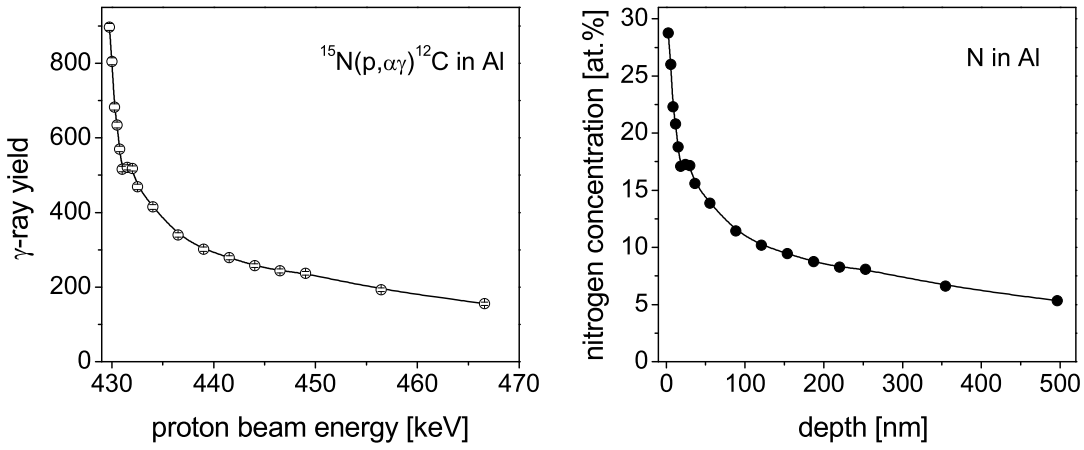

Figure 4.7: Conversion of the γ-rays yield vs. beam energy (left) to nitrogen concentration in aluminum vs. depth (right) according to the procedure described by Eqs. (4.18)-(4.24).

Doppler broadening of the target nuclei and (iv) the proton beam straggling. The cross section width Γ of a given resonance is described by the Breit-Wigner formula:

$$\sigma(E) = \frac{\sigma_0 \Gamma^2}{(E - E_r)^2 + \Gamma^2/4}. \tag{4.25}$$

The energy resolution of a 430 keV proton beam at the IONAS accelerator is $\omega_{beam} = 36$ eV [69]. The Doppler broadening is due to the vibrations of the target atoms and it follows a gaussian law with width ω_D given by [78]:

$$\omega_D = 2.355\sqrt{2M_p E k_B T / M_t}, \tag{4.26}$$

where M_p and E are the atomic mass and the energy of the beam, respectively, M_t is the average atomic mass of the target, T is the temperature and k_B is the Boltzmann constant. During the measurement the sample is typically cooled to liquid nitrogen temperature ($\sim$ 80 K) and the value of ω_D is of the order of 28 eV. The energy straggling ω_{LS} of the proton beam can be described by the Lindhard-Sharff model as already discussed in the previous section (see Eq. (4.14)). The total energy spreading of the proton beam is then:

$$\omega_{tot} = \sqrt{\Gamma^2 + \omega_{beam}^2 + \omega_D^2 + \omega_{LS}^2}, \tag{4.27}$$

and the depth resolution Δz can be written as (see also Eq. (4.16)):

$$\Delta z = \omega_{tot} / \varepsilon(E_r) N(f). \tag{4.28}$$

The values of Δz for a 430 keV proton beam in pure Fe and pure Al targets are reported in Fig. 4.8 as an example.

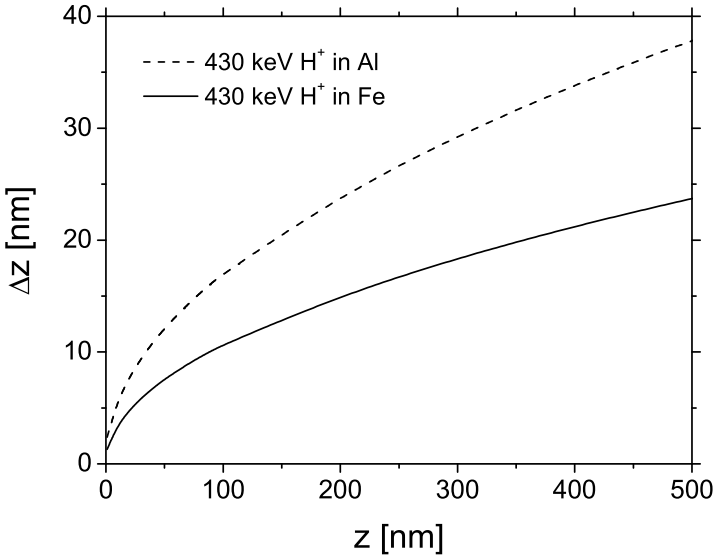

Figure 4.8: Depth resolution of a 430 keV proton beam traversing an aluminum (dashed line) and an iron (solid line) target.

4.4 Mössbauer Spectroscopy

Mössbauer Spectroscopy is based on the resonant absorption of nuclear γ-rays without thermal broadening and without energy loss due to the recoil of the absorbing and the emitting nuclei [79]. An excited nucleus will emit γ-ray with an energy distribution given by the Breit-Wigner law:

$$\sigma(E) = \frac{\sigma_0 \Gamma^2}{(E - E_0)^2 + \Gamma^2/4}, \tag{4.29}$$

where E_0 is the transition energy (14.4 keV for ^{57}Fe) and Γ is the resonance width (4.7×10^{-9} eV for ^{57}Fe). Since the momentum of a γ-ray with energy E_0 is E_0/c, a free emitting atom of mass M would recoil with energy $E_{rec} = E_0^2/2Mc^2$. Nevertheless, if the nucleus is bound in a solid, there is a non-zero probability that the recoil is transferred to the whole solid with mass of the order of $10^{20}M$, making the recoil energy negligible. This is the essence of the Mössbauer effect [80, 81, 82]. The recoil-free fraction f_D of a nucleus emitting or absorbing a γ-ray is given by the Debye-Waller factor [79]:

$$f_{DW} = \exp\left[\frac{-6E_0}{k_B\Theta}\left(\frac{1}{4} + \frac{T^2}{\Theta^2}\int_0^{\Theta/T}\frac{xdx}{e^x - 1}\right)\right], \tag{4.30}$$

with Θ being the Debye temperature of the sample and T its local temperature. The γ-ray energy of a typical Mössbauer transition is so well defined that its Heisemberg width corresponds to an energy shift produced by a Doppler velocity of 1 mm/s. Therefore, the transition energy of a γ-ray source and a γ-ray absorber can precisely match if the energy is modulated by Doppler effect. This turns the Mössbauer effect into spectroscopy. A Mössbauer spectrum consists of a series of γ-ray yield measurements at different relative velocities (i.e. energies) between the source and the absorber. The high energy

resolution allows the detailed measurement of the hyperfine interaction, that is the modification of the nuclear energy levels due to the electric and magnetic fields at the nuclear site. The electrostatic energy due to the interaction between the nuclear charges and the surrounding electrons can be written as [79, 83]:

$$W = \int \rho(\mathbf{r})\phi(\mathbf{r})dV, \tag{4.31}$$

where $\rho(\mathbf{r})$ and $\phi(\mathbf{r})$ are the nuclear charge distribution and electronic potential, respectively. Due to the infinitesimal dimensions of the nucleus, $\phi(\mathbf{r})$ can be written as a Taylor series:

$$\phi(\mathbf{r}) = \phi(\mathbf{0}) + \sum_{i=1}^{3} \frac{\partial\phi}{\partial x_i}\Big|_{\mathbf{0}} x_i + \frac{1}{2}\sum_{i,j=1}^{3} \frac{\partial^2\phi}{\partial x_i \partial x_j}\Big|_{\mathbf{0}} x_i x_j. \tag{4.32}$$

Substituting Eq. (4.32) in Eq. (4.31) with a proper arrangement of all terms and a suitable definition of the reference frame [79], the electrostatic energy becomes:

$$W = \phi(\mathbf{0})Ze + \frac{1}{6}\sum_{\alpha=1}^{3}\phi_{\alpha\alpha}\int \rho(\mathbf{r})r^2 dV + \frac{1}{6}\sum_{\alpha=1}^{3}\phi_{\alpha\alpha}\int \rho(\mathbf{r})(3x_\alpha^2 - r^2)dV, \tag{4.33}$$

with $\phi_{\alpha\alpha}$ being the diagonal terms of the electric field gradient (EFG) tensor and Z the nuclear charge (i.e. the atomic number). The first two terms in the r.h.s. of Eq. (4.33) determine the interaction energy of the so-called isomer shift (IS):

$$E_{IS} = \phi(\mathbf{0})Ze + \frac{1}{6}\sum_{\alpha=1}^{3}\phi_{\alpha\alpha}\int \rho(\mathbf{r})r^2 dV = \phi(\mathbf{0})Ze + \frac{Ze}{6}\langle r^2\rangle \nabla^2\phi, \tag{4.34}$$

with $\langle r^2\rangle$ being the average nuclear radius squared and $\nabla^2\phi$ the trace of the EFG tensor. In Mössbauer spectroscopy, the transition between the nuclear ground state (g) and the excited state (e) with differing nuclear radii is measured. Besides, the chemical environments (and consequently $\nabla^2\phi$) of the source (S) and the absorber (A) are generally different. Using the Poisson equation, $\nabla^2\phi$ can be related to the electronic charge at the nucleus, which in turn, is proportional to the square of the total electron wave function $\Psi(\mathbf{r})$. Therefore the isomer shift δ can be written as:

$$\delta = \frac{Ze^2}{6\epsilon_0}\Big(\langle r_g^2\rangle - \langle r_e^2\rangle\Big)\Big(|\Psi(\mathbf{0})_S|^2 - |\Psi(\mathbf{0})_A|^2\Big). \tag{4.35}$$

The last integral in the r.h.s. of Eq. (4.33) determines the electric quadrupole interaction. The quantity:

$$eQ = \int \rho(\mathbf{r})(3x_\alpha^2 - r^2)dV \tag{4.36}$$

is a traceless tensor that can be related to the nuclear spin states (I,$\widehat{\mathbf{I}}$) using the Wigner-Eckart theorem [83], and the quadrupole energy becomes:

$$\widehat{\mathbf{W}}_{QS} = \sum_{\alpha=1}^{3}\Big[\phi_{\alpha\alpha}\frac{eQ}{2I(2I-1)}\Big(\widehat{\mathbf{I}}_\alpha^2 - \frac{I(I+1)}{3}\Big)\Big]. \tag{4.37}$$

It can be demonstrated that the previous term depends only on the traceless part $V_{\alpha\alpha} = \phi_{\alpha\alpha} - \frac{\nabla^2\phi}{3}$ of the electric field gradient tensor [77]. With a proper choice of the coordination system, we can always have:

$$\Big|V_{zz}\Big| \geq \Big|V_{xx}\Big| \geq \Big|V_{yy}\Big|. \tag{4.38}$$

Defining the *asymmetry parameter* as:

$$\eta = \frac{V_{xx} - V_{yy}}{V_{zz}}, \tag{4.39}$$

Eq. (4.37) becomes [79]:

$$\widehat{\mathbf{W}}_{QS} = \frac{eQV_{zz}}{4I(2I-1)}\Big[3\widehat{\mathbf{I}}_z^2 + \frac{\eta}{2}(\widehat{\mathbf{I}}_+^2 + \widehat{\mathbf{I}}_-^2) - I(I+1)\Big], \tag{4.40}$$

where $\widehat{\mathbf{I}}_+$ and $\widehat{\mathbf{I}}_-$ are the rising and the lowering operators, respectively. For ^{57}Fe, the spins of the ground and the excited states are 1/2 and 3/2, respectively, and only the excited states splits into a doublets with separation ε given by:

$$\varepsilon = \frac{eQV_{zz}}{2}\sqrt{1 + \frac{\eta^2}{3}}. \tag{4.41}$$

In the presence of a magnetic field B at the nucleus, the degeneracy of the nuclear states is broken by the interaction energy $-\mu \cdot \mathbf{B}$, where μ is the nuclear magnetic moment. The state with spin I splits into $2I + 1$ levels with eigenvalues:

$$E_m = -g_N \mu_N m_I B, \tag{4.42}$$

with g_N being the Landé factor, μ_N the nuclear Bohr magneton and $m_I = I, I-1, ..., -(I-1), -I$ the magnetic quantum number. There are 4 level for the excited state and 2 for the ground state of ^{57}Fe, for a total of 8 transitions, but the selection rules $\Delta m_I = 0, \pm 1$ allow only six of them, leading to the characteristic ^{57}Fe Mössbauer sextet of magnetic materials, as shown in Fig. 4.9. The intensity of each transition line depends on the

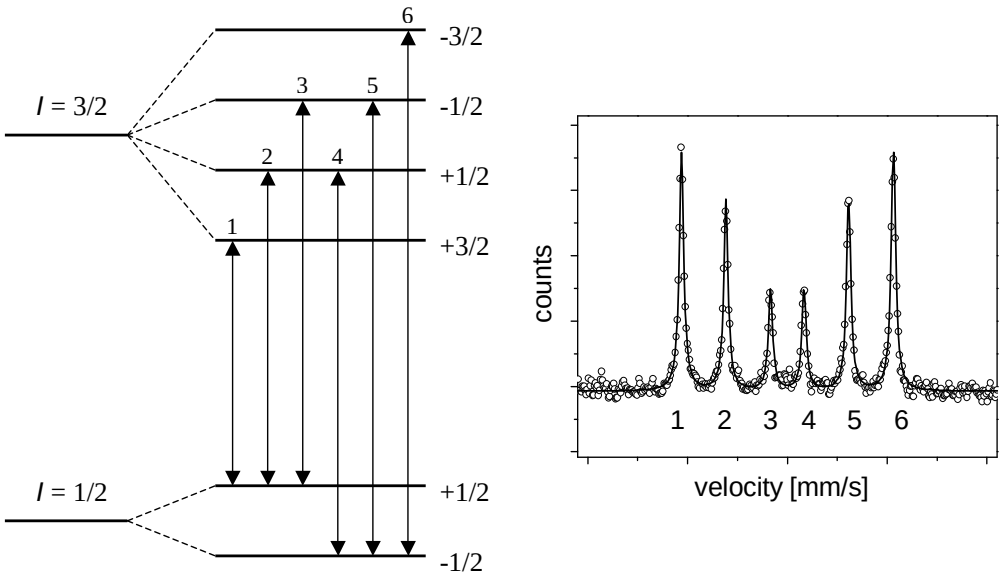

Figure 4.9: Sketch of the ^{57}Fe Mössbauer transitions scheme (left) and typical α-Fe Mössbauer spectrum (right). All the corresponding transition lines are labeled.

angle θ_m between the direction of propagation of the γ-rays and the hyperfine magnetic field as summarized in Table 4.3. The standard fitting routine of the Mössbauer spectra

Table 4.3: Angular dependence of the Mössbauer transition lines.

Transition	Δm_I	Angular dependence
$\pm 3/2 \rightarrow \pm 1/2$	± 1	$3/4(1+\cos^2\theta_m)$
$\pm 1/2 \rightarrow \pm 1/2$	0	$\sin^2\theta_m$
$\mp 1/2 \rightarrow \pm 1/2$	∓ 1	$1/4(1+\cos^2\theta_m)$

is performed using superimposed lorentzian lines, and the fitting parameters are: the line width Γ (Eq. (4.29)), the isomer shift δ (Eq. (4.35)), the quadrupole splitting ε (Eq. (4.41)), the magnetic hyperfine field B (Eq. (4.42)) and the relative intensities of the lines (Table 4.3). The typical geometries of a Mössbauer experiment are sketched in Fig. 4.10. The radioactive ^{57}Co(Rh) source (^{57}Co in Rh matrix, typical activity of

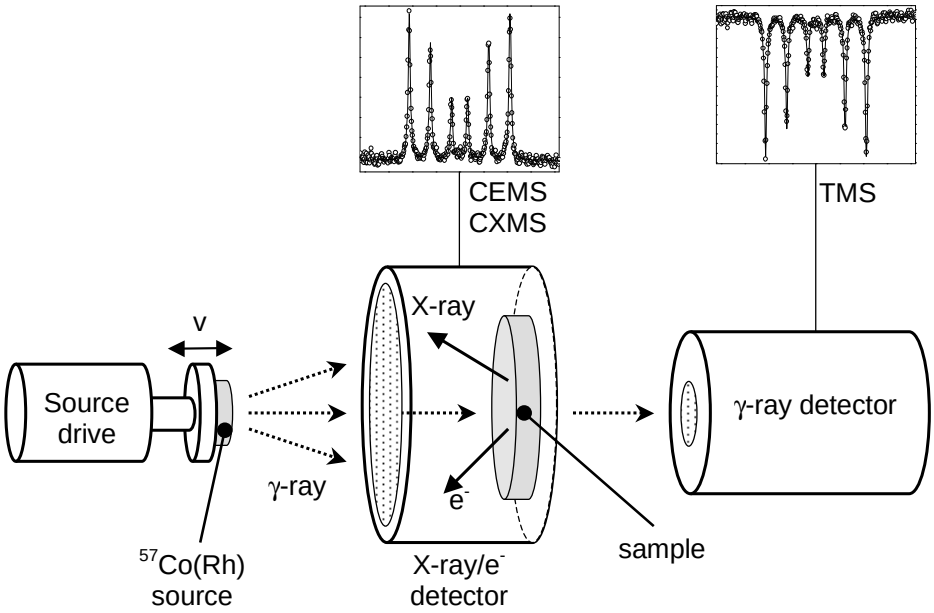

Figure 4.10: Geometries of the transmission (TMS) and the conversion (CEMS-CXMS) Mössbauer experiments.

10 mCi) is mounted on a computer-controlled drive, moving periodically toward and away from the sample with a frequency of the order of 10 Hz. In transmission geometry (TMS) the γ-ray detector is placed behind the sample. The γ-ray yield is recorded in a multichannel analyzer as a function of the source velocity (i.e. the energy modulation). When the velocity is such that the resonant energy is reached, a γ-ray can be absorbed by the sample, and then re-emitted in random direction. Therefore, at the resonant energy, the detector will count fewer photons and the spectral lines appear downward. In backscattering geometry the sample is placed on the bottom of the detector and the conversion phenomenon is used [84]. The photon emitted from an excited nucleus might interact with the inner shell electrons leading to the emission of electrons and X-rays instead of γ-rays. If the detector reveals electron, the technique is named Conversion Electron Mössbauer Spectroscopy (CEMS). When the X-rays are counted, we have the Conversion X-ray Mössbauer Spectroscopy (CXMS). In both cases, more electrons and

X-rays are revealed at the resonant energy and the spectral lines are upward. It should be mentioned that the information depth of CEMS is about 150 nm, while CXMS can reach 10 μm [85].

4.5 X-Ray Absorption Fine Structure

X-ray absorption fine structure (XAFS) refers to the oscillatory structure of the linear X-ray absorption coefficient μ above the absorption edge [86]. The intensity I_0 of a X-ray beam traversing a solid sample decreases exponentially with the penetration depth according to the following law:

$$I(z) = I_0 \exp(-\mu z) \tag{4.43}$$

where μ depends on the nature of the target and in general on the X-ray energy. The absorption coefficient sharply increases when the X-ray energy matches the energy E_c of a inner electronic shell: the abrupt jump of $\mu(E)$ at the energy $E = E_c$ corresponds to the photoexcitation of an electron from the atomic core level with energy E_c. Above the edge E_c some weak wiggles of $\mu(E)$ are observed. These oscillations are characteristic of the emitting sample and they provide a unique signature of the atomic structure of the material. They are interpreted as a quantum interference phenomenon: the outgoing electron of momentum $p = \hbar k$ can be viewed as a quantum oscillation of wavelength $\lambda = h/p = 2\pi/k$ propagating over the solid. This waves can be scattered by the atoms surrounding the emitter, and the amplitude of the reflected waves can add constructively or destructively to the original outgoing wave. The interference pattern changes with the energy of the photoelectron (i.e. with k) and consequently the absorption coefficient will exhibit similar oscillations. A XAFS spectrum consists on the measurement of the X-ray absorption coefficient $\mu(E)$ as a function of the X-ray energy, more specifically the intensities I_0 and $I(z')$ of the incident and the transmitted X-ray beams, respectively, are measured. For a sample of given thickness z' we have:

$$\mu = \frac{1}{z'} \ln \left[\frac{I_0}{I(z')} \right] \tag{4.44}$$

The XAFS spectrum $\chi(E)$ is defined as the normalized, oscillatory part of the absorption coefficient above the edge [87]:

$$\chi(E) = [\mu(E) - \mu_0(E)]/\Delta\mu_0 \tag{4.45}$$

where $\mu_0(E)$ is the smooth, atomic-like component of the absorption coefficient and $\Delta\mu_0$ is a normalization factor (typically the magnitude of the jump at the absorption edge). An example is shown in Fig. 4.11, where the measured absorption coefficient μ, its smooth atomic-like component μ_0 and the extrapolated χ of a crystalline Si sample are reported. Each absorption edge is related to a specific atom and the K-edge is considered in most XAFS experiments. The energies of the K-edge for same elements of interest in this work are reported in Table 4.4. The weak oscillatory structure 30 eV above the edge is generally termed EXAFS (Extended X-ray Absorption Fine Structure) and it contains the information about the local atomic surrounding of the atoms that absorbed the X-ray. In

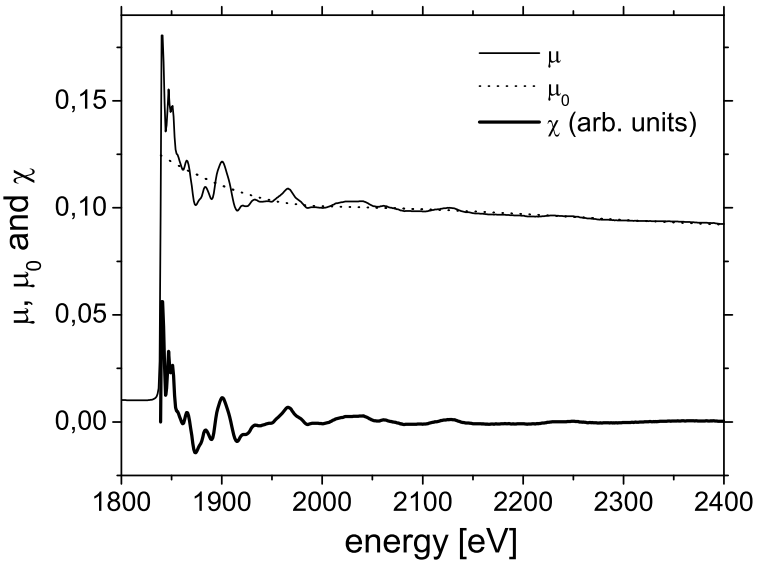

Figure 4.11: X-ray absorption coefficient μ (solid line), the smooth atomic-like component μ_0 (dashed line) and the extrapolated χ (bold solid line) of a crystalline Si sample.

Table 4.4: K-edge energies of carbon, nitrogen, aluminum, silicon and iron.

Element	Atomic number	K-edge energy [eV]
Carbon	6	284.2
Nitrogen	7	409.9
Aluminum	13	1559
Silicon	14	1839
Iron	56	7112

contrast, the region closer to the edge (within the first 30 eV) is known as XANES (X-ray Absorption Near-Edge Structure) and is dominated by the strong multiple scatterings and by the atomic resonances [86]. The experimental data are typically collected in the energy region that goes from a few tens of eV below the edge to several hundreds of eV above the edge in energy step of constant width (e.g. 1 eV). If the X-ray photon has an energy $\hbar\omega > E_c$, the extra energy is transformed into kinetic energy of the emitted photoelectron. Conventionally χ is defined with respect to the photoelectron *momentum* $k = \sqrt{2m(\hbar\omega - E_c)/\hbar^2}$ obtaining $\chi(k)$ instead of $\chi(E)$. The parametrization of the XAFS pattern was formalized by Sayers *et al.* [88] in 1971 and it can be summarized in the following form:

$$\chi(k) = \sum_i A(k)_i N_i \frac{\sin[2kR_i + \delta_i(k)]}{R_i^2} \exp(-2R_i/\eta) \exp(-2k^2\sigma_i^2). \tag{4.46}$$

The index i refers to the atomic shell, and the sum is performed over all shells: N_i are the coordination numbers (i.e. the number of atoms in each shell), R_i are the interatomic

distances (i.e. the radii of the shells), $A_i(K)$ are the scattering amplitudes, $\delta_i(k)$ are phase shifts, η is the XAFS mean free path and σ_i are the average fluctuations of the interatomic bond lengths. From Eq. (4.46) it is clear that the XAFS pattern is given by the superposition of different coordination shells, each oscillating with different amplitude and frequency. In order to analyze the data, it is necessary to isolate each contribution. The standard method is to perform the Fourier Transform (FT) of the pattern. The atomic like part μ_0 of the absorption coefficient is extrapolated from the experimental data using cubic splines or a polynomial fit. Once the $\chi(E)$ is obtained, it is converted to $\chi(k)$ and then Fourier tranformed. Due to the finite data range, the FT can be contaminated by spurious peaks or oscillations. Therefore, the $\chi(k)$ is usually convoluted with a *window* $W(k)$ that smoothly goes to zero at the edges of the k-range. Besides, the data are weighted with some power of k (k^n, with $n = 1$, 2 or 3) to compensate the decay of the waves at large values of k. The FT is thus performed as follows [87]:

$$\tilde{\chi}(R) = \int_{k_{min}}^{k_{max}} e^{-ikr} W(k) k^n \chi(k) dk \tag{4.47}$$

Each peak of $\tilde{\chi}(R)$ represents a shell contribution. The position of the peaks is related (but not equal) to the radius of the shells, and the intensity of the peaks reflects the number of atoms in the shell. The quantitative analysis is performed selecting one or few adjacent

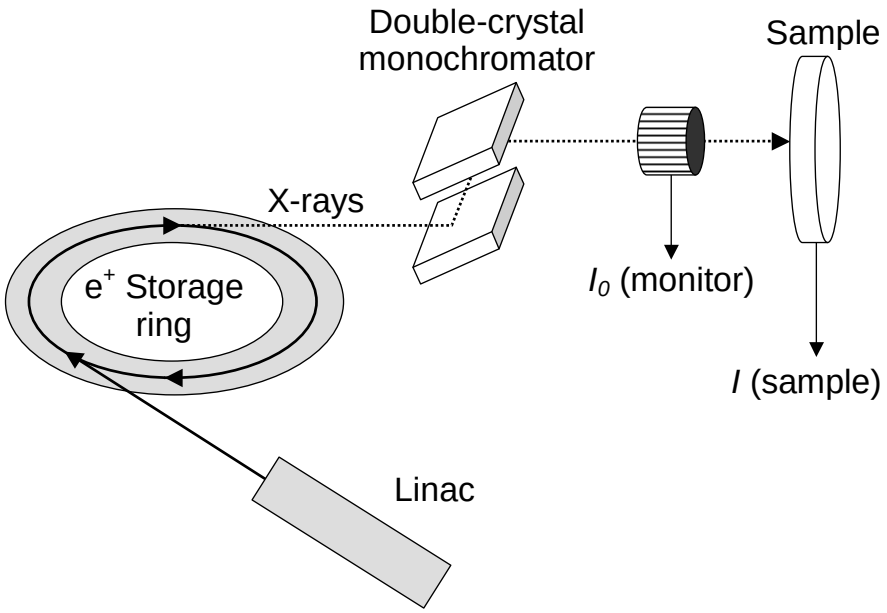

Figure 4.12: Sketch of the L.U.R.E. SA32 beamline experimental setup.

peaks and calculating the back Fourier transform (BFT). The corresponding oscillations in the k-space are then fitted according to Eq. (4.46), in order to obtain the values of the coordination number N_i, the interatomic distance R_i and the disorder parameter σ_i of each shell. The scattering amplitudes A_i and the phase shifts δ_i are entered as initial parameters. They are calculated with the help of dedicated softwares [89] or obtained experimentally from the analysis of calibration samples. Similarly to Mössbauer spectroscopy, the XAFS data can be collected in transmission geometry, where the incident and the transmitted X-ray intensities are compared, or in backscattering geometry where the emitted photoelectrons are detected. The latter is called *total electron yield* (TEY)

mode. The XAFS technique has been employed to analyze the silicon substrates irradiated in nitrogen and in methane atmospheres. All data have been collected at the L.U.R.E (Laboratoire pour l'Utilisation du Rayonnement Electromagnétique, Orsay - France) on the beamline SA32. The experimental setup is schematically drawn in Fig. 4.12. The SuperACO storage ring was operating with a positron beam at 800 MeV and average current of 200 mA. The X-ray energy was selected with an InSb <111> double-crystal monochromator and the data were collected at room temperature in the energy range 1800-2500 eV, with 1 eV step in TEY mode. The investigated depth was estimated to be about 30 nm according to the formula given by Elam *et al.* [90]. The data analysis was performed with the VIPER software [91, 92] using weighted cubic spline functions to simulate the continuous, atomic-like μ_0. The FT was performed in the region 2 Å^{-1} $< k <$ 12 Å^{-1} using the k^2 weight and a gaussian window $W(k)$ centered at $\overline{k} = 7.0$ Å^{-1} and defined as follows: $W(k) = \exp[-3\pi(k-\overline{k})^2/2\overline{k}^2]$.

4.6 Crystallography and X-Ray Diffraction

The X-ray Diffraction (XRD) is used for the structural analysis of crystalline samples. Since the typical interatomic distances in a solid are of the order of 10^{-10} m, an electromagnetic probe of the microscopic structure must have a wavelength λ this short, corresponding to an energy $hc/\lambda = hc/10^{-10}$ m $\simeq 10^4$ eV. These are the characteristic X-ray energies. The scattering process by a perfect periodic structure can be explained in two equivalent ways, due to Bragg and to von Laue [53]. Referring to Fig. 4.13, the Bragg formulation assumes the crystal as made of parallel planes of ions called lattice planes, placed a distance d apart. The conditions to have a sharp, intense peak of the scattered

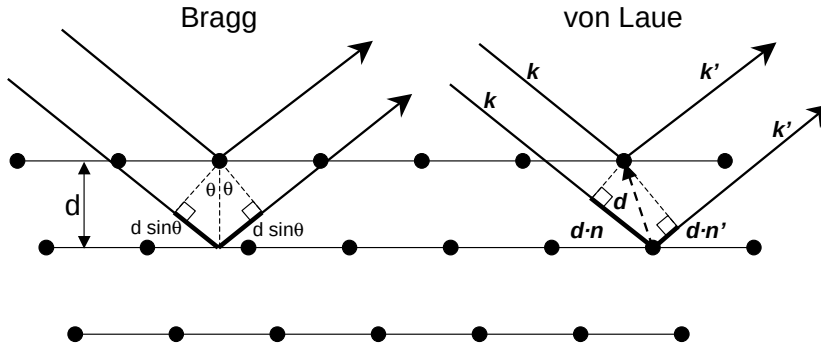

Figure 4.13: Bragg (left) and von Laue (right) pictorial explanations of the X-ray diffraction phenomenon.

radiation are: (i) the X-ray should be specularly reflected and (ii) the reflected waves should interfere constructively. The difference in the optical path of two X-ray scattered from successive planes is simply $2d\sin\theta$ where θ is the incident angle. To have constructive interference, this path must equal an integer number n of wavelengths, leading to the celebrated Bragg condition:

$$2d\sin\theta = n\lambda. \tag{4.48}$$

The alternative way to explain the X-ray diffraction is due to von Laue, who considered the crystal as given by identical microscopic objects (atoms) regularly placed. If two

scatterers are separated by a displacement vector $\mathbf{d}$, the incoming X-ray of wavelength λ along the direction $\hat{\mathbf{n}}$ can be described by the wave vector $\mathbf{k} = 2\pi\hat{\mathbf{n}}/\lambda$. Similarly, the scattered X-ray in a direction $\hat{\mathbf{n}}'$ is described by the wave vector $\mathbf{k}' = 2\pi\hat{\mathbf{n}}'/\lambda$. The difference in the optical paths is simply $\mathbf{d}\cdot(\hat{\mathbf{n}} - \hat{\mathbf{n}}')$ and the condition of constructive interference becomes:

$$\mathbf{d}\cdot(\hat{\mathbf{n}} - \hat{\mathbf{n}}') = n\lambda, \tag{4.49}$$

which, in terms of wave vectors, is:

$$\mathbf{d}\cdot(\mathbf{k} - \mathbf{k}') = 2\pi n. \tag{4.50}$$

or also:

$$e^{i\mathbf{d}\cdot(\mathbf{k}-\mathbf{k}')} = 1. \tag{4.51}$$

It can be demonstrated that Eq. (4.48) and Eq. (4.51) are equivalent (see for example [53], chapter 6). The basic concept to describe a crystalline solid is the *Bravais lattice*, that specifies the periodicity of the atomic arrangement. It consists of all points with positions $\mathbf{R}$ of the form:

$$\mathbf{R} = m_1\mathbf{v_1} + m_2\mathbf{v_2} + m_3\mathbf{v_3}, \tag{4.52}$$

where $\mathbf{v_i}$ $(i = 1, 2, 3)$ are called *primitive* vectors and m_i are integer numbers. The *primitive cell* is the portion of space that, translated through all the primitive vectors, fills the space without overlaps or voids. A physical crystal is completely described by giving its Bravais lattice and the arrangement of molecules/atoms/ions inside the primitive cell. The structure of such crystal consists of identical copies of the same unit, called *basis*, located at the points of the Bravais lattice. An example is reported in Fig. 4.14. For a

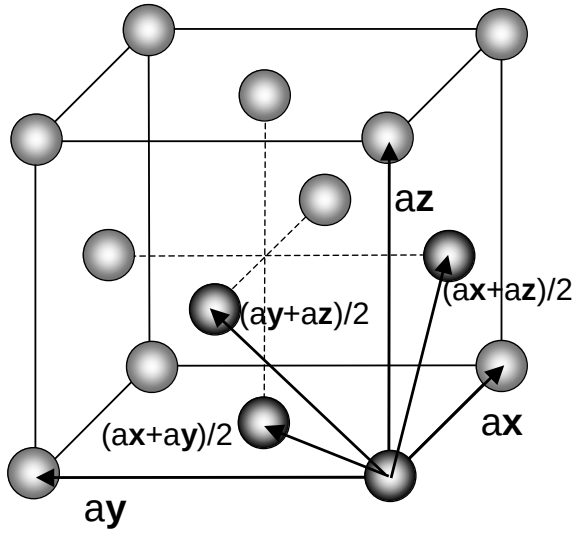

Figure 4.14: Face centered cubic (fcc) Bravais lattice system with lattice parameter a. The four darker atoms constitute the basis.

given Bravais lattice $\mathbf{R}$, the *reciprocal* lattice is defined as the set of vectors $\mathbf{K}$ that gives plane waves with the periodicity of the given Bravais lattice. Analytically:

$$e^{i\mathbf{K}\cdot\mathbf{R}} = 1. \tag{4.53}$$

As an example, for a cubic crystal of lattice parameter a, $\mathbf{R} = a(m_1\hat{\mathbf{x}} + m_2\hat{\mathbf{y}} + m_3\hat{\mathbf{z}})$ and the reciprocal lattice vectors satisfying Eq. (4.53) are $\mathbf{K} = 2\pi/a(k_1\hat{\mathbf{x}} + k_2\hat{\mathbf{y}} + k_3\hat{\mathbf{z}})$, being m_1, m_2, m_3, k_1, k_2 and k_3 integer numbers. The reciprocal lattice plays an important role in crystallography, since it identifies all families of crystallographic planes: a lattice plane is defined as any plane containing at least three non-collinear points of the Bravais lattice, and a family of lattice planes is the set of parallel, equally spaced lattice planes that together contain all the points of the Bravais lattice. For any family of lattice planes a distant d apart, there are reciprocal lattice vectors, the shortest of which has length $2\pi/d$ [53]. The *Miller indices* (usually h, k, l) of a lattice plane are the coordinates of the shortest reciprocal lattice vector normal to that plane. Comparing Eq. (4.51) with Eq. (4.53) it is clear that the change of the wave vector $\mathbf{K} = \mathbf{k} - \mathbf{k}'$ *must* belong to the reciprocal lattice, in order to have constructive interference. For a cubic crystal of lattice parameter a, $\mathbf{K} = 2\pi/a(h\hat{\mathbf{x}} + k\hat{\mathbf{y}} + l\hat{\mathbf{z}})$. By definition, the family of lattice planes $\{hkl\}$ must satisfy the condition

$$| \mathbf{K}|^2 = \left(\frac{2\pi}{a}\right)^2 (h^2 + k^2 + l^2) = \left(\frac{2\pi}{d}\right)^2, \tag{4.54}$$

and using the Bragg's law (Eq. (4.48) with $n = 1$) to eliminate d, we obtain

$$\lambda^2 \frac{(h^2 + k^2 + l^2)}{4a^2} = \sin^2\theta. \tag{4.55}$$

Each family of lattice planes $\{hkl\}$ corresponds to a Bragg peak in the angular position θ, or equivalently with scattering angle 2θ. In nature there are 7 crystal systems and 14 Bravais lattices, as summarized in Table 4.5. Relations like Eq. (4.55) can be found

Table 4.5: Crystal systems and Bravais lattices.

Crystal system	Bravais lattice	Lattice constants	Lattice angles
Cubic	simple	$a = b = c$	$\alpha = \beta = \gamma = 90°$
	body-centered		
	face-centered		
Tetragonal	simple	$a = b \neq c$	$\alpha = \beta = \gamma = 90°$
	centered		
Orthorhombic	simple	$a \neq b \neq c$	$\alpha = \beta = \gamma = 90°$
	base-centered		
	body-centered		
	face-centered		
Monoclinic	simple	$a \neq b \neq c$	$\beta \neq \alpha = \gamma = 90°$
	centered		
Triclinic	simple	$a \neq b \neq c$	$\alpha, \beta, \gamma \neq 90°$
Trigonal	simple	$a = b = c$	$\alpha = \beta = \gamma \neq 90°$
Hexagonal	simple	$a = b, c$	$\alpha = \beta = 90°, \gamma = 120°$

for each of them, revealing that the the diffraction *directions* (i.e. the diffraction angles) are determined only by the *shape* and the *size* of the unit cell. On the other hand, the

intensity of each diffraction peak is affected by the arrangement of atoms inside the unit cell and by the geometry of the XRD experiment. The structure factor F_{hkl} is in general a complex number describing the amplitude and the phase of the wave scattered by all N atoms in the unit cell [93]:

$$F_{hkl} = \sum_{n=1}^{N} f_n e^{2\pi i(hu_n + kv_n + lw_n)}, \tag{4.56}$$

where u_n, v_n and w_n are the fractional coordinates of the n^{th} atom inside the unit cell, and f_n is the corresponding scattering factor. The Lorentz-polarization factor ϕ_{LP} depends on the geometry of the XRD experiment and on the polarization of the X-ray beam (typically randomly polarized) [93]:

$$\phi_{LP} = \frac{1 + \cos^2 2\theta}{\sin^2 \theta \cos \theta}. \tag{4.57}$$

The temperature factor produces a decrease in the intensity of the diffracted peaks. It depends on the thermal vibrations that atoms undergo about their equilibrium positions, and is quantified as e^{-2M} with [93]:

$$M = \frac{6h^2}{mk_B\Theta}\left[\frac{1}{4} + \frac{T^2}{\Theta^2}\int_0^{\Theta/T} \frac{xdx}{e^x - 1}\right]\left(\frac{\sin\theta}{\lambda}\right)^2. \tag{4.58}$$

The angular dependence of the Lorentz-polarization × temperature factors is shown in Fig. 4.15 for pure Fe and pure Al specimens. The multiplicity factor p is the number of

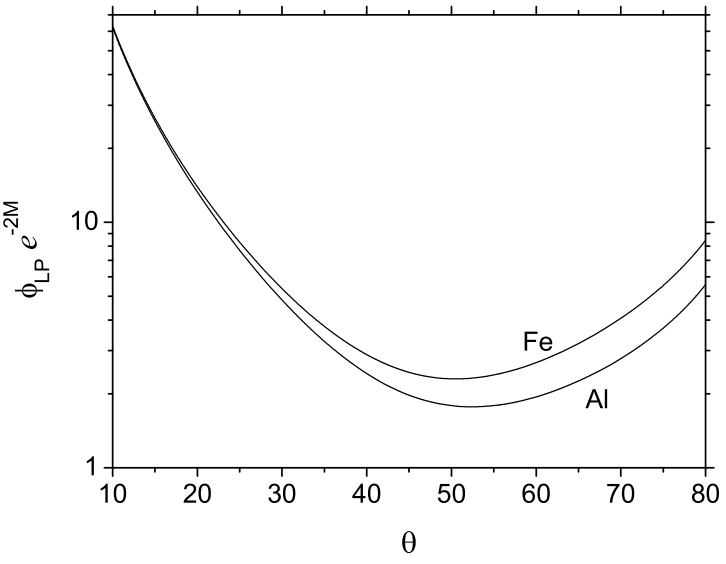

Figure 4.15: Angular dependence of the Lorentz-polarization × temperature factors for Fe and Al substrates.

equivalent directions contributing to the same reflection (for example, in a cubic crystal the [110], [101] and [011] directions are all equivalent and indicated as <110>). Therefore, the intensity I_{hkl} of a given diffraction peak can be written as:

$$I_{hkl} = |F_{hkl}|^2 p \left(\frac{1 + \cos^2 2\theta}{\sin^2 \theta \cos \theta}\right) e^{-2M}. \tag{4.59}$$

All the diffractograms reported in this work have been recorded with a Bruker AXS diffractometer employing a Cu source ($\lambda = 1.54$ Å) and LiF single-crystal monochromator on the diffracted beam. Most of the data have been collected in glancing incidence geometry (GIXRD), the basic principle of which is sketched in Fig. 4.16. The incidence angle α

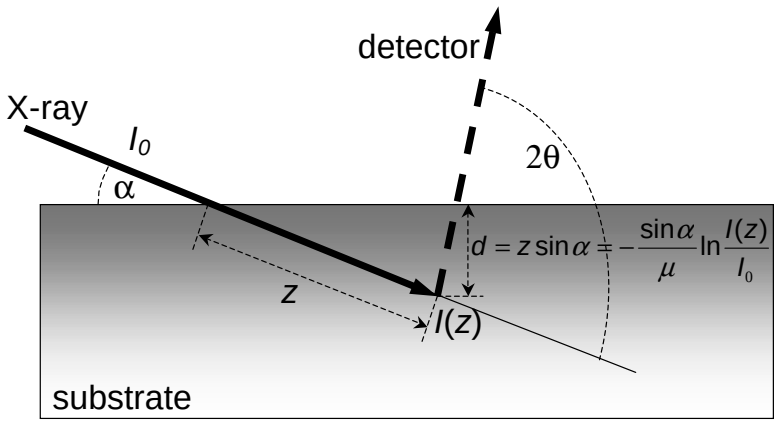

Figure 4.16: Geometry of the GIXRD experiment. The intensity I_0 of the incident X-rays is reduced to $I(z)$ after traveling a distance z inside the substrate, corresponding to a depth $d = z \sin\alpha$.

between the incoming X-rays and the substrate surface is fixed, while the angle between the incoming X-rays and the rotating detector is 2θ. With simple geometrical considerations and using Eq. (4.43), the X-ray penetration depth d can be calculated at any given incidence angle for any material (the linear absorption coefficients μ of the Cu-Kα radiation are tabulated in [93] for all the elements of the periodic table). Table 4.6 reports the penetration depths [μm] at which 90% of the X-ray intensity has been absorbed (i.e. $I(z)/I_0 = 0.1$, see Fig. 4.16), for three incidence angles (1°, 3° and 5°) in pure Fe, pure Al and pure Si substrates.

Table 4.6: Penetration depth [μm] at which 90 % of the Cu-Kα X-ray intensity is absorbed in Fe, Al and Si targets at incidence angles of 1°, 3° and 5°.

Element	glancing angle [°]		
	1	3	5
Fe	0.17	0.50	0.84
Al	1.29	3.86	6.43
Si	1.15	3.44	5.73

Some detailed analysis required the use of the Rietveld refinement [94, 95], that was carried out with the FULLPROF software package [96] (for a review of the Rietveld method see [97]).

4.7 Nanoindentation hardness

The hardness of a material can be defined as its resistance to the penetration of a harder tip [43]. The current method to measure the hardness is to employ a diamond tip as the

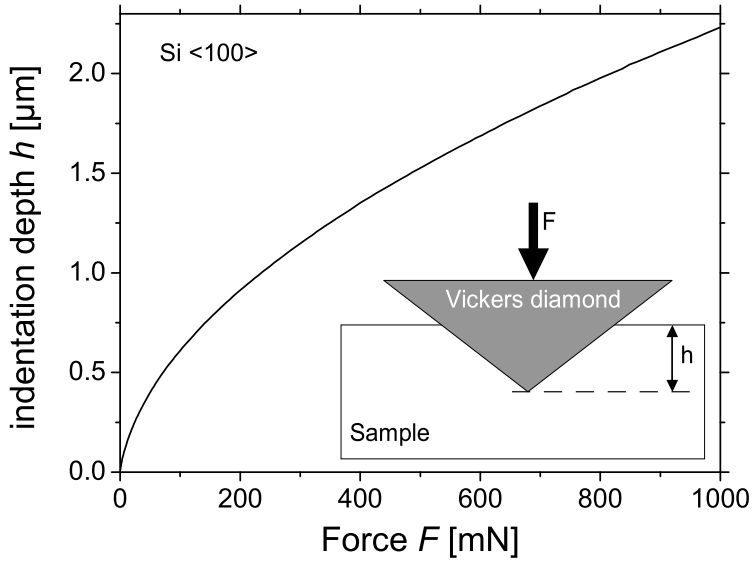

Figure 4.17: Indentation depth vs. load applied on a Vickers diamond tip indenting a single crystalline Si substrate. The inset represents the experimental geometry.

indenter and to determine the indentation depth h as a function of the applied load F. The typical $h - F$ curve of a single-crystalline silicon substrate, <100> oriented is shown in Fig. 4.17. The *universal hardness* H [N/mm^2 or MPa] is defined as the ratio of the applied force F and the area of contact A between the material and the diamond tip, which in turn is function of the indentation depth. For a Vickers diamond indenter, the tip is a square-based pyramid with an opening angle of 136°, and the contact area A is given by $A = 4\,h^2 \sin(68°)/\cos^2(68°) = 26.43\,h^2$. Therefore the universal hardness H is:

$$H = \frac{F}{A} = \frac{F}{26.43\,h^2} \tag{4.60}$$

In reality, the Vickers diamond is never a perfect pyramid especially at its vertex, and any geometrical deviation leads to large errors in the estimation of the hardness. To overcome this problem, the experimental setup is calibrated by indenting a homogeneous material of known hardness (typically <100> single crystalline Si): the measured hardness is corrected in order to match its real value, and the correction function is stored in a computer. Each indentation profile is then corrected accordingly. An example of hardness curve before and after the correction is reported in Fig. 4.18. All hardness measurements shown in the next chapters have been performed with a Fisherscope HV 100 allowing a depth resolution of few nanometers (depending on the surface roughness) and a force definition that can be better than 50 nN. The maximum load is chosen according to the analyzed material (typically less than 1 N); the indentation curve is obtained by increasing

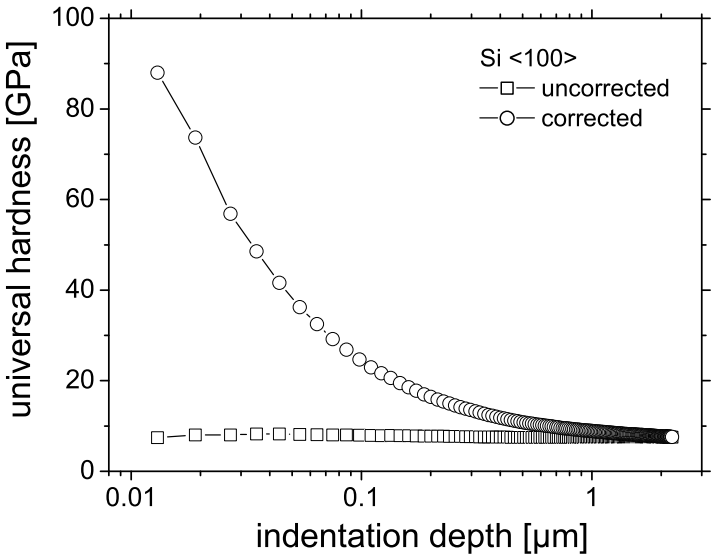

Figure 4.18: Corrected and non-corrected hardness of a single crystalline Si substrate.

the square root of the load with constant increments (150 steps in total) and measuring the corresponding indentation depth at each step. The force is applied for a tenth of a second in each step. The data acquisition procedure is computer-controlled and requires few minutes. In general, 20 to 50 indentation curves are measured at different positions on the surface of the samples, in order to improve the statistics of the acquisition.

Chapter 5

The iron substrate

Laser irradiation of iron in nitrogen atmosphere (iron laser nitriding) has been extensively investigated in the past years, determining the influence of the laser fluence, the number of shots, the pulse duration and wavelength, and the nitrogen gas pressure on the efficiency of the treatment. The results are reported in Ref. [28, 29, 30, 31, 98, 99, 100] and only the most recent findings on the phenomenological modeling of the mass transport mechanism will be discussed here [101]. Due to the successful treatment of iron in nitrogen atmosphere, the laser process has been extended to different kinds of gaseous environments. The results of the laser irradiation in methane (CH_4) will be reported [102, 103], showing the effectiveness of the carbon incorporation into the iron matrix.

5.1 The nitrogen transport mechanism

The following sections will describe a phenomenological model (based on the experimental evidence) of the nitrogen transport mechanism during single spot irradiations of iron in N_2 gas. The nitrogen take-up mechanism has already been modeled for the raw laser beam [104]: the nitrogen depth profiles were fitted with a linear combination of two complementary error functions (erfc) and the parametrization vs. the number of laser pulses was obtained. Further experiments have been performed at the laser fluence of 4 J/cm^2 in 1 bar N_2 with the homogeneous laser beam, in order to hinder the mass transport due to convection.

5.1.1 The diffusion process

Using the capability of RNRA, the contribution of *each* laser shot on the mass transport mechanism can be distinguished. By irradiating the target in enriched isotopic atmosphere, it is possible to track the evolution of the nitrogen profiles under the effect of subsequent laser pulses. An irradiation in ^{15}N atmosphere will be marked by a star (*) and the notation m^*/n will indicate m pulses in enriched atmosphere followed by n pulses in natural nitrogen. Fig. 5.1 shows the results of the isotopic experiments $1^*/0$, $1^*/1$, $1^*/2$, $1^*/4$, illustrating the evolution of the nitrogen profile produced by the first pulse

($1^*/0$) after 1 ($1^*/1$), 2 ($1^*/2$) and 4 ($1^*/4$) subsequent laser shots in natural nitrogen. The first pulse ($1^*/0$) can be fitted by a complementary error function (erfc):

$$e(z, t_e) = C \text{ erfc}[z/\sqrt{4Dt_e}], \tag{5.1}$$

where C is the surface concentration, D the diffusion constant and t_e the diffusion time. The other isotopic experiments ($1^*/1$, $1^*/2$, $1^*/4$) can be fitted by gaussian profiles:

$$g_n(z, t_g) = \frac{M}{\sqrt{\pi} L_n/2} \exp[-z^2/L_n^2]. \tag{5.2}$$

M is the amount of ^{15}N remaining after further irradiations and L_n is the diffusion length of the profile after n pulses. As illustrated in Fig. 5.2, the square of L_n depends linearly

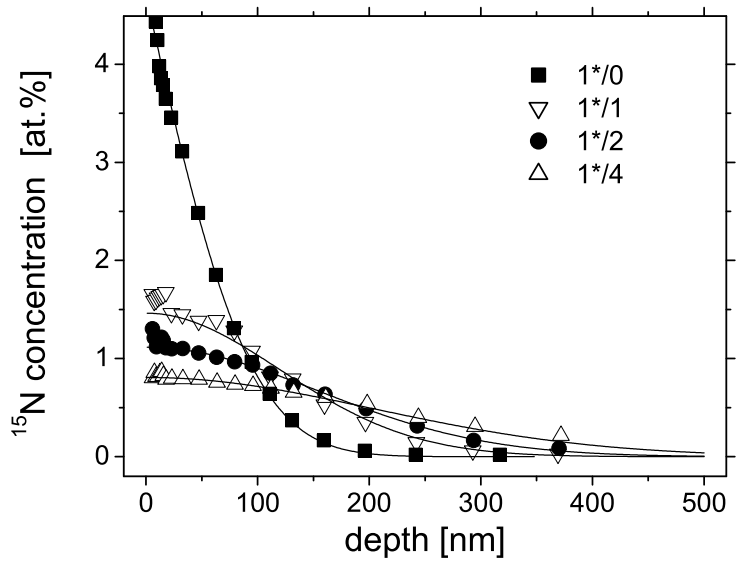

Figure 5.1: Isotopic experiments $1^*/0$, $1^*/1$, $1^*/2$, $1^*/4$: the symbols represent the experimental data, the solid lines are the simulations.

on n:

$$L_n^2 = 4(Dt_e + nDt_g). \tag{5.3}$$

Dt_e is the contribution of the first pulse (the erfc) to the total diffusion length L_n and $t_e + nt_g$ is the total diffusion time of the profile after $n + 1$ pulses. Eq. (5.3) is a clear evidence of the diffusion nature of the process: the increase in the diffusion length is due to the linear increase in the total diffusion time with the number of laser pulses. It should be noticed that both Eq. (5.1) and Eq. (5.2) are solutions of the one-dimensional diffusion equation:

$$\frac{\partial C(z,t)}{\partial t} = D\frac{\partial^2 C(z,t)}{\partial z^2}, \tag{5.4}$$

where $C(z, t)$ is the solute concentration and the diffusion constant D is assumed to be independent of the concentration itself, the time t, the position z and the substrate

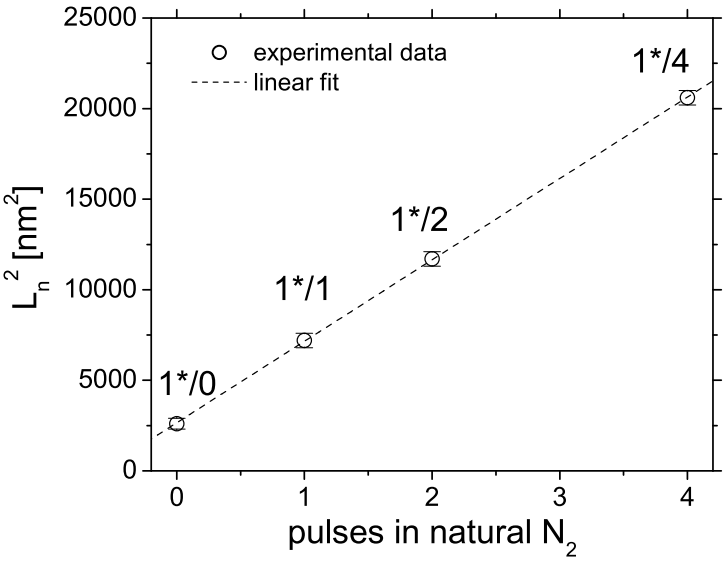

Figure 5.2: Diffusion length squared of the depth profiles as a function of the number of pulses.

temperature (the use of one-dimensional equations was justified in section 3.1). The experimental value of C is 4.1 at.%, while Dt_e is 2700 nm^2 (from such experiments we can estimate only the product Dt). The diffusion constant D of nitrogen in liquid iron at a mean temperature of the melt (∼2500 K) can be evaluated according to the relation $D = D_0 \exp(-Q/RT)$, where $D_0 = 2.86 \times 10^{-3}$ cm^2/s and $Q = 61090$ J/mol [105], obtaining $D = 15$ nm^2/ns and therefore $t_e \sim 180$ ns. Within the theory of Laser Supported Absorption (LSA) waves [31, 106], this time is consistent with the existence of a rarefaction fan and it represents the interaction time during which N is supplied to the target. The value of Dt_g is 4500 nm^2, corresponding to a time $t_g \sim 300$ ns, that is in excellent agreement with the simulated duration of the melt (see Fig. 3.2). The fact that $t_g \neq t_e$ also reveals the different nature of the first pulse with respect to its evolution, meaning that the nitrogen take-up (erfc) and the further diffusion (gaussian) are distinct processes. A second series of isotopic experiments, $4/1^*$, $8/1^*$, $32/1^*$, $64/1^*$ [29], was performed in order to check how the nitrogen take-up of the *last* pulse is affected by the nitrogen content. We observed that the erfc can nicely fit these profiles as well, but the surface concentration C seems to increase with n, while the diffusion length $\sqrt{4Dt_e}$ decreases. The number of pulses n is not the proper physical parameter, since the observed changes should be correlated to the prior modifications induced in the target. The *total* nitrogen concentration S_{n-1} on the surface of the target, due to all previous $n-1$ pulses seems to be a suitable choice. We can express the evolution of C as $C_n = C(S_{n-1})$ and the evolution of Dt_e as $(Dt_e)_n = Dt_e(S_{n-1})$ (notice that here C_n represents the contribution of the n^{th} erfc *alone* to the nitrogen surface concentration, while S_{n-1} is the *total* nitrogen surface content after $n-1$ pulses); writing C_n as a power series and considering only the linear term we obtain:

$$C_n = a + bS_{n-1} = C(1 + \sigma S_{n-1}), \tag{5.5}$$

with $\sigma > 0$ (since C_n increases with S_{n-1}). In a similar way:

$$(Dt_e)_n = Dt_e(1 + \mu S_{n-1}), \tag{5.6}$$

with $\mu < 0$. σ and μ are parameters of the model, while S_{n-1} is determined by iteration. The dependencies of the diffusion length $2\sqrt{(Dt_e)_n}$ and the erfc surface concentration C_n on the number of laser shots n are reported in Fig. 5.3.

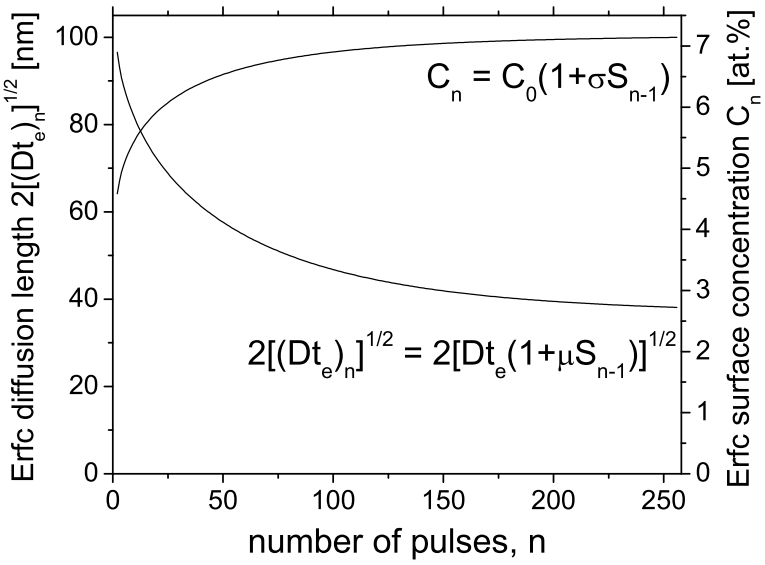

Figure 5.3: Evolution of the erfc surface concentration C_n and the erfc diffusion length $(Dt_e)_n$ as a function of the number of laser pulses.

5.1.2 The melting depth

A factor that we have to include in the model is the finite melting depth. According to the thermodynamic simulations, the melting depth d_m induced by the excimer laser in iron should be of the order of 1 μm (see Fig. 3.2). We are assuming that the diffusion of nitrogen takes place only in the liquid iron (due to the much smaller nitrogen diffusion constant in the solid [105], the observed nitrogen profiles would not be justifiable). The amount of nitrogen is therefore confined inside the molten layer; mathematically this condition is satisfied with a proper choice of the gaussian normalization factor (the erfc is always within the melting depth), so Eq. (5.2) can be written as:

$$g_n(z, t_g) = \frac{M}{\int_0^{d_m} \exp[-z'^2/L_n^2] dz'} \exp[-z^2/L_n^2]. \tag{5.7}$$

The integral of $g_n(z, t_g)$ over the whole melting region ($0 \leq z \leq d_m$) is M for any values of L_n. We verified numerically that the condition reported in Eq. (5.7) is analogous to the introduction of a reflecting interface at the maximum melting depth: $\left.\frac{\partial C}{\partial z}\right|_{z=d_m} = 0$.

5.1.3 The nitrogen losses

The effect of each irradiation is not only to incorporate nitrogen in the sample as an erfc profile, but also to remove some of the nitrogen introduced by the previous pulses. This is attributed to the combined effects of ablation and nitrogen degassing of the target. The amount of the nitrogen incorporated in the sample with the n^{th} erfc is:

$$A_n = \int_0^{d_m} C_n \mathrm{erfc}[z/\sqrt{4(Dt_e)_n}]dz \simeq 2C_n\sqrt{(Dt_e)_n/\pi}, \tag{5.8}$$

and what is remaining after the following irradiation can be written as:

$$M_n^{n+1} = \int_\Delta^{d_m} C_n \mathrm{erfc}[z/\sqrt{4(Dt_e)_n}]dz, \tag{5.9}$$

where Δ is the nitrogen depletion depth of the erfc. Here, the parameter Δ includes both the ablation and the nitrogen degassing effects. M_n^{n+1} represents the area of the gaussian evolution of the n^{th} erfc after the $(n+1)^{th}$ pulse. Under the effect of further laser shots, the width of this gaussian profile will increase according to Eq. (5.3), but the area will decrease after each pulse due to ablation/degassing, and the nitrogen loss can be computed iteratively as follows:

$$M_n^{q+1} = \int_\delta^{d_m} \left(\frac{M_n^q}{\int_0^{d_m} \exp[-z'^2/L_n^2]dz'} \exp[-z^2/L_n^2] \right) dz, \tag{5.10}$$

where δ is the depletion depth of the gaussian and $q > n+1$. Both δ and Δ are parameters of the model determining the nitrogen loss per pulse. We observed that $\Delta > \delta$, i.e., the nitrogen loss is larger for the erfc than the gaussian. The value of δ is in good agreement with the ablation depth observed experimentally for the homogenized beam treatments [107], and the fact that $\Delta > \delta$ indicates a stronger degassing effect of the N in the erfc profile, probably correlated to the differences in the two types of nitrogen distributions (for example, the degassing rate has a quadratic dependence on the N concentration [105]).

5.1.4 The results

To summarize the results, a laser pulse "introduces" nitrogen in the sample, producing an erfc depth profile. Under the effect of the subsequent pulses the erfc evolves into gaussian profiles with increasing width and decreasing area vs. n (using an erfc as initial condition in Eq. (5.4), the time evolution closely resembles a gaussian profile [108]), but a new erfc is created by each further laser shot. Therefore, the overall nitrogen profile after n pulses is given by the sum of $n-1$ gaussians plus an erfc representing the effect of the n^{th} pulse. Fig. 5.4 illustrates the experimental nitrogen profile after 8 pulses and its simulation. The contribution of each pulse is labeled in chronological order from 1 to 8 and added to all previous ones. The last pulse of a series of n is hence described by the following erfc:

$$e_n(z, t_e) = C_n \mathrm{erfc}[z/\sqrt{4(Dt_e)_n}], \tag{5.11}$$

where C_n and $(Dt_e)_n$ are calculated respectively from Eq. (5.5) and Eq. (5.6). The evolution of a previous erfc, for example the j^{th} erfc (with $1 \leq j < n$), is given by the following

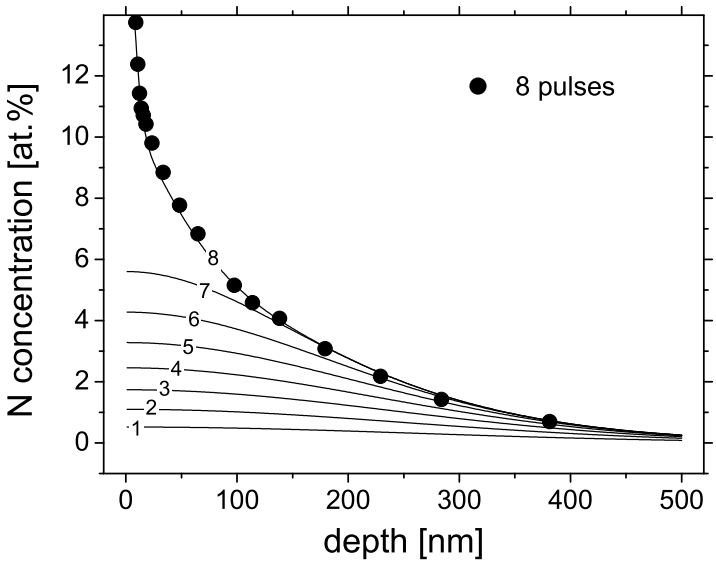

Figure 5.4: The nitrogen profile after 8 laser pulses (solid symbols): the evolution of each pulse is labeled in chronological order and added to all the previous ones.

gaussian:

$$g_n^j(z,t_g) = \left(\frac{M_j^n}{\int_0^{d_m}\exp[-z'^2/(4(Dt_e)_j+4(n-j)Dt_g)]dz'}\right) \times \exp[-z^2/(4(Dt_e)_j+4(n-j)Dt_g)], \quad (5.12)$$

where the value of M_j^n is calculated according to Eq. (5.9) and Eq. (5.10), while the diffusion length after the n^{th} pulse is $2\sqrt{(Dt_e)_j+(n-j)Dt_g}$ (see Eq. (5.3)). The overall nitrogen depth profile p_n after n laser shots is described by the sum:

$$p_n(z) = e_n(z,t_e) + \sum_{j=1}^{n-1} g_n^j(z,t_g). \quad (5.13)$$

Notice that the value of S_{n-1} appearing in Eq. (5.5) and in Eq. (5.6) is simply:

$$S_{n-1} = p_{n-1}(z)|_{z=0} = C_{n-1} + \sum_{j=1}^{n-2} g_{n-1}^j(0,t_g). \quad (5.14)$$

Besides, the overall nitrogen loss G_n after the n^{th} pulse is:

$$G_n = \int_0^{\Delta} e_n(z,t_e)dz + \int_0^{\delta}\sum_{j=1}^{n-1} g_n^j(z,t_g)dz \simeq \int_0^{\Delta} e_n(z,t_e)dz + (S_n - C_n)\,\delta. \quad (5.15)$$

As shown in Fig. 5.5, the nitrogen take-up A_n (Eq. (5.8)) decreases with increasing number of laser pulses n, while the nitrogen loss G_n increases with n. Both functions approach the same value in the limit $n \to \infty$, reflecting the fact that the nitrogen losses compensate the

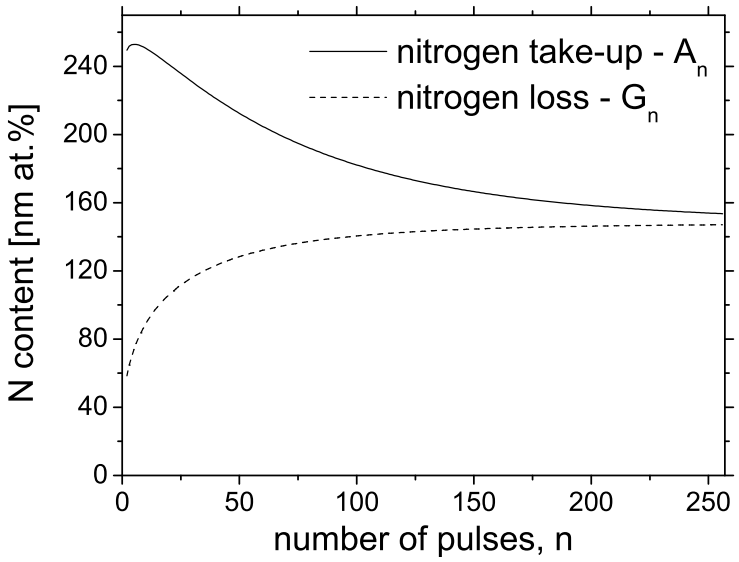

Figure 5.5: Nitrogen take-up (continuous line) and nitrogen losses (dashed line) per pulse as a function of the number of laser shots.

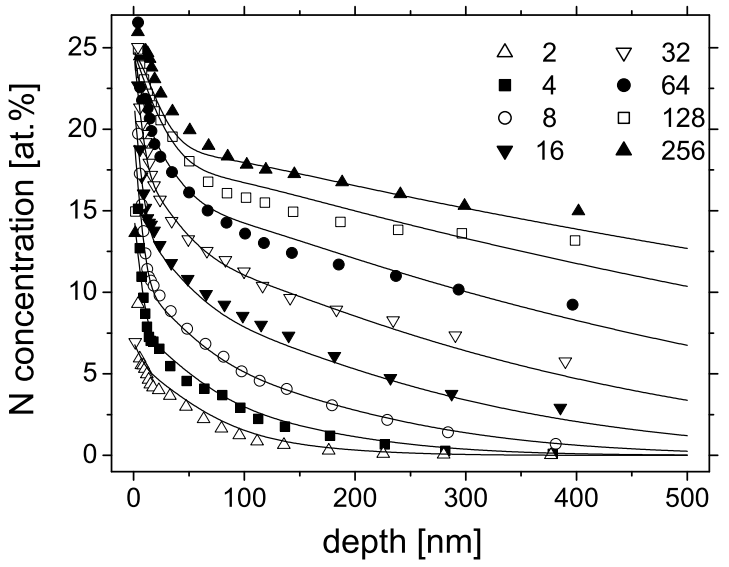

Figure 5.6: Experimental nitrogen depth profiles (symbols) and corresponding simulations according to Eq. 5.13 (solid lines) of the pulse series 2, 4, 8, 16, 32, 64, 128, 256.

up-take for high number of laser shots, and the overall nitrogen content remains constant. Eq. (5.13) is used to fit the experimental nitrogen depth profiles obtained with various number of pulses and the results are illustrated in Fig. 5.6. The simulations (solid lines) of the nitrogen profiles obtained with 2, 4, 8, 16, 32, 64, 128 and 256 laser pulses are

calculated using the parameters reported in Table 5.1.

Table 5.1: List of parameters used in the model. Where possible, a comparison with the experimental data has been given.

Parameter	Value	From [31, 107]
C [at.%]	4.1	-
Dt_e [nm^2]	2700	1700
σ [at.%$^{-1}$]	1/35	-
μ [at.%$^{-1}$]	-1/30	-
Dt_g [nm^2]	4500	4500
Δ [nm]	13	-
δ [nm]	4	2
d_m [nm]	900	800

5.2 Laser irradiation in methane atmosphere

After the successful and promising results of iron laser nitriding, the irradiation has been extended to other gaseous environments. Due to the technological importance of carbon in iron, a carbon-containing atmosphere was chosen. The following sections will focus on the results of the meandering irradiation in methane (CH_4) gas and the influence of experimental parameters, such as the spot overlap and the gas pressure on the mechanical and crystallographic properties will be illustrated.

5.2.1 Influence of the meandering spot overlap

The preliminary investigation on the efficiency of the carbon incorporation has been performed with fixed laser fluence (4 J/cm^2) and fixed methane gas pressure (1.5 bar), varying the spot overlaps of the meandering treatment. The phase analysis has been carried out by means of Mössbauer spectroscopy (CEMS and CXMS) and XRD, the carbon depth profiles were investigated with RBS and the mechanical properties by nanoindentation. The CEM spectra of the samples treated with 8×8, 11×12 and 16×16 meander scans are shown in Fig. 5.7. The 8×8 scan produces a mixture of γ-Fe(C) (austenite), ϵ-Fe$_x$C and non-reacted α-Fe. The γ phase is fitted using a singlet (IS $\simeq$ 0.06(1) mm/s) representing an iron site without carbon neighbors, and a doublet (IS $\simeq$ 0.02(1) mm/s, QS $\simeq$ 0.65(2) mm/s) due to an iron site with one carbon nearest neighbor. Using the binomial distribution, the relative area of the singlet, A_s, and the doublet, A_d, can be related to the occupancy of the interstitial octahedral sites, and the average carbon content y_c can be estimated according to the relations [31]:

$$y_c = 1 - \sqrt[6]{\frac{A_s}{A_s + A_d}}, \tag{5.16}$$

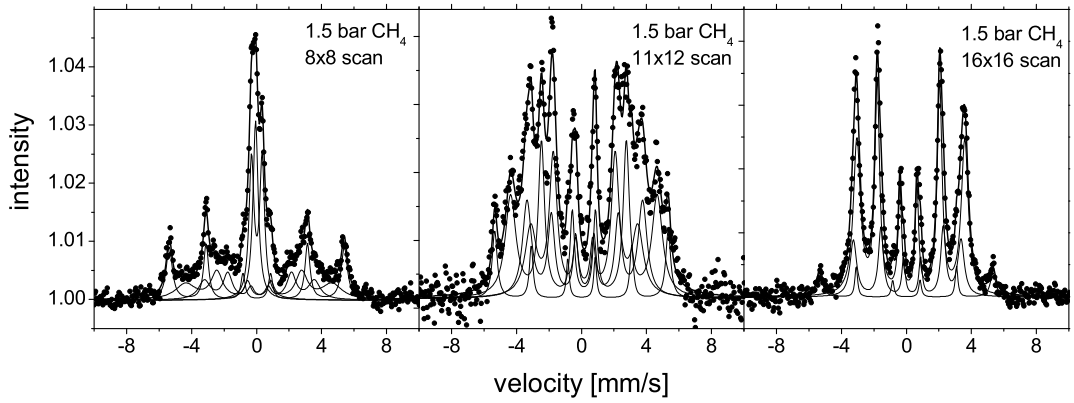

Figure 5.7: CEM spectra and corresponding fits of the iron samples irradiated in 1.5 bar CH_4 with 8×8, 11×12 and 16×16 spot overlaps (from left to right).

obtaining $y_c \simeq 13$ at.%. This value is higher than the maximum solubility of carbon in γ-Fe under equilibrium conditions, but as we explained in chapter 3, the laser irradiation produces extreme pressures and temperature gradients that can lead to far-from-equilibrium solid solutions. The ϵ-Fe_xC is represented by two sextets with hyperfine fields of ~ 28 T and ~ 21 T. They are attributed to the hexagonal arrangement of iron atoms with one (ϵ-Fe_6C) and two (ϵ-Fe_3C) interstitial carbon atoms, respectively. The relative fraction of the two components allows to determine the average stoichiometry of the phase, obtaining $x = 4.33$. The atomic arrangement of the ϵ-Fe_3C carbide is shown in Fig. 5.8: the ϵ phase with the Fe_6C stoichiometry is obtained removing one of the two carbon atoms. With the 11×12 meander scan, no austenite is observable with CEMS,

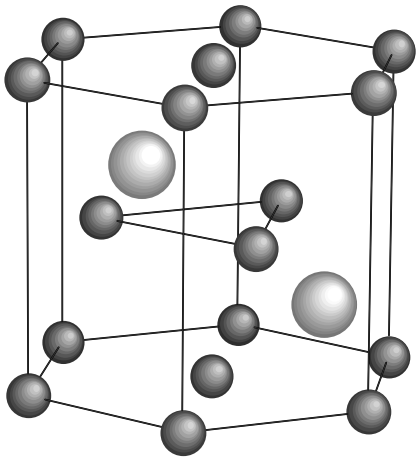

Figure 5.8: Atomic arrangements of the ϵ-Fe_3C carbide: the darker spots represent the positions of the iron atoms (space group $P6_322$).

although a mixture of γ and ϵ phases is visible with GIXRD (grazing incidence of 5°),

as shown in Fig. 5.9. Since the information depth of GIXRD with the incidence angle of

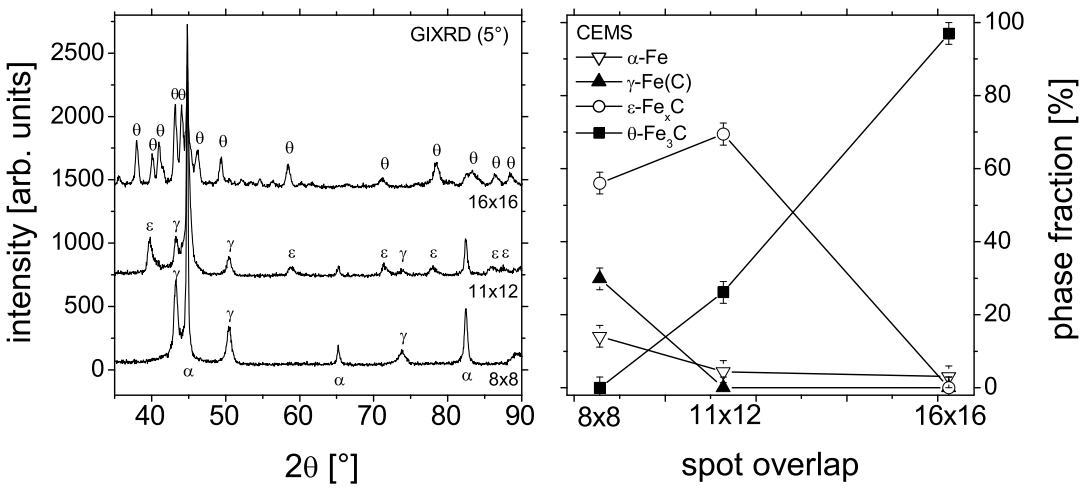

Figure 5.9: Phase fraction vs. the spot overlap as obtained from the CEMS analysis (right) and the corresponding GIXRD diffractograms measured at grazing angle of 5° (left). All main XRD peaks are labeled.

5° is about 0.8 μm (see Table 4.6), while CEMS is sensitive to the first 150 nm from the surface, we can conclude that the austenite is not formed at the surface of the sample, but deeper inside, most probably close to the maximum melting depth, where the carbon content is lower. Opposite to the austenite, some θ-Fe_3C appears in the CEM spectrum, but not in the X-ray diffractogram, indicating that its formation is limited to the surface (first 150 nm) of the specimen. Notice that in the sample meandered with the 8×8 scan, only the austenite is visible with XRD, while both the the γ and the ϵ phases are observed in the CEM spectra, suggesting that the latter is mainly confined on the sample surface. The treatment performed with the 16×16 spot overlap reveals the formation of a cementite (θ-Fe_3C) layer and no other carbide is observed by means of CEMS and GIXRD. The phase evolution as a function of the spot overlap is reported in Fig. 5.9. The Mössbauer spectral area has been converted to phase fraction taking into account the recoilless factor f_{DW} of each phase, as given in Eq. (4.30). The Debye temperature of the carbon-rich carbides (ϵ and θ) was measured by Mathalone *et al.* [109], who obtained the value of about 200 K, corresponding to $f_{DW} = 0.36$ at room temperature. This is quite small compared to the recoilless factors of α-Fe (0.8) and γ-Fe (0.6). The mechanical properties of the irradiated samples have been investigated by nanoindentation, and the hardness curves are reported in Fig. 5.10. Jönsson and Hogmark [110] developed a model to estimate the composite hardness $H(d)$ of a coating on a softer substrate as a function of the indentation depth. According to their analysis:

$$H(d) = H_s + (H_c - H_s)\left[2k\frac{t}{d} - k^2\left(\frac{t}{d}\right)^2\right]. \tag{5.17}$$

H_c and H_s are respectively the hardness of the coating and the substrate, d is the indentation depth, t is the coating thickness and k (with $0.073 < k < 0.14$) is a parameter

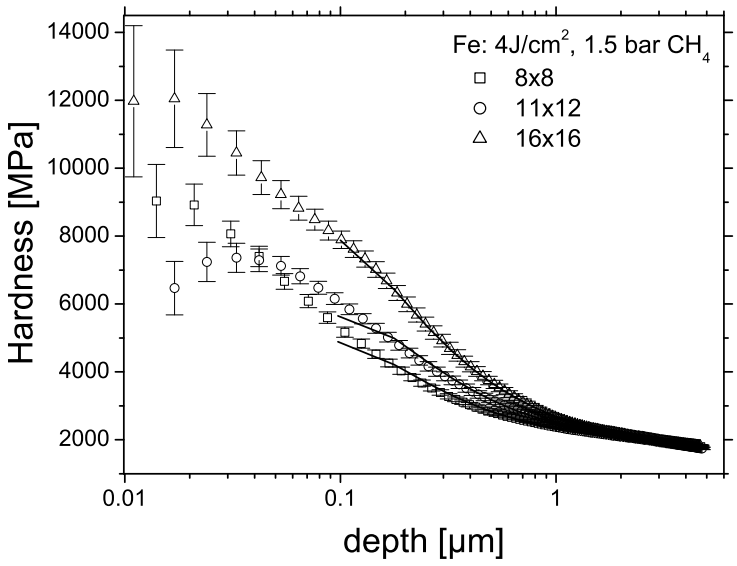

Figure 5.10: Microhardness curves of the samples meandered in CH_4 (symbols). The continuous lines are the fitting according to Eq. 5.17.

describing the plastic deformation of the film as the diamond tip indents the sample. For simplicity we assumed $k = 0.1$. The model works properly if the ratio $d/t > 0.1$; since the thickness t of the carburized layer should not exceed the melting depth ($\simeq 1$ μm), the model can be applied to indentation depths $d > 100$ nm. The continuous lines in Fig. 5.10 are the fits of the hardness profiles according to Eq. (5.17), using H_s, H_c and t as fitting parameters. The results are reported in Table 5.2. The substrate hardness

Table 5.2: Results the hardness profiles fits vs. the spot overlap.

Meandering	H_s [MPa]	H_c [MPa]	t [μm]
8×8	1761(7)	4888(85)	0.95(3)
11×12	1701(10)	5668(70)	1.04(3)
16×16	1588(3)	7927(20)	0.91(1)

H_s is ~ 1700 MPa for all samples and the thickness t of the layer is ~ 0.95 μm, in good agreement with the calculated melting depth. The hardness H_c of the carburized film increases with the spot overlap and therefore with the amount of cementite (the hardest carbide [39]). Despite the fact that the model was developed for homogeneous coatings on softer substrates, the fits are quite satisfactory and the average hardness of the carburized layers is consistent with the phase analysis. Since the mechanical properties and the crystallographic phases obtained with the 8×8 meander scan in CH_4 closely resemble what has been observed with nitrogen gas under identical experimental conditions (same spot overlap, same pressure and laser fluence) [30, 111], the further investigation has been focused on the higher spot overlap.

5.2.2 Influence of the methane gas pressure

As already pointed out in the previous section, with the 11 × 12 scan a complex overlap of magnetic phases has been observed with Mössbauer spectroscopy. In order to achieve a better understanding of the carburization process we performed the same meandering treatment at various methane pressures ranging from 0.1 bar to 10 bar. The Mössbauer spectra with the corresponding fits are shown in Fig. 5.11. The central component, at-

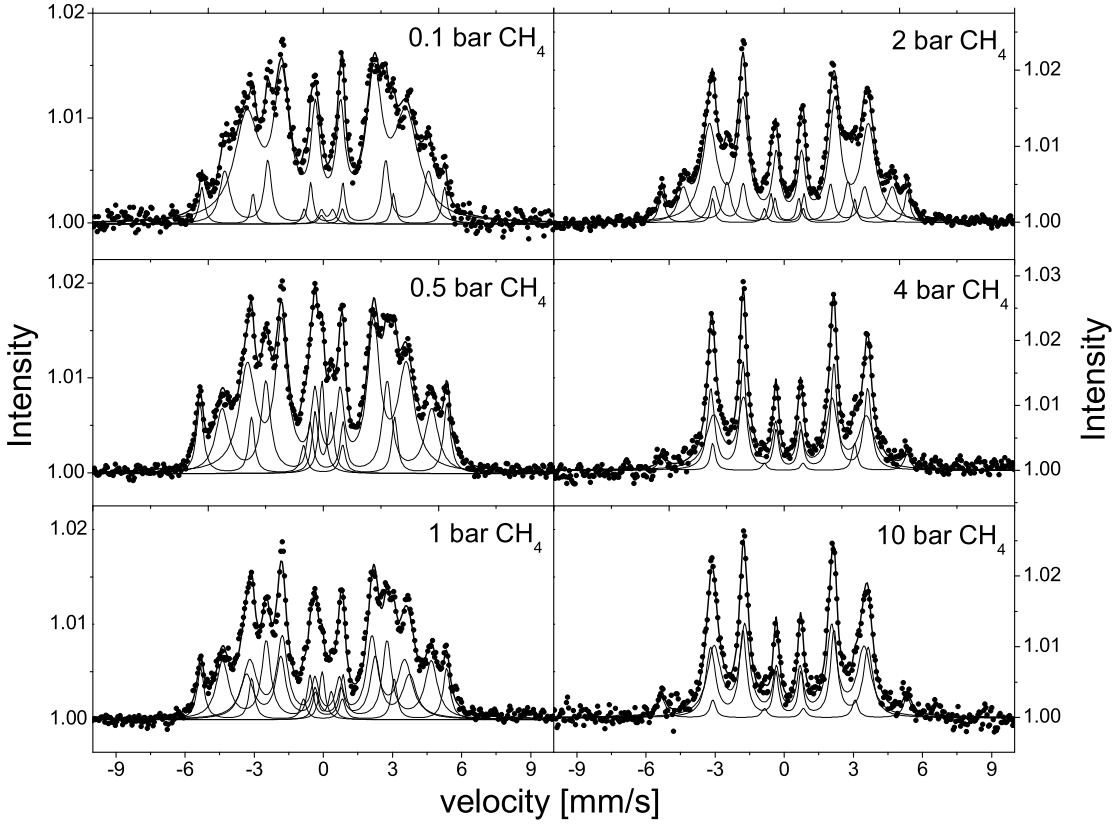

Figure 5.11: CEM spectra and corresponding fits of the iron samples irradiated at different methane pressures with the 11×12 meandered scan.

tributed to γ-Fe(C) austenite, is detectable only for pressures lower than 2 bar, while the sextet of non-reacted iron and additional broad magnetic components are observed over the entire pressure range. The two characteristics sextets of ϵ-Fe_xC carbide can be distinguished, but a gradual increase in the isomer shift of the lower hyperfine field component (corresponding to ϵ-Fe_3C) is observed with increasing pressures. Simultaneously, the relative area of the higher hyperfine field component (corresponding to ϵ-Fe_6C) gradually drops, disappearing if the CH_4 pressure is higher than 4 bar. As confirmed by GIXRD measurements carried out at grazing incidence of 1° (corresponding to an information depth of about 200 nm), this behaviour is attributed to the gradual increase of the θ-Fe_3C relative fraction at expenses of the ϵ-Fe_xC phase with increasing methane

pressure. The Mössbauer analysis has been performed employing two distinct subspectra for the lower hyperfine field component, constraining their isomer shift to 0.17 mm/s for the ϵ-Fe_3C and to 0.205 mm/s for the θ-Fe_3C phase. These are their values at the edges of the pressure range, i.e. the isomer shift of the ϵ-Fe_3C formed at 0.1 bar CH_4 (where no cementite is present) and the isomer shift of the θ-Fe_3C formed at 10 bar CH_4 (where no ϵ carbide is present). This procedure allows to separate the ϵ and the θ phases in the Mössbauer spectra. At high methane pressure only the cementite is formed and the result is analogous to the irradiation in 1.5 bar CH_4 with the 16×16 scan. The relative phase fractions extrapolated from the Mössbauer analysis are reported in Fig. 5.12 as a function of the CH_4 pressure. The amount of non-reacted iron is about 5% regardless of

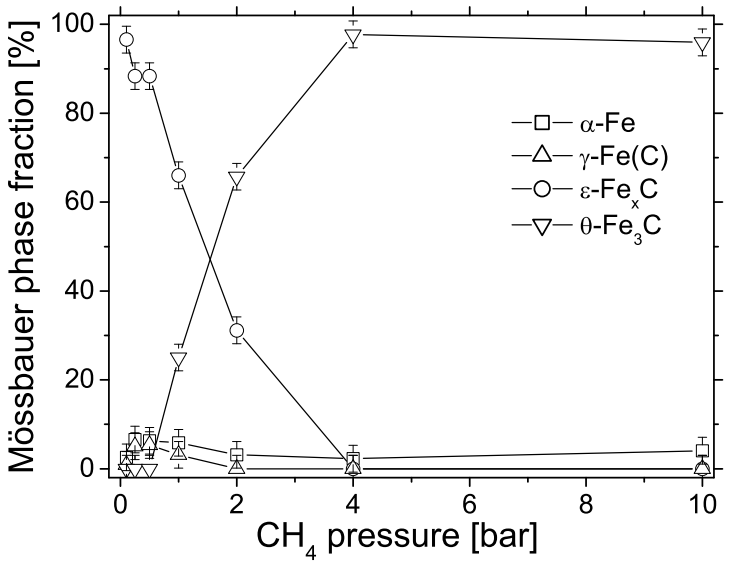

Figure 5.12: Phase fractions obtained from the Mössbauer analysis vs. the methane gas pressure.

the ambient pressure, while the amount of cementite sharply increases at expenses of the ϵ-Fe_xC carbide in the region 1-4 bar. The austenitic phase drops simultaneously to the ϵ phase and both are not observed for irradiations performed at methane pressures higher than 2 bar. Thanks to the capability of the Mössbauer spectroscopy not only the relative amount of all phases can be obtained, but also the average carbon content in each of them. The overall concentration of carbon as a function of the methane pressure is reported in Fig. 5.13. The data have been compared with the carbon contents extrapolated from the RBS depth profiles (averaged over the first 150 nm from the surface in order to compare the results with the CEMS analysis). The agreement is quite good for pressures higher than 2 bar. The large discrepancy in the region $0.1 - 2$ bar is due to the considerable amount of carbon deposited on the samples treated at low pressure (see the RBS depth profiles in the inset of Fig. 5.13). Since the Mössbauer technique is not sensitive to carbon and the GIXRD measurements did not show any crystalline phase other than iron or iron carbides, we can conclude that the carbon forms amorphous layers. At the moment, a valid explanation of this phenomenon is missing. Intuitively, one would expect thicker

carbon layers for increasing methane pressure, but the opposite trend is observed instead. This might be correlated to the shielding effect of the ambient gas on the laser energy (see section 3.3.3). The higher is the methane pressure, the stronger is the shielding of the laser beam and less laser energy reaches the substrate. This reduces the surface temperature and thus the vapor pressure. As a consequence, the effect of the substrate on the plasma formation is hindered: fewer CH_4 molecules are ionized/decomposed, and less carbon is deposited on the target surface.

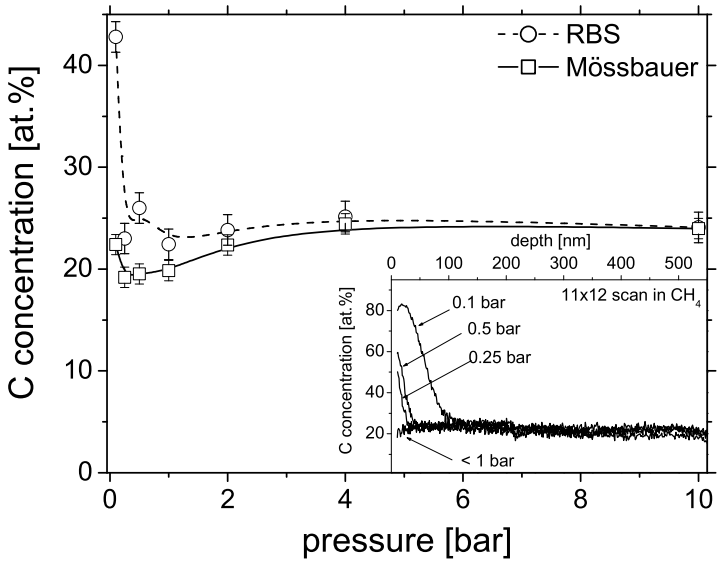

Figure 5.13: Average carbon content vs. the methane gas pressure obtained from the RBS depth profiles (dash line) and from the Mössbauer analysis (continuous line). The inset show the most significant RBS carbon depth profiles.

5.2.3 Formation of a homogeneous cementite layer

As we already mentioned in the preliminary investigation, with the 16 × 16 meander scan at an intermediate methane pressure (1.5 bar), the only iron-carbide formed in the irradiated sample is θ-Fe_3C. Due to its technological importance in iron metallurgy, a more detailed investigation has been carried out [102]. Fig. 5.14 shows the RBS spectra of the untreated substrate and the one irradiated at 4 J/cm^2 in 2 bar CH_4 with the 16×16 scan. After the laser treatment, the Fe yield reduces due to the carbon incorporation into the specimen. The simulation performed with the RUMP code shows excellent agreement with the cementite stoichiometry (25 at.% C and 75 at.% Fe) to a depth of at least 650 nm. The Mössbauer data and their analyses are shown in Fig. 5.15. The CEM spectrum, with an information depth of about 150 nm, shows that almost 97% of the relative phase fraction is cementite, while the remaining part is non-reacted α-Fe. The two characteristic sextets of θ-Fe_3C can be clearly distinguished in the spectrum. They originate from the two different crystallographic iron sites: Fe(I) with 3 C and 11 Fe

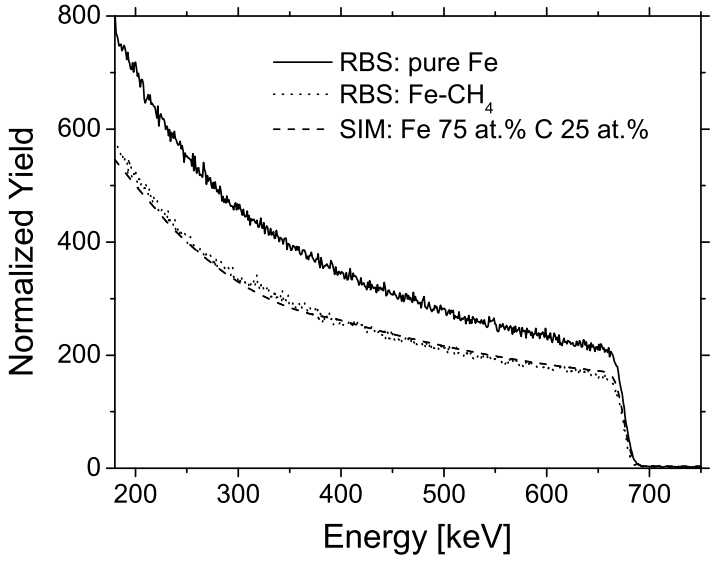

Figure 5.14: RBS spectra of the non-treated sample (higher yield) and the one irradiated with the 16×16 scan at fluence of 4 J/cm^2 in 2 bar CH_4 (lower yield). The dashed line is the RUMP simulation of the cementite phase.

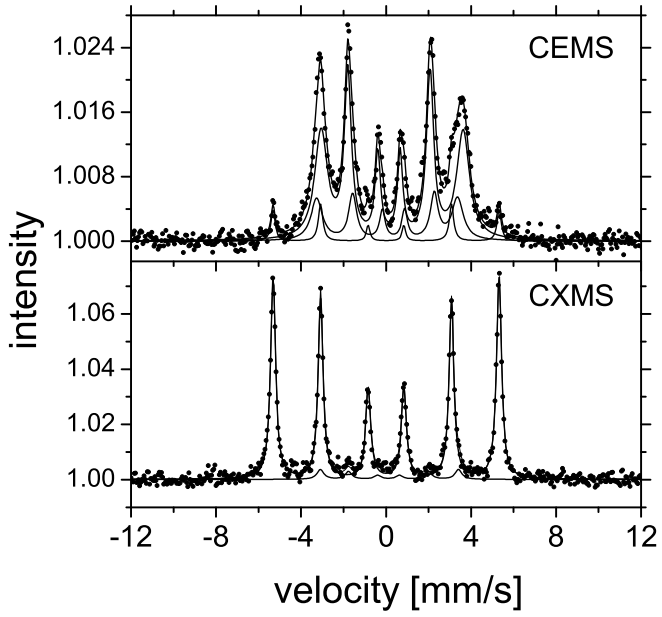

Figure 5.15: CEM (top) and CXM (bottom) spectra of the 16×16 meandered sample in 2 bar CH_4.

nearest neighbors, and Fe(II) with 2 C and 12 Fe nearest neighbors [39]. The CXM spectrum, with an information depth of the order of 10 μm, reveals that only about 10%

of the relative phase fraction can be attributed to the carbide phase, indicating that the θ-Fe_3C layer is about 1 μm thick, in agreement with the calculated melting depth. All hyperfine parameters are shown in Table 5.3 and agree well with those reported in the literature [112]. X-Ray diffraction was carried out at three different grazing incidence

Table 5.3: Mössbauer parameters of the spectra shown in Fig. 5.15.

	Phase	IS [mm/s]	QS [mm/s]	HF [T]	fraction [%]
CEMS	Fe_3C(I)	0.21	0.075	20.72	66(3)
	Fe_3C(II)	0.20	-0.15	20.56	31(2)
	α-Fe	0.0	0.0	33	3(1)
CXMS	Fe_3C	0.20	0.003	20.4	9.7(2)
	α-Fe	0.0	0.0	33	90.3(2)

angles (5°, 10°, 15°) to obtain qualitative information on the crystallographic morphology of the carburized layer. The three indexed peaks in Fig. 5.16 correspond to the α-Fe phase and originate from the non-reacted substrate, while all other peaks can be assigned to the θ-Fe_3C phase [44]. Since the cementite phase is at the surface of the sample, the relative

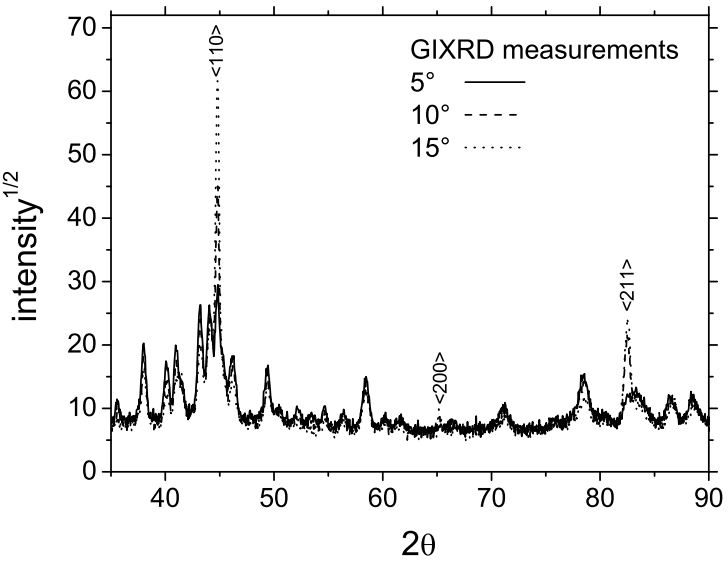

Figure 5.16: GIXRD diffractograms of the 16×16 scan in CH_4 taken at three different grazing incidence angles (5°, 10°, 15°): the indexed peaks correspond to the iron substrate, all other peaks belong to the cementite phase.

intensity of the Fe_3C peaks decreases with increasing incidence angle, i.e. with increasing X-ray penetration depth. Besides, no other carbide can be detected at larger depth, in agreement with the CXMS measurement, indicating the good degree of homogeneity of the layer. The possible mechanism governing the formation of the cementite layer can be

explained with the help of the Fe-C temperature-carbon activity phase diagram reported in Fig. 5.17. Due to the high temperature reached during the laser irradiation (>4000 K

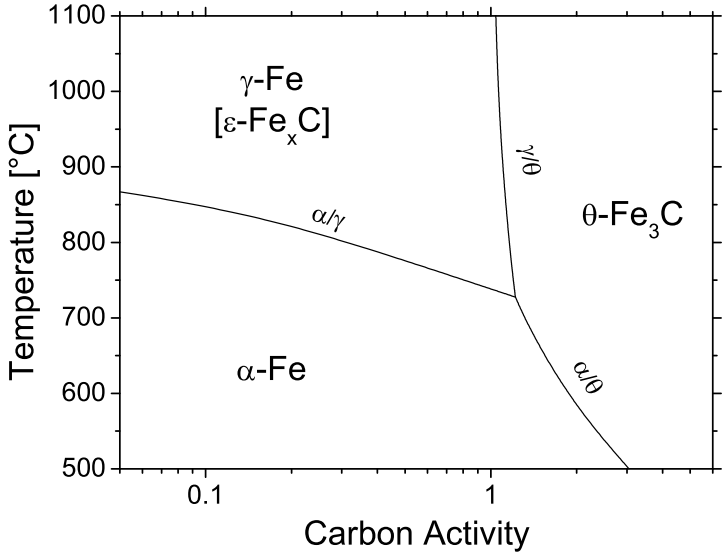

Figure 5.17: Temperature-carbon activity phase diagram of the Fe-C system (data from [42]).

at a laser fluence of 4 J/cm^2, see Fig. 3.2), the system, that initially is at the lower left-hand corner of the phase diagram, can rapidly move into the γ-Fe region. However, the high quenching rates ($\sim 10^9$ K/s) obtained with excimer laser processes rapidly bring the system back to the α-Fe region. As the number of pulses increases, more carbon is incorporated in the sample and the system gradually moves towards the higher carbon activity side. Eventually it may cross the steep γ/Fe$_3$C phase boundary in the direction of the cementite, where no γ-Fe is present, cooling in the Fe$_3$C region. When the carbon incorporated in the iron matrix has reached the value of 25 at.%, the cementite phase will grow inside the iron substrate leading to the formation of a homogeneous Fe$_3$C coating. The transition carbides, due to their unstable nature, are not included in the carbon activity phase diagram, but we observed in the previous section that the γ-Fe(C) phase is "coupled" to the ϵ phase (their existence is simultaneous) and the γ-Fe region in Fig. 5.17 might be correlated to the ϵ-Fe$_x$C phase (reported in square brackets).

Chapter 6

The aluminum substrate

Laser nitriding of aluminum substrates has been studied in the last decades with particular emphasis on the morphological, structural and tribological properties [113, 114, 115], but so far no effort has been made to understand the mechanisms of nitrogen incorporation and mass transport. In order to investigate the influence of the experimental parameters on the nitriding efficiency and the mass transport, a systematic study on the effects of the laser irradiation of pure Al substrates in nitrogen atmosphere has been carried out, revealing the strong influence of the laser fluence on the mass transport properties [98, 116]. Even if aluminum carbide is technologically not as attractive as AlN, laser irradiation in methane atmosphere has been performed, demonstrating that the carbon incorporation is effective.

6.1 Laser nitriding of aluminum

The following sections will describe the results of the laser irradiation of aluminum substrates in nitrogen atmosphere as a function of the laser fluence, the number of pulses and the gas pressure. Special emphasis will be given to the mass transport mechanism, revealing how the migration of nitrogen is strongly correlated to the laser-induced temperature of the substrate.

6.1.1 Preliminary investigations: the laser fluence dependence

Fig. 6.1 depicts the nitrogen depth profiles of the Al samples irradiated as single spot with 64 laser pulses in 1 bar N_2, at fluences ϕ ranging from 1 to 4 J/cm^2, in steps of 0.5 J/cm^2. Below 2 J/cm^2, the maximum nitrogen concentration is lower than 10 at.% and the thickness of the nitrided layer is of the order of 100 nm. Between 2 and 3 J/cm^2, diffusion-like profiles (i.e. exponential decays analogous to the nitrogen profiles in iron, see section 5.1) are observed: the nitrogen concentration at the surface is higher than 30 at.% and the thickness of the nitrided layer exceeds 600 nm. Since the nitriding efficiency can be measured by the mean nitrogen concentration and/or by the average thickness of the nitrided layer, the nitriding process in Al becomes effective at a laser

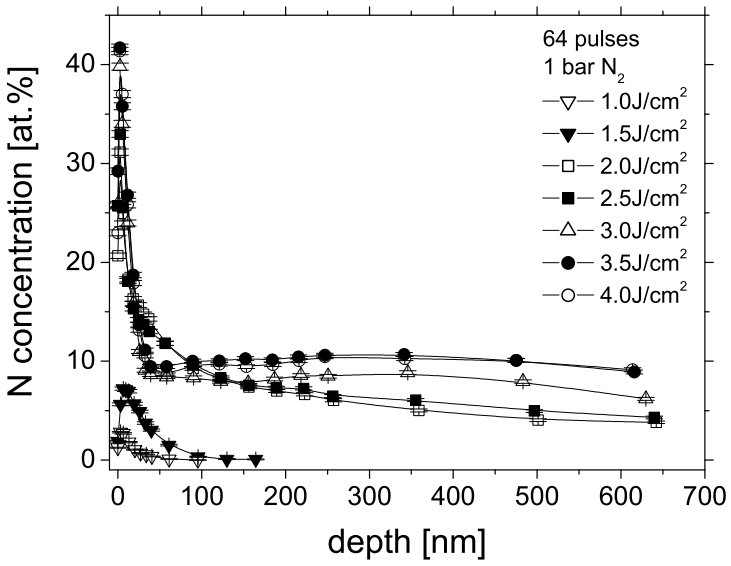

Figure 6.1: Nitrogen depth profiles obtained after irradiation with 64 pulses in 1 bar N_2 at laser fluences ranging from 1 to 4 J/cm^2.

fluence of about 2 J/cm^2. Above 3 J/cm^2, roughly homogeneous nitrogen profiles are formed within the investigated depth. Sharp nitride peaks with an average thickness of a few tens of nanometers appear on the surface of these samples: they are attributed to the "fall-out" (plasma re-condensate) of AlN clusters, most probably formed in the laser-induced plasma. The supersaturated Al vapor on the sample surface might facilitate the chemical reaction between Al and N as already pointed out in section 3.3. In order to better understand the nature of the fluence dependence across $\phi = 3$ J/cm^2 we have studied in more detail the nitriding effect at 2 J/cm^2 and at 4 J/cm^2. The differences are strongly correlated with the maximum temperature induced in the irradiated sample. According to the thermal simulations, as reported in Fig. 6.2, at 4 J/cm^2 the Al surface reaches the temperature of 3800 K: this value is higher than the dissociation temperature of AlN (2400 K at 1 bar N_2, but it increases with the ambient gas pressure [48]) and the melting point of AlN (3070 K [38]), while at 2 J/cm^2 the maximum surface temperature is about 2000 K, i.e. higher than the melting point of pure Al, but insufficient to dissolve the AlN. This aspect will be analyzed extensively in the following sections.

6.1.2 Mass transport mechanism at $\phi = 4$ J/cm^2

The depth profiles of the samples irradiated at 4 J/cm^2 in 1 bar N_2 are shown in Fig. 6.3. The nitrogen concentrations are rather homogeneous, increasing monotonically with the number of laser pulses up to the mean value of 14.7 at.% after 256 shots. The average nitrogen content drastically increases if the irradiation at 4 J/cm^2 is performed in higher ambient gas pressure. Fig. 6.4 reports the nitrogen profiles obtained at $\phi = 4$ J/cm^2 in 6 bar N_2. After 256 pulses, the homogeneous (within the experimental errors) N

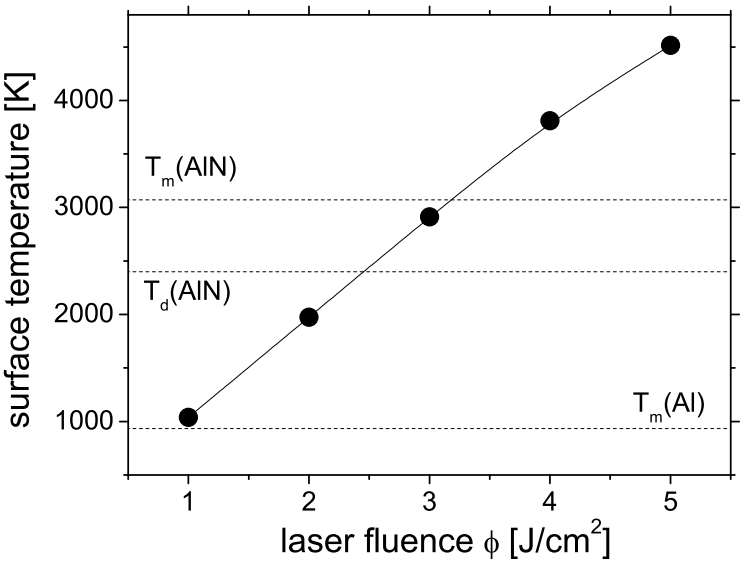

Figure 6.2: Simulation of the maximum Al surface temperature vs. the laser fluence. The dashed lines represent the melting point of Al, the dissociation and the melting points of AlN, respectively (from bottom to top).

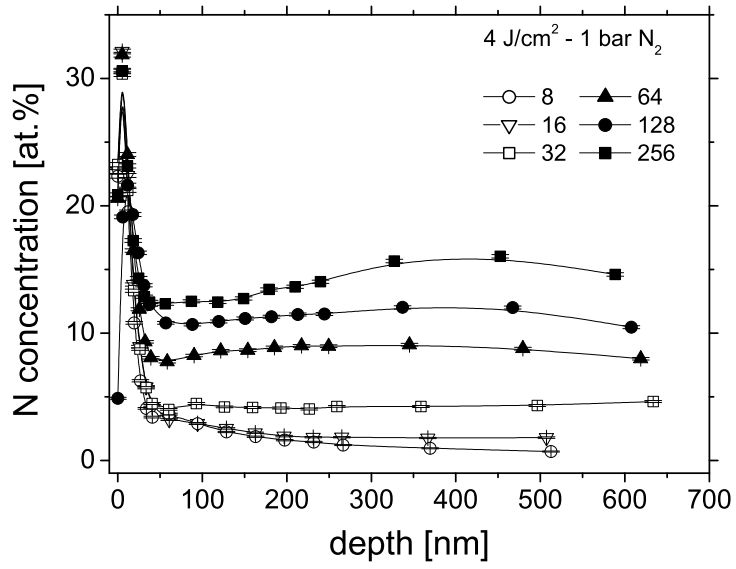

Figure 6.3: Nitrogen depth profiles after irradiation in 1 bar N_2 at a fluence of 4 J/cm^2 and various numbers of laser pulses.

concentration reaches the value of ~ 48 at.%, i.e. very close to the stoichiometry of AlN. According to the temperature simulations, at a laser fluence of 4 J/cm^2 the aluminum surface exceeds the melting point of AlN for about 80 ns and remains liquid for about

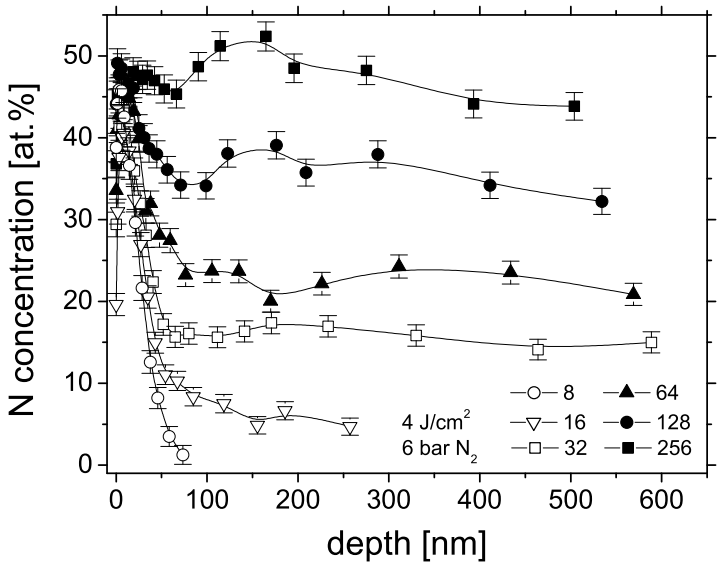

Figure 6.4: Nitrogen depth profiles after irradiation in 6 bar N_2 at a fluence of 4 J/cm^2 and various numbers of laser pulses.

800 ns, as shown in Fig. 6.5. During the melting time, atomic nitrogen can be in solution

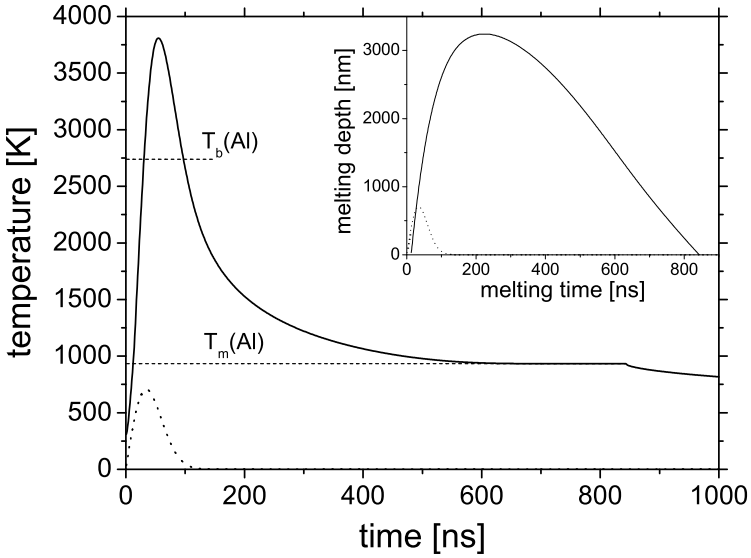

Figure 6.5: Time evolution of the surface temperature of pure Al irradiated at 4 J/cm^2. The inset shows the melting depth vs. the melting time (the dashed curves are the duration of the laser pulse).

in the liquid Al up to the solubility limit of few atomic percent (see Fig. 2.4), and can form

AlN as the temperature of the liquid drops to the melting point of pure Al. When the solidification temperature is reached, all the nitrogen in the sample will be in the nitride form, since no N solubility is possible in solid Al. However, during the cooling of the liquid some atomic nitrogen may segregate [117] at the moving solid-liquid interface or it may form N_2 molecules that will eventually outgas, being chemically inert and very stable [43]. The segregation process is strongly affected by the velocity v_{sl} of the solid-liquid interface during the cooling (the slower is the solid/liquid interface, the stronger is the segregation, see section 7.2.2): according to the simulations, at 4 J/cm^2 the value of v_{sl} is about 7 m/s, while at 2 J/cm^2 the calculation leads to $v_{sl} \sim 12$ m/s and the segregation should be less effective. The measured nitrogen depth profiles can be attributed to two distinct and competing effects: (i) an inward nitrogen flux due to the plasma-substrate coupling, leading to the nitrogen incorporation, and (ii) an outgassing flux due to the nitrogen segregation/recombination into N_2 molecules. It is reasonable to assume that the average nitrogen take-up per pulse S_{in} [at.% pulse^{-1}] caused by the inward flux increases with the abundance of atomic nitrogen in the laser-induced plasma and therefore with the ambient gas pressure. On the other hand, the outgassing rate should scale with the nitrogen concentration c_N [at.%] inside the sample (the more nitrogen exceeds the solubility limit, the larger is the outgassing). Therefore the rate of nitrogen loss per pulse due to the outgassing flux can be written as $S_{out} = c_N/l$, where the proportionality constant $1/l$ [pulse^{-1}] represents the outgassing rate. The overall change of the nitrogen concentration vs. the number of laser pulses m is then:

$$\frac{dc_N}{dm} = S_{in} - S_{out} = S_{in} - c_N/l, \tag{6.1}$$

and the solution of this differential equation is easily obtained:

$$c_N(m) = S_{in}\, l \left(1 - e^{-m/l}\right). \tag{6.2}$$

The average nitrogen contents (neglecting the sharp surface peaks) vs. the number of laser pulses in 1 bar and 6 bar N_2 are shown in Fig. 6.6 (symbols) with the corresponding fits according to Eq. (6.2) (lines). The value of the outgassing rate $1/l$ is 0.0115 for the irradiation in 1 bar N_2 and 0.010 for the irradiation in 6 bar N_2, revealing its weak dependence on the ambient gas pressure, while the value of S_{in} increases with the nitrogen pressure. In order to better understand its dependence, we performed laser irradiations with 256 pulses at various pressures between 1 bar and 10 bar. The average nitrogen contents vs. the pressure are fitted according to Eq. (6.2) with fixed $m = 256$ and using the mean value of $1/l = 0.0107(8)$. The results are shown in Fig. 6.7; the inset reports the RNRA nitrogen depth profiles at the different pressures. The increase of S_{in} with the ambient pressure p can be linearly fitted in the region 1-6 bar:

$$S_{in} = A + B\, p, \tag{6.3}$$

obtaining $A = 0.087(7)$ [at.% pulse^{-1}] and $B = 0.064(2)$ [at.% pulse^{-1} bar^{-1}]. Using Eq. (6.2) and Eq. (6.3), the average nitrogen content in the aluminum matrix after excimer laser irradiation at 4 J/cm^2 can be estimated as a function of the ambient gas pressure p and the number of laser pulses m as follows:

$$c_N(m, p) = (a_1 + a_2 p)(1 - e^{-m/l}), \tag{6.4}$$

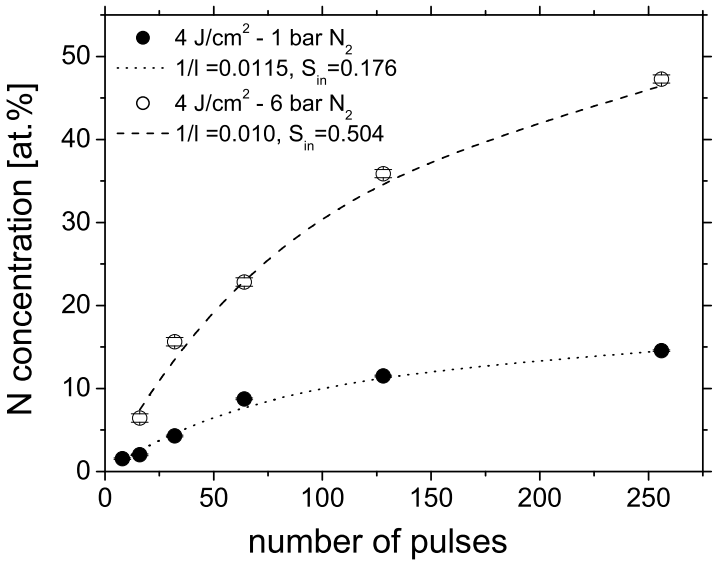

Figure 6.6: Average nitrogen content as a function of the number of laser pulses at 4 J/cm^2 in 1 bar N_2 (solid symbols) and in 6 bar N_2 (open symbols) with the corresponding fits according to Eq. (6.2).

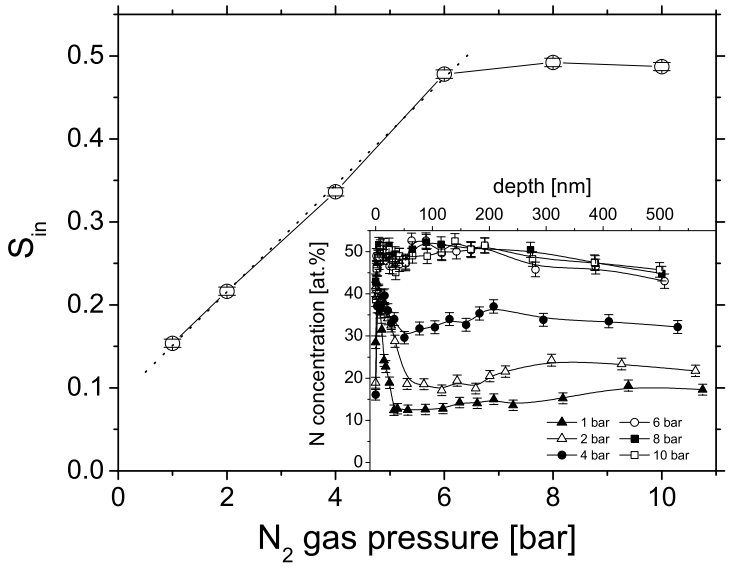

Figure 6.7: Experimental dependence of the parameter S_{in} on the ambient gas pressure. The dashed line is the linear fit in the region 1-6 bar. The inset depicts the corresponding nitrogen depth profiles used to extrapolate the values of S_{in}.

with $a_1 = A\ l = 8.1(8)$ [at.%] and $a_2 = B\ l = 6.0(4)$ [at.% bar^{-1}]. The presented phenomenological model describes the take-up mechanism in a wide range of ambient

pressures and number of laser shots. From the experimental evidence it can also be concluded that the melting time is long enough to homogenize the nitrogen distribution (unfortunately, no data about the diffusion of N in Al are available up to date).

6.1.3 Mass transport mechanism at $\phi = 2$ J/cm^2

The nitrogen depth profiles as a function of the number of laser pulses in the samples irradiated at 2 J/cm^2 in 1 bar N_2 are shown in Fig. 6.8. Diffusion-like profiles with

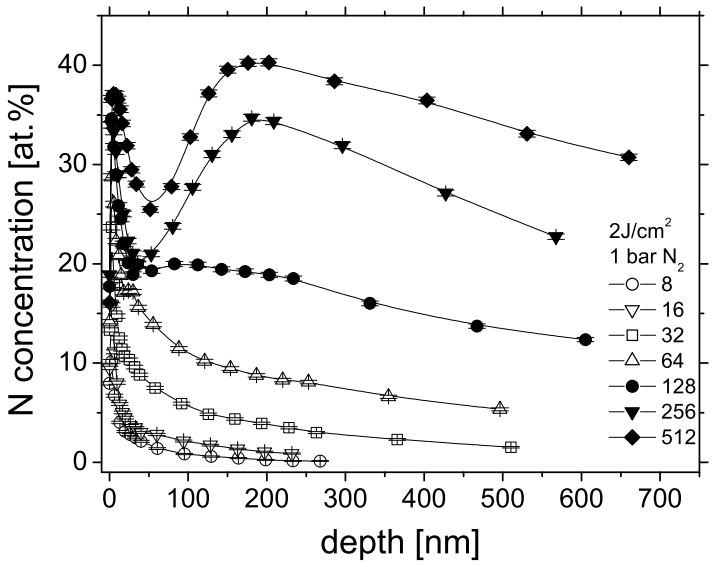

Figure 6.8: Nitrogen depth profiles after irradiation in 1 bar N_2 at a fluence of 2 J/cm^2 and various numbers of laser pulses.

increasing nitrogen content and nitrided thickness are formed as the number of laser shots increases from 2 to 64. A gradual modification of the profile shape is induced for a higher number of pulses, and the significant nitrogen content of ~ 40 at.% is obtained. The simulation of the surface temperature and the evolution of the melting depth after irradiation of pure Al at 2 J/cm^2 are shown in Fig. 6.9. The melting time is about 230 ns and the maximum temperature reached at the surface is about 2000 K, i.e. higher than the melting point of aluminum, but not high enough to dissociate or melt the AlN. This feature seems to determine the mass transport mechanism at this fluence. As verified by Transmission Electron Microscopy (TEM) on the samples irradiated 256 times at 2 J/cm^2 in 1 bar N_2, small AlN particles embedded in the Al matrix are formed, with an average radius of the order of a few tens of nanometer (Fig. 6.10). The temperature reached in the sample during the laser irradiation is not sufficient to destroy these particles and they can move inside the liquid Al. In such a case, it is well established that the driving forces of the mass transport mechanism originate from the temperature and the chemical gradients [5] (gravitation-buoyancy plays a negligible role). For small particles floating inside a liquid, the chemical gradient is simply ∇n_p, where n_p is the number of particles

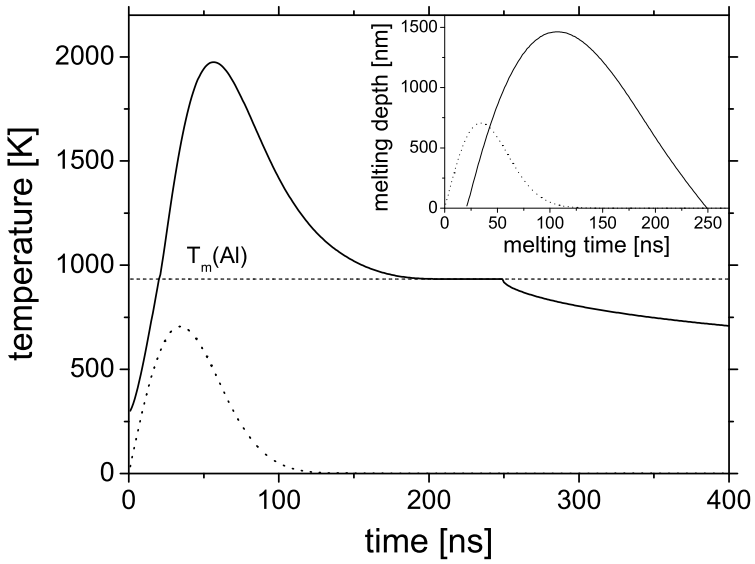

Figure 6.9: Time evolution of the surface temperature of pure Al irradiated at 2 J/cm^2. The inset shows the melting depth vs. the melting time (the dashed curves represent the duration of the laser pulse).

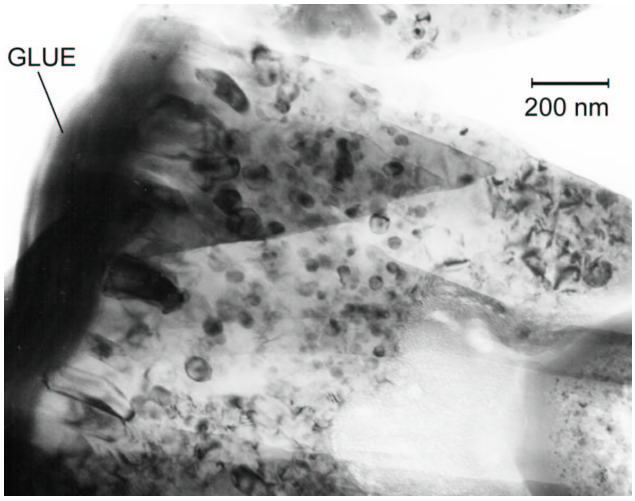

Figure 6.10: TEM picture of sample irradiated 256 times at 2 J/cm^2 in 1 bar N_2. The small dark dots are the AlN grains.

per unit volume, and the diffusion mechanism is governed by the Brownian motion, with the diffusion constant D_{br} depending on the temperature T of the fluid and on the radius r of the solid particles [118, 119]:

$$D_{br} = \frac{k_B T}{6\pi\eta r}. \tag{6.5}$$

η is the dynamic viscosity of the fluid and k_B is the Boltzmann constant. At a temperature of about 2000 K, with the viscosity of liquid Al being 10^{-3} Pa·s [120] and a particle radius

of 10 nm we obtain $D_{br} \sim 0.15$ nm^2/ns. The particle flux J_{br} (i.e. the number of particles crossing the unit area per unit time) due to the Brownian motion is then:

$$J_{br} = -D_{br}\frac{\partial n_p}{\partial z}. \tag{6.6}$$

The transport mechanism related to the temperature gradient is called thermophoresis [121, 122]. It produces a drift of the floating particles in the direction opposite to the temperature gradient. The drift velocity for solid particles in a liquid has the following form [116]:

$$v_{th} = -\frac{2\eta}{\rho T(2+\kappa_i/\kappa_e)}\frac{\partial T}{\partial z}, \tag{6.7}$$

where κ_i and κ_e are the thermal conductivities of the particle and the liquid, respectively. For a temperature gradient of $\sim 10^9$ K/m (see Fig. 6.11) and using $\kappa_e = \kappa_i$ for simplicity, at 2000 K we have $v_{th} \sim 0.12$ m/s. The corresponding particle flux J_{th} is simply

$$J_{th} = v_{th} n_p. \tag{6.8}$$

The total particles flux can be written as:

$$J = J_{br} + J_{th} = -D_{br}\frac{\partial n_p}{\partial z} + v_{th} n_p, \tag{6.9}$$

and using the mass conservation law we obtain:

$$\frac{\partial n_p}{\partial t} = -\nabla \cdot J = -\frac{\partial J}{\partial z} = \frac{\partial}{\partial z}\left(D_{br}\frac{\partial n_p}{\partial z} - v_{th} n_p\right), \tag{6.10}$$

which is a version of the one-dimensional drift-diffusion equation [118]. It should be noticed that the time scale of the diffusion process and the thermophoretic drift might differ. In fact, the diffusion lasts as long as the Al matrix is molten, i.e. for a time of the order of the melting time $t_m \sim 230$ ns. The thermophoretic drift depends on the temperature gradient $\frac{\partial T}{\partial z}$. The simulation of $\frac{\partial T}{\partial z}$ in the first 600 nm from the surface of the sample (i.e. the mean depth investigated by RNRA) is plotted in Fig. 6.11 as a function of the time (the same computer code used to plot Figs. 6.5 and 6.9 has been used). The full width at half maximum is about 45 ns, that represents the duration t_{th} of the thermophoretic drift. Eq. (6.10) was verified experimentally with some isotopic irradiations. Similarly to the notation used in section 5.1, the term m^*/k refers to m pulses in enriched ^{15}N gas followed by k pulses in natural nitrogen. Fig. 6.12 reports the nitrogen depth profiles (symbols) of the 256*/0, 256*/4, 256*/8 and 256*/16 irradiations. Eq. (6.10) was written according to the finite difference method and the numerical fit of the 256*/0 nitrogen depth profile was used as the initial condition. Since the number of particles per unit volume n_p is proportional to the nitrogen concentration c_N, the substitution of n_p by c_N in Eq. (6.10) is harmless. The surface boundary condition

$$\left.\frac{\partial c_N}{\partial z}\right|_{z=0} = 0 \tag{6.11}$$

was used to exclude any material flux through the surface of the sample. The evolution of the 256*/0 profile after 4, 8 and 16 laser pulses according to Eq. (6.10) is plotted

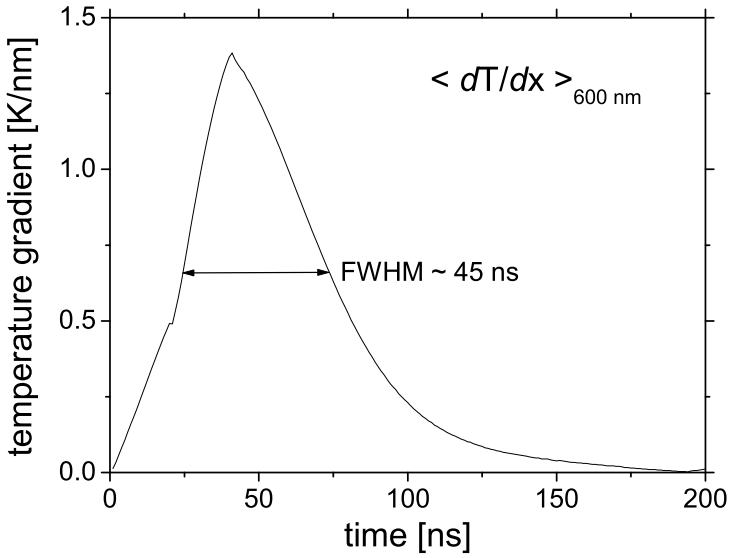

Figure 6.11: Time evolution of the temperature gradient averaged over 600 nm from the surface of the Al sample irradiated at 2 J/cm^2.

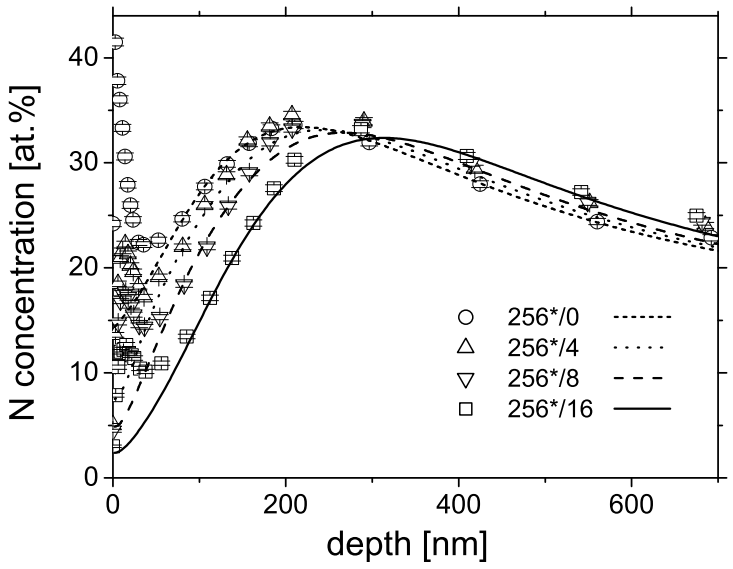

Figure 6.12: Nitrogen depth profiles of the isotopic experiments 256*/0 (○), 256*/4 (△), 256*/8 (▽), 256*/16 (□) at 2 J/cm^2 in 1 bar N_2 with the corresponding simulations according to Eq. (6.10).

(lines) in Fig. 6.12, showing excellent agreement with the experimental data. The values of $v_{th} = 0.10$ nm/ns, $t_{th} = 45$ ns, $D_{br} = 0.5$ nm^2/ns and $t_m = 230$ ns were used in the simulations as fitting parameters. The values of v_{th} and t_{th} are consistent with the

results obtained from the thermal simulations. The diffusion constant $D_{br} = 0.5$ nm^2/ns corresponds to a particle radius of ~ 2 nm, which is somewhat smaller than the average dimension observed with TEM. However, the analytical technique used to measure the nitrogen depth profiles involves the use of a charged ion beam that is subject to straggling. According to the model of Lindhard and Scharff (Eq. (4.14) and Fig. 4.8), the straggling of a 430 keV proton beam in aluminum at a depth of 170 nm is of the order of 21 nm. This value corresponds to an apparent diffusion length of $\sim \sqrt{D_{app} t_m}$. If $t_m = 230$ ns, we obtain D_{app}=1.9 nm^2/ns. Due to the thermophoretic drift, after 16 laser pulses the nitrogen profile moves to $170 + 16\ v_{th}\ t_{th} \simeq$ 240 nm and the straggling becomes about 25 nm, corresponding to an apparent diffusion coefficient $D_{app} = 2.7$ nm^2/ns. Therefore, the RNRA depth resolution, especially at large depths, can be inadequate to measure small diffusion constants. This may explain the discrepancy between the measured and the predicted value of D_{br}. However, the beam straggling is smaller than the overall thermophoretic drift, even after 4 pulses, and this effect can be clearly distinguished. The entire mass transport process at 2 J/cm^2 is schematically summarized in Fig. 6.13 and the main thermophysical parameters of the Al-AlN system are reported in Table 6.1. The modeling of the nitrogen depth profiles as a function of the number of laser pulses requires the detailed knowledge of the nitrogen incorporation mechanism, that might depend on the properties of the surface (roughness, reflectivity, nitrogen content, etc.) and therefore on the number of pulses itself, with a high degree of complexity.

Table 6.1: List of the main thermal and physical parameters of Al and AlN.

Parameter	Symbol	Value	Ref.
Al melting temperature	T_m(Al)	933.5 K	[43]
Al boiling temperature	T_b	2740 K	[43]
Al latent heat of fusion	L_m	10.5 kJ/mole	[43]
Al latent heat of evaporation	L_{ev}	296 kJ/mole	[43]
Al reflectivity (at $\lambda = 308$ nm)	R_0	$\simeq 0.5$	[a]
Al absorption length (at $\lambda = 308$ nm)	$1/\alpha$	7 nm	[43]
Al molar mass	M	27 g	[43]
Al density	ρ_{Al}	2.7 g/cm^3	[43]
liquid Al viscosity	η	10^{-3} Pa s	[120]
AlN melting temperature	T_m(AlN)	3070 K	[38]
AlN dissociation temperature	T_d	2400 K	[48]
AlN density	ρ_{AlN}	3.25 g/cm^3	[43]

[a] Measured.

6.1.4 Crystal structures and mechanical properties

The crystalline structure of the nitrided layers was investigated in the samples irradiated at 2 J/cm^2 and 4 J/cm^2 in 1 bar N_2 with 256 pulses. The diffractograms reported in Fig. 6.14 show the formation of polycrystalline AlN with the wurtzite structure, as

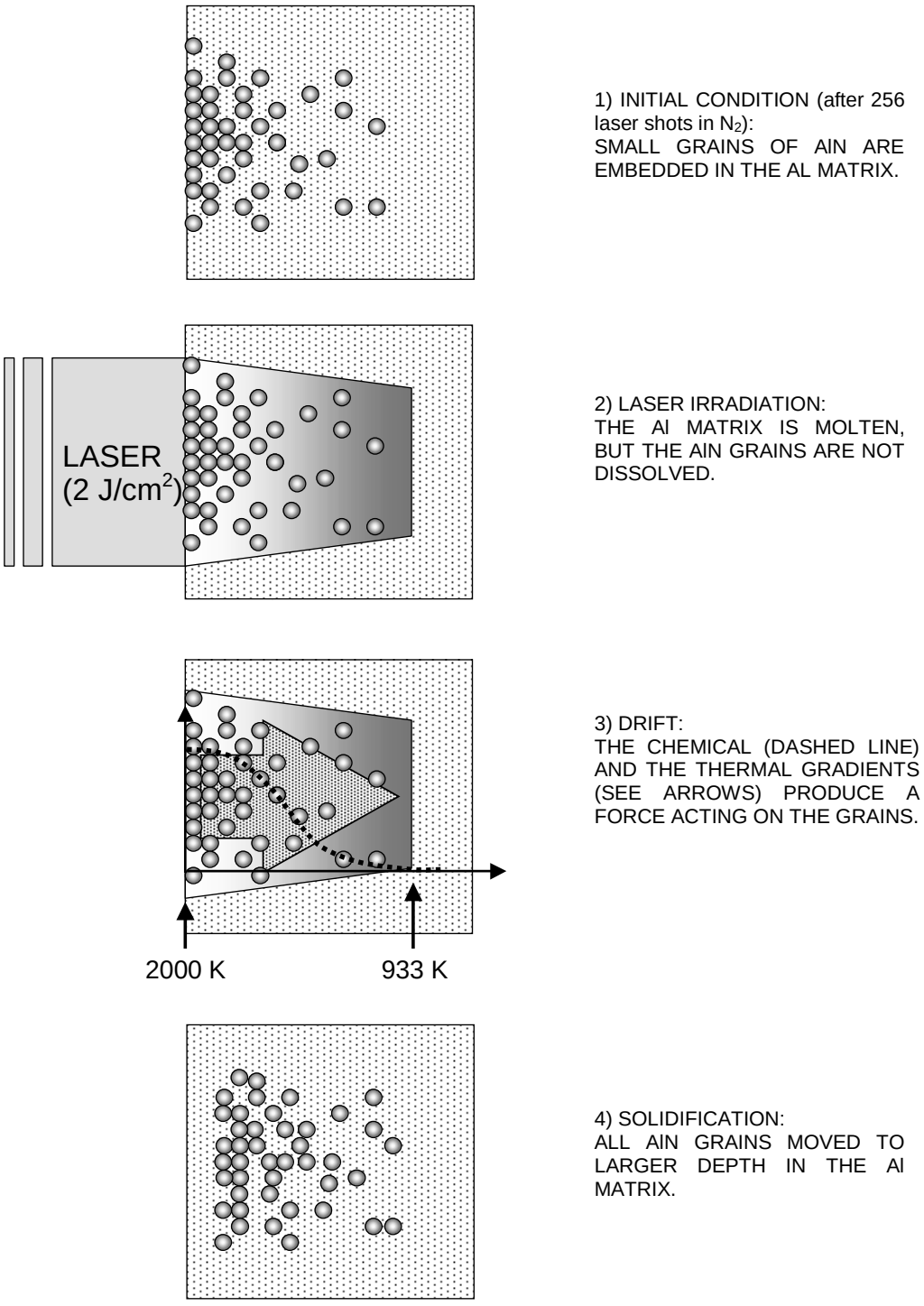

Figure 6.13: Schematic view of the mass transport mechanism of AlN in the Al matrix during the irradiation at a laser fluence of 2 J/cm^2.

revealed by the Rietveld refinements. The lattice parameters of the Al matrix and the AlN phase reported in Table 6.2 are in good agreement with the bulk values [44]. No evidence of oxides, NaCl-type or zincblende-type AlN was found (the latter is considered a non-equilibrium crystal structure: it was observed for GaN and InN, but only theoretically

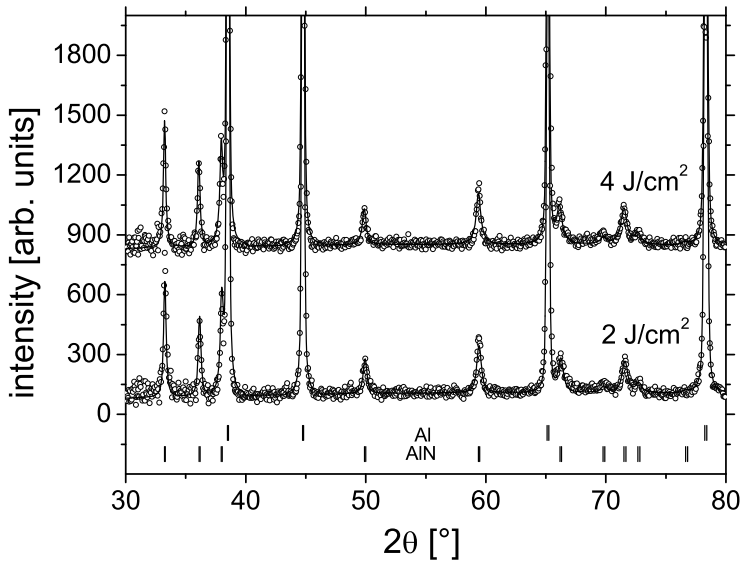

Figure 6.14: 1.5° GIXRD diffractograms of the Al sample irradiated at 2 J/cm^2 and 4 J/cm^2, with 256 pulses in 1 bar N_2. The continuous lines are the Rietveld refined fits and the small vertical bars correspond to the Bragg positions of the various crystallographic directions.

predicted for AlN [51, 123]). The mechanical properties of the irradiated samples have

Table 6.2: Lattice parameters obtained from the Rietveld refinements shown in Fig. 6.14. The parameter "u" is the fractional coordinate along the c axis of the AlN cell that determines the position of the nitrogen atoms in the wurtzite structure.

	Aluminum	Aluminum Nitride		
	S.G. $Fm\bar{3}m$ (225)	S.G. $P6_3mc$ (186)		
	a [Å]	a [Å]	c [Å]	u
2 J/cm^2	4.0493(2)	3.1107(5)	4.969(1)	0.599(4)
4 J/cm^2	4.0493(2)	3.1130(5)	4.978(1)	0.599(4)

been investigated by nanoindentation. The values of the hardness reported in Fig 6.15 have been taken at the indentation depth of 100 nm for all profiles in order to compare the results consistently. A large increase in the surface hardness for increasing number of laser shots and nitrogen pressure has been observed in all the nitrided specimens, regardless of the laser fluence (only in the sample irradiated at 4 J/cm^2 in 10 bar nitrogen we noticed a decrease attributed to the surface roughness). The highest value of 5 GPa, i.e 10 times larger than the untreated aluminum substrate, has been observed in the sample irradiated at 4 J/cm^2 in 8 bar N_2. The correlation between the nitrogen content and the surface hardness is evidenced in Fig. 6.16 as function of the gas pressure, revealing how the mechanical properties are closely connected to the formation of the nitride. A similar feature was observed in the iron substrates irradiated in nitrogen [31].

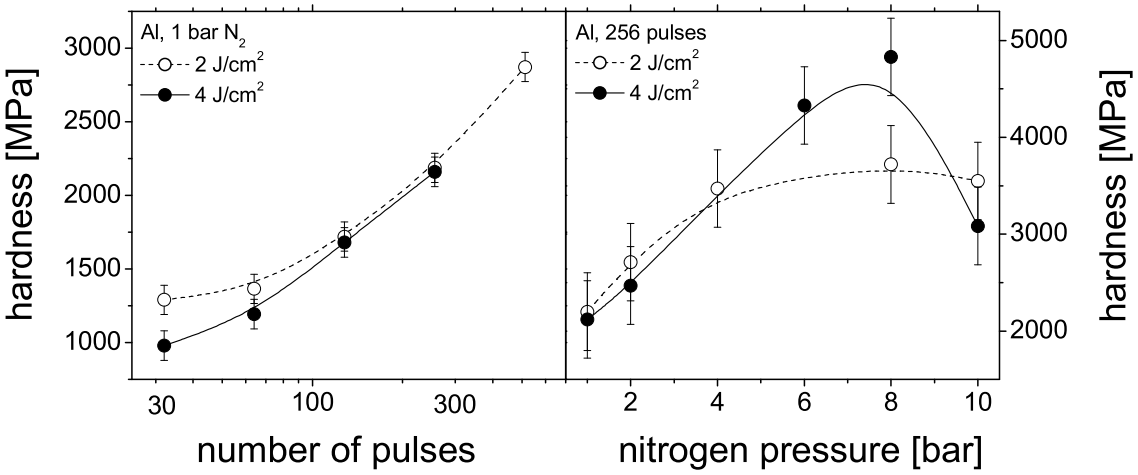

Figure 6.15: Hardness of the Al samples nitrided at 2 J/cm^2(○) and 4 J/cm^2(●) as a function of the number of laser shots (left) and the nitrogen pressure (right).

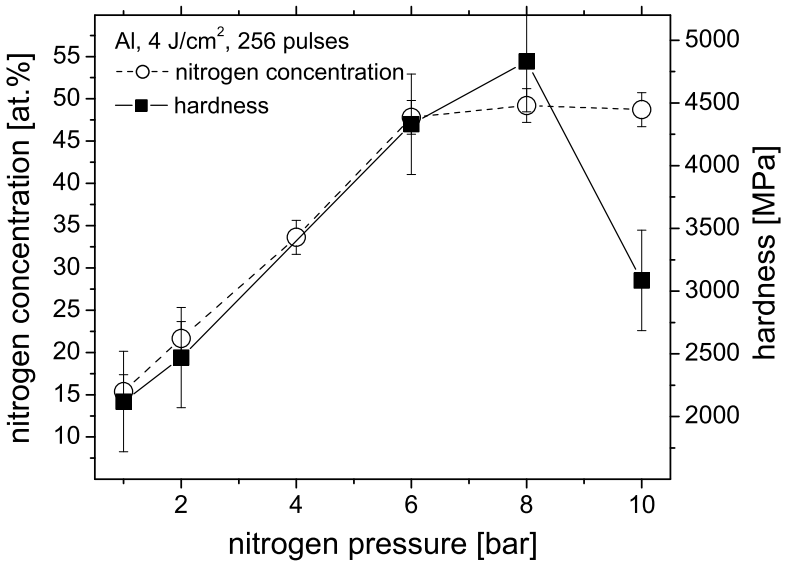

Figure 6.16: Correlation between the surface hardness and the average nitrogen content in the samples irradiated with 256 pulses at 4 J/cm^2.

6.2 Laser irradiation in methane atmosphere

Aluminum carbide (Al_4C_3) does not meet the technological "fortune" of aluminum nitride. Few publications and little attention has been given to this compound in comparison to its nitride counterpart. Nevertheless the laser irradiation of aluminum substrates in methane

atmosphere has been performed in order to demonstrate that the carbon incorporation is effective. The sample treated with the 16×16 meander scan at the laser fluence of

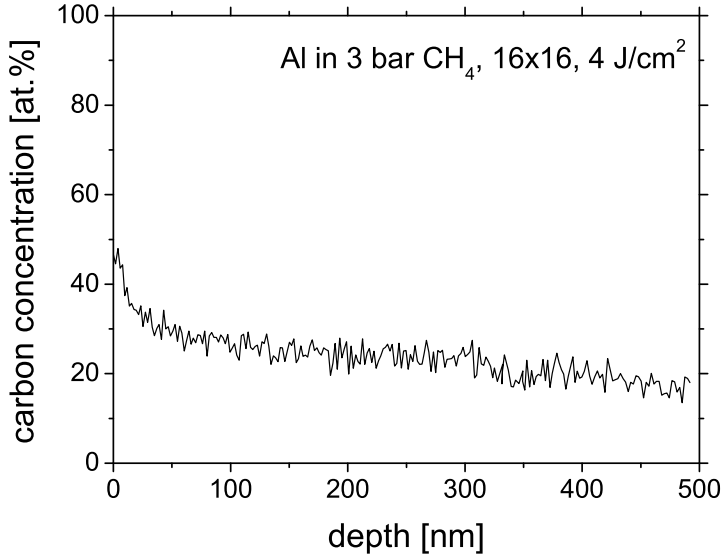

Figure 6.17: RBS carbon depth profile of the aluminum sample meandered in 3 bar CH_4.

4 J/cm^2 in 3 bar CH_4 has been analyzed by means of RBS, XRD and nanoindentation. The RBS measurement revealed an average carbon content of about 20 at.%, as shown in Fig. 6.17. The nanoindentation measurement showed a considerable increase of the

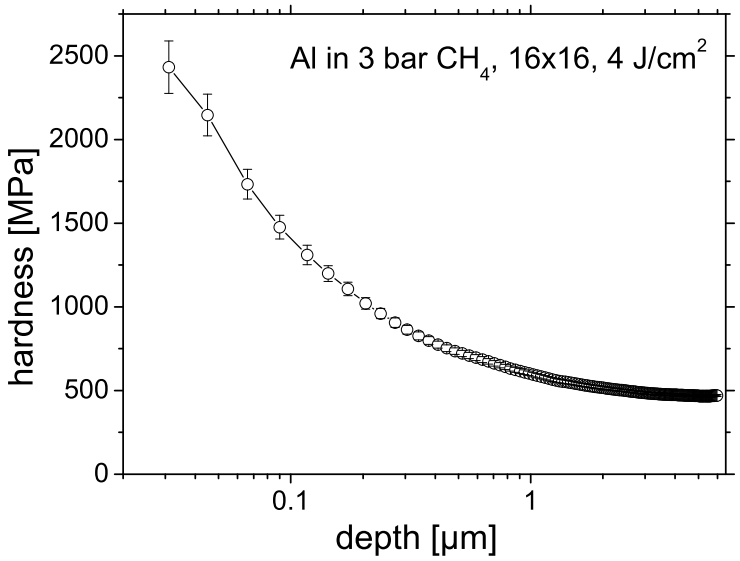

Figure 6.18: Hardness profile of the laser carburized Al substrate.

surface hardness after the treatment (about 4 times larger than the virgin substrate) as reported in the Fig. 6.18. Nevertheless, very poor crystallinity has been observed by GIXRD (with incidence angle of 1°): a broad peak centered at the Bragg angle $2\theta = 31.6°$ (7.2° FWHM) appears in the diffraction patter of the irradiated specimen, as reported in Fig. 6.19. The position of the Bragg reflection is in good agreement with the value of the most intense diffraction peak of crystalline Al_4C_3 (<012> peak at $2\theta = 31.74°$), suggesting the formation of amorphous aluminum carbide. The poor crystallinity is attributed to the more complex atomic arrangement of the the Al_4C_3 phase compared to AlN. The rapid quenching rate (see Fig. 6.11) obtained with nanosecond laser pulses might hinder the long-range atomic order. Thus, even if the basic Al_4C_3 arrangement is locally formed, the crystallites are not large enough to give a clear XRD signal, and only the main interatomic distance is observed (i.e. the most intense XRD peak). Similar effects have been found in the silicon substrates irradiated in nitrogen atmosphere (see section 7.2), where the stoichiometry of the nitride phase is Si_3N_4 (the role of Al atom in the aluminum carbide is played by the N atom is the silicon nitride).

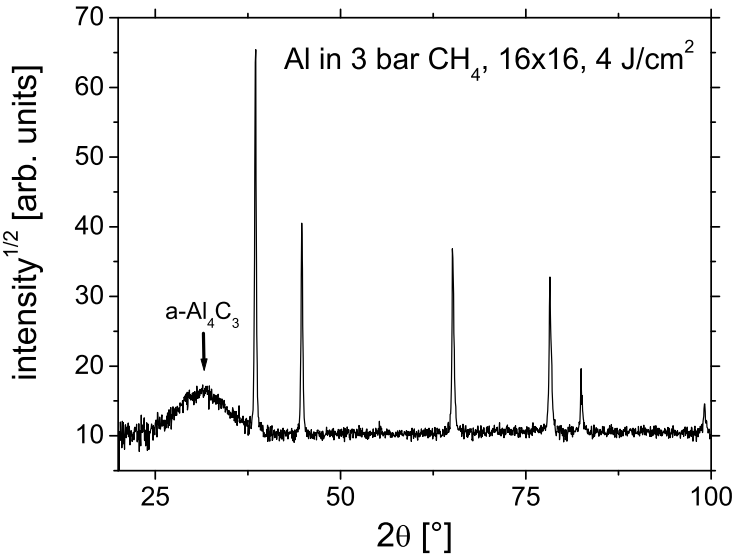

Figure 6.19: 1° GIXRD patter of the laser carburized sample. The broad peak at $2\theta = 31.6°$ indicates the formation of amorphous Al_4C_3, all other peak belong to the fcc Al matrix.

Chapter 7

The silicon substrate

The following sections will show how the laser irradiation of single-crystalline silicon substrates in controlled nitrogen and methane atmospheres leads to the formation of carbide and nitride phases [124]. The analysis has been performed mainly (but not only) by Extended X-ray Absorption Fine Structure (EXAFS) due to the high sensitivity of this technique to the local atomic environment. As already described in section 4.5, the EXAFS information is extracted from the wiggles of the X-ray absorption coefficient above the absorption edge. Fig. 7.1 shows the fine structure oscillations (weighted with factor k^2) of the virgin silicon substrate, commercial β-SiC powder, commercial α-Si_3N_4 powder and the silicon samples irradiated with 256 laser pulses in CH_4 and in N_2.

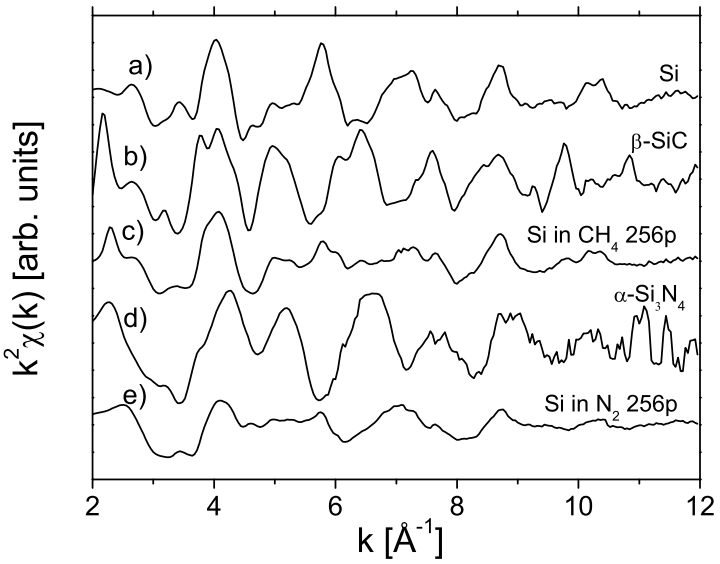

Figure 7.1: Fine structure oscillations weighted with the k^2 factor of: a) Si <100>, b) β-SiC, c) Si irradiated in CH_4 with 256 pulses, d) α-Si_3N_4, e) Si irradiated in N_2 with 256 pulses.

7.1 Laser irradiation in methane atmosphere

Aiming to the formation of SiC, the influence of the number of laser pulses on the carbon incorporation into the silicon matrix has been investigated with the single spot treatment, using the raw laser beam (the homogenizer lens barely allows to reach the fluence of 4 J/cm^2, which is the threshold fluence to induce strong vaporization in the silicon substrate). As it will be shown, the synthesis of SiC is successful, but its optimization requires the investigation of other experimental parameters: thus, the effect of the meandering scan combined with the methane gas pressure will be described in section 7.1.2.

7.1.1 Influence of the number of pulses

The single spot laser treatments were performed at fixed laser fluence of 5 J/cm^2 in 2 bar CH_4, varying the number of laser shots between 2 and 256. The EXAFS oscillations of the laser-carburized samples were Fourier-transformed in the region 2 Å$^{-1} \leq k \leq$ 12 Å^{-1}. The resulting curve of the Si sample irradiated with 256 pulses is reported in Fig. 7.2. For comparison, the Fourier transform (FT) of the virgin silicon substrate and the β-SiC standard are reported as well. It is clear at a first glance that the laser-irradiated specimen

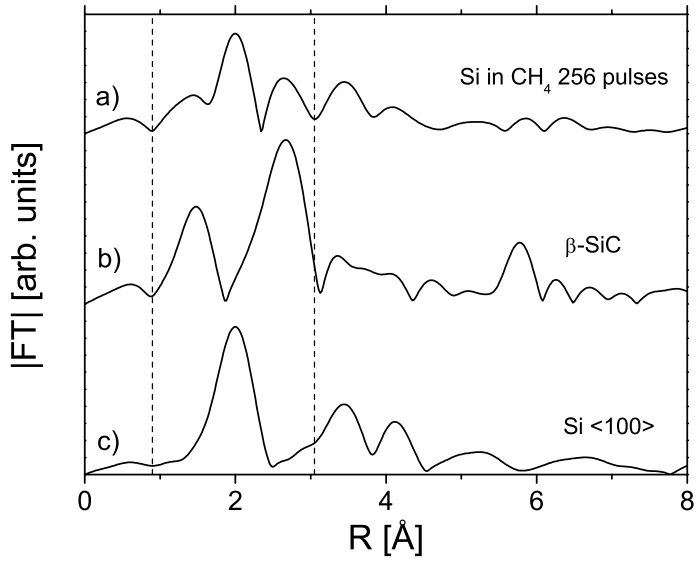

Figure 7.2: Fourier transform moduli of: a) Si sample irradiated in CH_4 with 256 pulses, b) β-SiC standard, c) virgin Si <100>. The dashed vertical lines delimit the BFT region.

is a mixture of the carbide phase and the non-reacted Si, since peaks belonging to both structures are superimposed. In order to have quantitative information, the back Fourier transform (BFT) analysis based on a three-shells fit has been carried out. The BFT was calculated in the region 0.90 Å $< R <$ 3.05 Å including the peaks corresponding to the first shell of SiC (C scatterer, peak at ∼1.5 Å), the first shell of Si (peak at ∼2.05 Å) and the second shell of SiC (Si scatterer, peak at ∼2.6 Å). The scattering amplitudes

and the phases of each shell were obtained from the standard specimens (pure Si and β-SiC) and loaded in the fits as initial parameters. Since the absorption edges of Si and SiC differ by 2 eV (1839 eV and 1841 eV, respectively), this energy correction has been introduced as a fixed parameter in the fitting procedure of the first and second shell of SiC. The oscillations extrapolated from the BFT of the silicon sample irradiated with 256 laser shots are shown in Fig. 7.3. They have been fitted according to Eq. (4.46) in

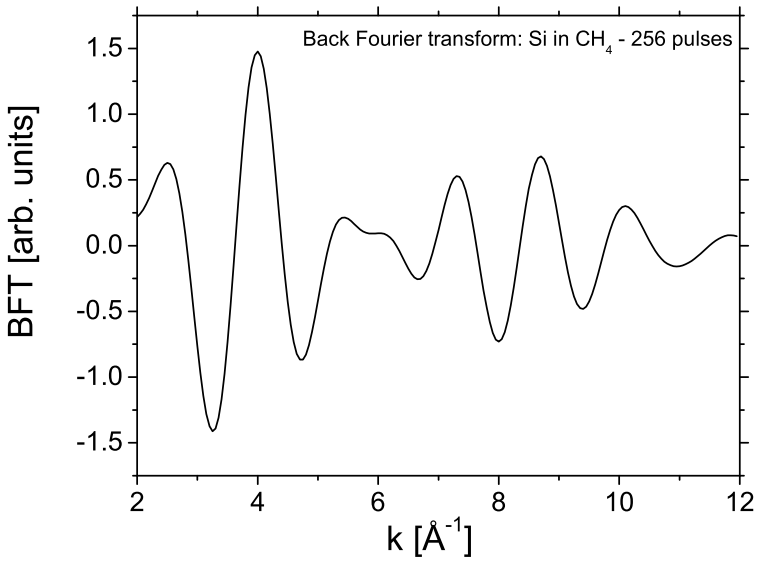

Figure 7.3: Back Fourier transform oscillations of the Si sample irradiated with 256 laser pulses in 2 bar CH_4.

order to obtain the radii, the occupancies and the disorder factors of the three shells. The disorder parameters $\Delta\sigma^2$, relative to the standards, were found to be less than 4×10^{-4} Å^2, confirming the good crystallinity of the laser-induced phases. To evaluate the Si to SiC phase ratio, the numbers of neighbors obtained from the analysis have been normalized with respect to the ideal values of the pure substances. There are four C neighbors at the distance of 1.89 Å in the first shell of SiC (in tetrahedral arrangements), four Si neighbors at the distance of 2.35 Å in the first shell of Si (in tetrahedral arrangements) and 12 Si neighbors at the distance of 3.08 Å in the second shell of SiC (in fcc configuration). The results of the fits are reported in Fig. 7.4 and Table 7.1. The radii of the shells are in good agreement with the predicted values, and the relative amounts of SiC calculated independently from each shell are very close, indicating the good morphology of the basic carbide structure. The fraction f_{Si} of non-reacted Si has been related to the fraction f_{SiC} of SiC simply as $f_{SiC} = 1 - f_{Si}$. To cross check the results of the fitting, we compared the weighted oscillations $k^2\chi(k)$ of the laser treated samples with the linear combination of the weighted oscillations of Si and β-SiC in the entire region 2 Å^{-1} $\leq k \leq$ 12 Å^{-1}. The result reported in Fig. 7.4 (solid symbol) shows an excellent agreement with the shells fitting, confirming once more the good degree of crystallinity of the laser-induced SiC. We point out that the relative amount of carbide phase seems to saturate at about 35% after 256 laser pulses and a higher number of laser shots would hardly lead to any

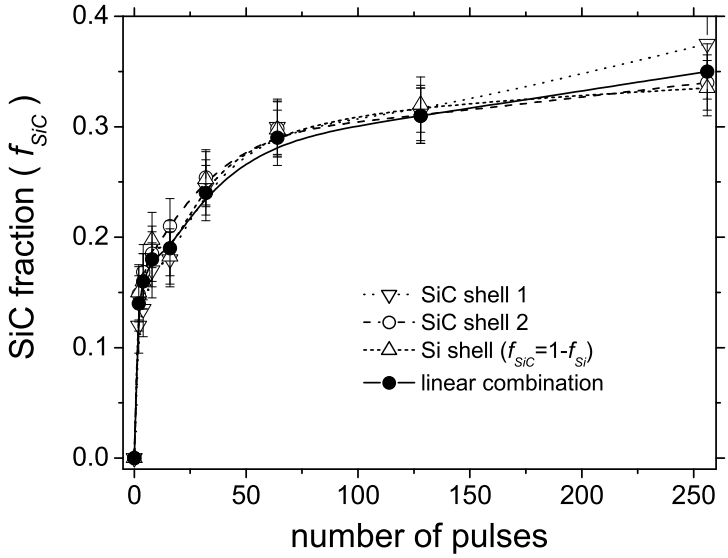

Figure 7.4: SiC phase fraction obtained from the EXAFS analysis as a function of the number of laser pulses: ($\bigtriangledown$) first shell of SiC, ($\circ$) second shell of SiC, ($\bigtriangleup$) first shell of Si, ($\bullet$) linear combination (see text).

Table 7.1: Three-shells fitting of the Si samples irradiated in CH_4: summary of the results.

Laser shots	Si-C (I shell)		Si (I shell)		Si-C (II shell)	
	N/4	R[Å]	N/4	R[Å]	N/12	R[Å]
2	0.120	1.90	0.850	2.35	0.148	3.11
4	0.135	1.88	0.840	2.35	0.168	3.11
8	0.170	1.89	0.802	2.35	0.185	3.09
16	0.180	1.89	0.818	2.35	0.210	3.09
32	0.245	1.89	0.748	2.35	0.254	3.08
64	0.300	1.89	0.703	2.35	0.298	3.08
128	0.313	1.89	0.680	2.35	0.310	3.07
256	0.375	1.86	0.665	2.35	0.340	3.07

increase in the amount of SiC under the actual experimental conditions. Silicon carbide crystallizes in many polytypes differing from each other only in the stacking sequence. The two most common SiC polytypes are the 3C-SiC with cubic structure, and the 2H-SiC with hexagonal structure (see section 2.3). The EXAFS oscillations are sensitive to the short range atomic order and all types have the same fine structure pattern. GIXRD was employed to have information on the crystallographic phase of the laser-induced SiC and the diffractogram of the sample irradiated 256 times in CH_4 is reported in Fig. 7.5, showing the formation of polycrystalline 3C-SiC (β-SiC). In glancing incidence geometry, the peak corresponding to the orientation of the single crystal is not observable. Nevertheless, the laser melting leads to the formation of a polycrystalline Si layer and therefore all Si

peaks become visible. The EXAFS analysis revealed also the influence of the meandering

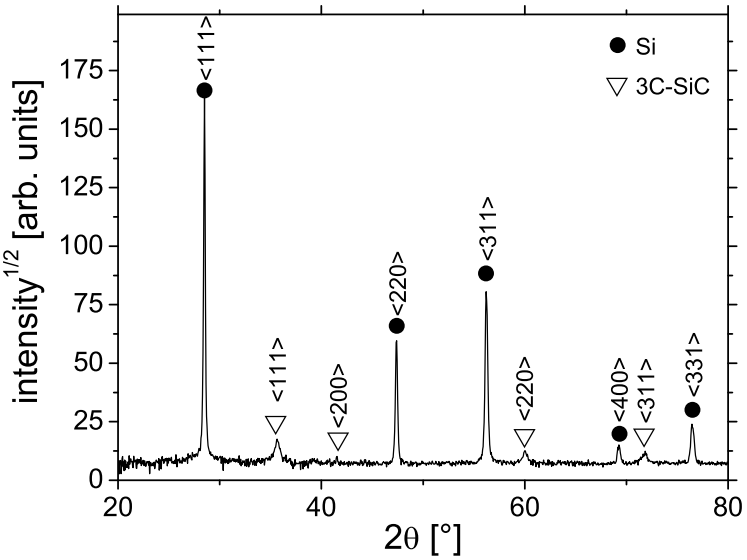

Figure 7.5: 2° GIXRD diffractogram of the Si sample irradiated in CH_4 with 256 pulses: (▽) cubic SiC, (•) polycrystalline Si.

treatment on the transport mechanism of carbon. As reported in Fig. 7.6, the intensities of the carbide peaks in the sample meandered with the 16×16 spot overlap are higher compared to the intensities in the sample treated under identical conditions but as single spot with 256 laser pulses. The carbon depth profiles extracted from the RBS analysis of these two samples are reported in the inset of Fig. 7.6, showing that the carbon contents on the surface are consistent with the EXAFS observations and indicating that the single spot treatment leads to more homogeneous concentration profiles compared to the meandering scan. Nevertheless, to maximize the carbon content (and therefore the amount of SiC) the meander treatment seems to be more appropriate.

7.1.2 Influence of the methane pressure

To investigate the influence of the methane pressure on the carbon incorporation, 12×12 meander scans at the fixed laser fluence of 5 J/cm^2 in 0.5, 1 and 4 bar CH_4 have been performed. The FT of the corresponding EXAFS oscillations are reported in Fig. 7.7. The intensity of the Si peak increases with increasing ambient pressure, indicating that the relative amount of carbide is higher for lower methane pressure. A similar effect was observed also in the iron samples irradiated in CH_4, where a layer of amorphous carbon was formed at low methane pressure on the target surface (see Fig. 5.13). As already pointed out in section 5.2.2 this phenomenon might be correlated to the shielding effect of the ambient gas on the laser beam. The quantitative analysis of the EXAFS data has been performed fitting the back Fourier transform (BFT) of the first three shells, similarly to the procedure described in the previous section. The average SiC relative fraction vs.

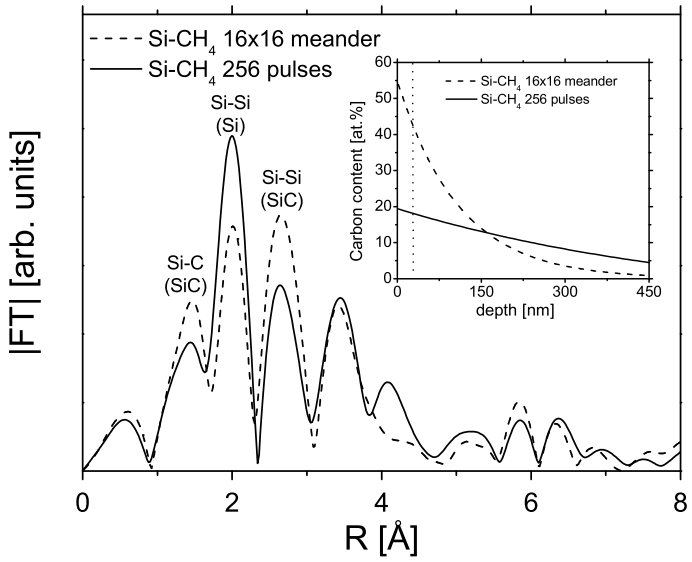

Figure 7.6: Fourier transform moduli of the samples irradiated in CH_4: single spot with 256 pulses (solid line) and 16×16 meander scan (dashed line). The inset show the corresponding carbon depth profiles measured by RBS. The vertical dotted line is the average information depth of the EXAFS in TEY mode ($\sim$ 30 nm).

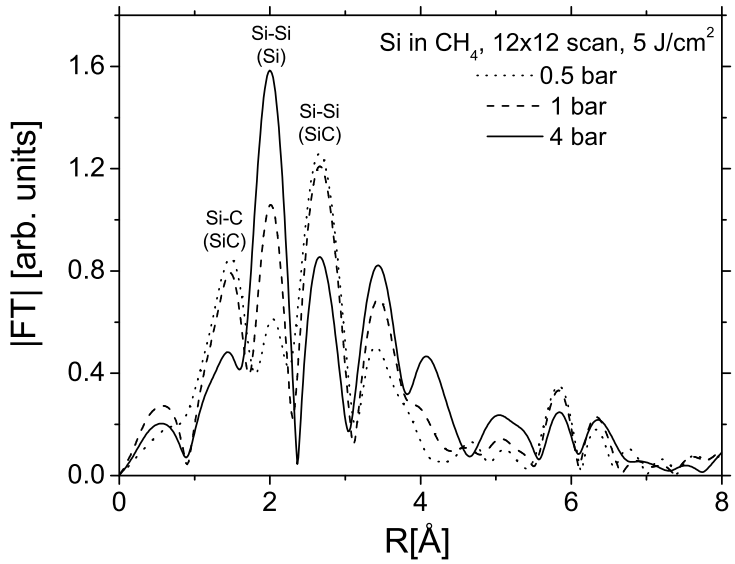

Figure 7.7: Fourier transform moduli of the Si samples meandered in 0.5 bar (dotted line), 1 bar (dashed line) and 4 bar (solid line) CH_4.

the methane pressure is reported in Fig. 7.8. At 0.5 bar CH_4 the carbide fraction is about 65%, decreasing to less than 30% at 4 bar. Besides, the carbon depth profiles measured

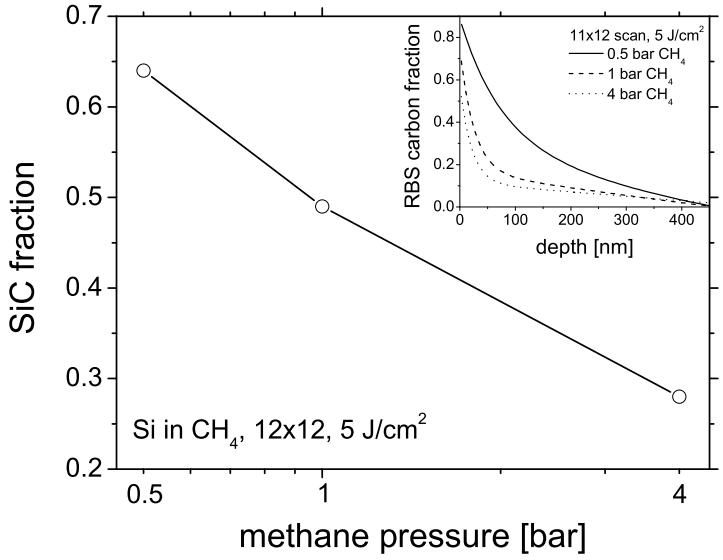

Figure 7.8: SiC phase fraction vs. the methane gas pressure as obtained from the EXAFS analysis. The inset reports the corresponding carbon depth profiles.

by RBS (see inset in Fig. 7.8) revealed that at the lowest methane pressure, the most effective carbon incorporation is achieved. Even if a pure and homogeneous SiC layer is not obtained, these results suggest that the optimal conditions to form SiC by irradiating Si in methane gas are: (i) a number of pulses/spot overlap not lower than 100 and (ii) an ambient pressure not higher than 0.5 bar.

7.2 Laser irradiation in nitrogen atmosphere

In the next sections, the results of the silicon irradiation in nitrogen atmosphere will be reported. Special emphasis will be given to the mass transport mechanisms during the single spot and the meandering treatments, revealing how the mass segregation can affect the nitrogen migration.

7.2.1 Influence of the number of pulses

The raw beam laser treatment has been performed in 1 bar N_2 at the fluence of 5 J/cm^2, ranging the number of pulses between 2 and 256. The FT of the Si sample irradiated 256 times is reported in Fig. 7.9 with the FT of the virgin Si and the α-Si_3N_4 standard. The laser-irradiated sample reveals all the peaks belonging to the Si structure, but only the first shell of the Si nitride phase is observable, suggesting that the nitride is highly disordered or amorphous (the poor crystallinity of the nitride phase was confirmed by XRD, where only the peaks of polycrystalline Si have been observed). The BFT procedure was performed in the region 0.86 Å $< R <$ 2.46 Å including the peaks corresponding to

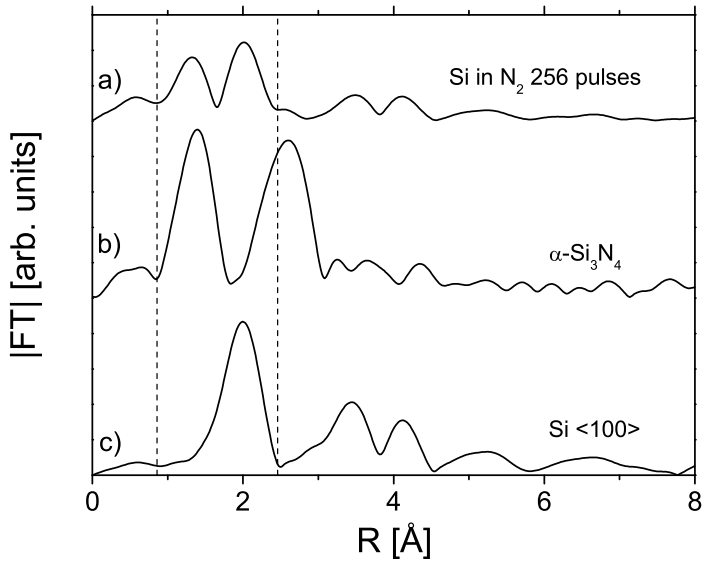

Figure 7.9: Fourier transform moduli of: a) Si sample irradiated in N_2 with 256 pulses, b) α-Si_3N_4 standard, c) virgin Si <100>. The dashed vertical lines delimit the BFT region.

the first shell of the Si_3N_4 system (N scatterer, peak at ∼1.35 Å) and the first shell of Si (peak at ∼2.05 Å). As for the SiC analysis, the scattering amplitudes and the phases of each shell were obtained from the standard samples (the virgin Si and the α-Si_3N_4 powder) and loaded in the fits as initial parameters. Since the absorption edges of Si and Si_3N_4 differ by 4 eV (1839 eV and 1843 eV, respectively), this energy correction has been introduced as a fixed parameter in the fitting procedure of the first shell of Si_3N_4. The oscillations extrapolated from the BFT of the silicon sample irradiated with 256 laser shots are shown in Fig. 7.10. The disorder parameter $\Delta\sigma^2$ (relative to the standard) of the Si shell was found to be less than 4×10^{-4} Å^2, but the average value of 2.8×10^{-3} Å^2 has been obtained for the Si_3N_4 shell, indicating a larger degree of disorder in the laser-synthesized nitride. The number of neighbors were normalized with respect to the ideal values of the pure phases, in order to evaluate the phase ratios. There are four N neighbors in the first shell of Si_3N_4 in a distorted tetrahedral configuration, at a distance of 1.7 Å-1.8 Å, according to the kind of polymorph [125, 126]. The radius of the first nitride shell obtained from the BFT fitting is consistent with the value of the α-Si_3N_4 phase, and the coordination numbers of both the Si and the Si_3N_4 shells have been used to evaluate the Si_3N_4 fraction with a procedure analogous to the one used for the SiC samples. The results of the pulse series are shown in Fig. 7.11 and summarized in Table 7.2. It should be noticed that the relative amount of the nitride phase saturates after few laser shots to values between 40% and 50%. As it will be shown is the next section, this feature is in qualitative agreement with the RNRA observation, where a sharp nitrogen peak can be observed even after only 4 laser shots (see Fig. 7.13). The nitrogen depth profiling revealed the strong influence of the meandering treatment on the mass transport. Opposite to the case of SiC, as reported in the inset of Fig. 7.12, the nitrogen content *on the surface* of the sample meandered with 16×16 spot overlap is almost half

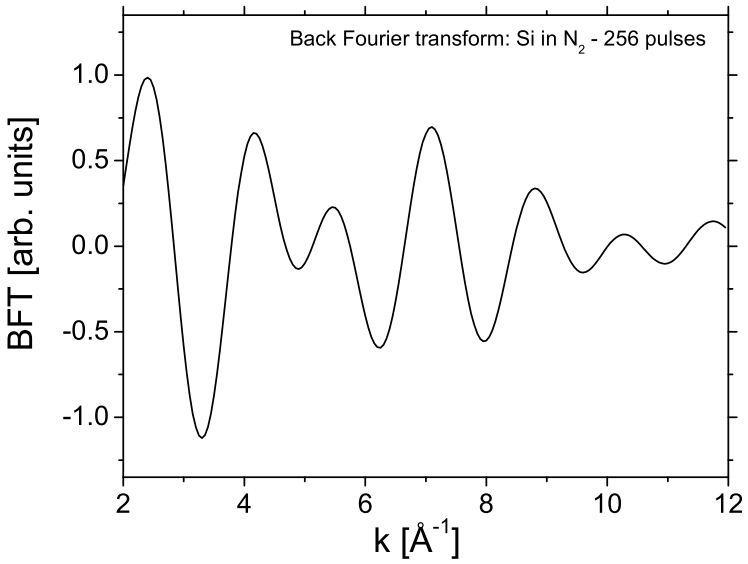

Figure 7.10: Back Fourier transform oscillations of the Si sample irradiated with 256 laser pulses in 1 bar N_2.

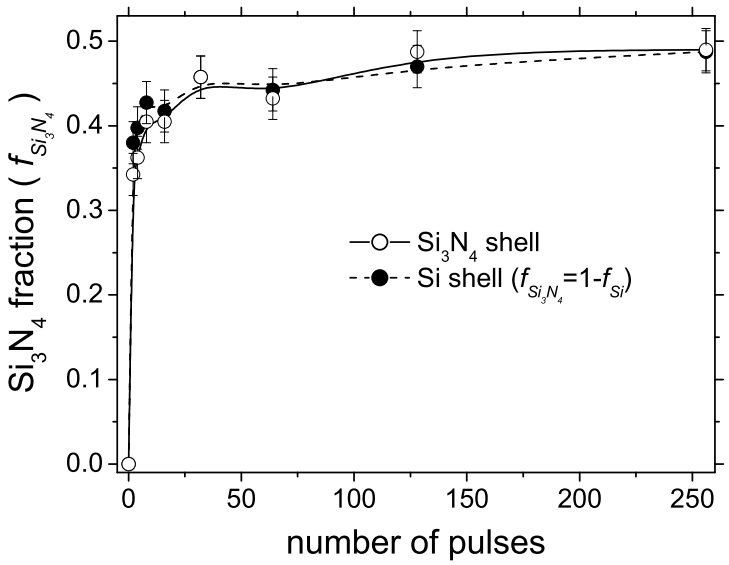

Figure 7.11: Si_3N_4 phase fraction obtained from the EXAFS analysis as function of the number of laser pulses: (○) first shell of Si_3N_4, (●) first shell of Si.

compared to the amount of nitrogen in the sample treated under identical conditions but as a single spot with 256 laser pulses. This is in qualitative agreement with the intensity ratio of the Si and the Si_3N_4 peaks obtained from the FT of the EXAFS data, as reported in Fig. 7.12. The sharp nitride surface peak (∼20 nm thick) obtained with the single spot

Table 7.2: Two-shells fitting for the Si samples irradiated in N_2: summary of the results.

Laser shots	Si-N (I shell)		Si (I shell)	
	N/4	R[Å]	N/4	R[Å]
2	0.343	1.73	0.620	2.35
4	0.363	1.72	0.603	2.35
8	0.405	1.72	0.573	2.35
16	0.405	1.73	0.583	2.36
32	0.458	1.73	0.543	2.36
64	0.433	1.73	0.558	2.36
128	0.488	1.73	0.530	2.36
256	0.490	1.73	0.513	2.35

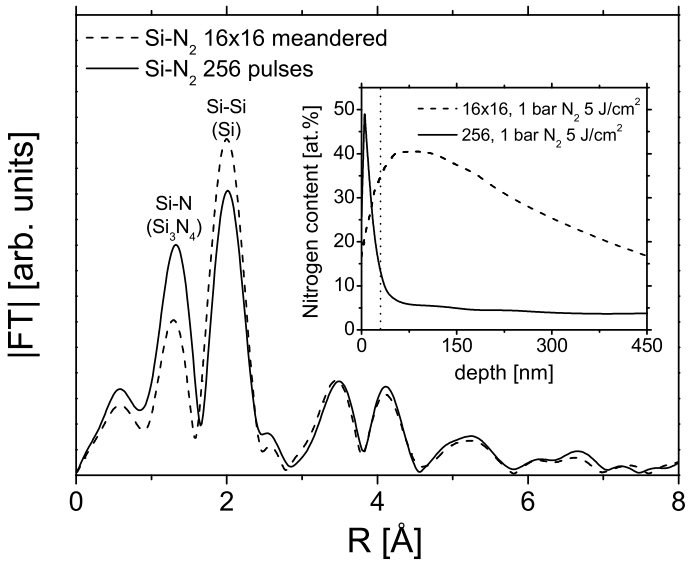

Figure 7.12: Fourier transform moduli of the samples irradiated in N_2: single spot with 256 pulses (solid line) and the 16×16 scan (dashed line). The inset show the corresponding nitrogen depth profiles measured by RNRA. The vertical dotted line is the average information depth of the EXAFS in TEY mode (∼30 nm).

treatment is attributed to the strong segregation of nitrogen in Si during the cooling of the substrate. The meandering treatment performed under the same experimental conditions enhances the migration of nitrogen to larger depth, nevertheless the EXAFS oscillations of the sample treated as single spot and the meandered one have similar features, revealing only the first shell of the Si_3N_4 and all peaks of Si. This suggests that the different mechanism of nitrogen migration does not lead to a different crystallization of the nitride phase. The complete absence of the second shell of Si_3N_4 in the laser nitrided samples suggests an alternative explanation of the EXAFS results. As reported by various authors [127, 128, 129], nitrogen in silicon is known to exist mostly in molecular form. Theoretical

calculations confirmed by experimental evidence have shown that the nitrogen-pair defect can be present in the ideal Si structure forming Si-N bonds with length of 1.7 Å-1.8 Å. In such a case, the EXAFS oscillations would have the contributions from the N scatterers with a shell radius of 1.7 Å-1.8 Å and the contributions from all the shells of Si. Since the Si structure is not strongly affected by the nitrogen pair [127], the coordination number of the first Si shell should be four-fold (i.e. the ideal value). Nevertheless, the FT of the laser irradiated samples reveals a clear decrease of the number of Si neighbors, suggesting the presence of vacancies (V). The existence of the vacancy-nitrogen complex has been extensively studied [129, 130, 131], demonstrating that the configuration N_2-V_2 is more stable than the nitrogen-pair defect with a theoretical Si-N bond of length $\sim$ 1.8 Å.

7.2.2 The segregation problem

With the single spot treatment in nitrogen atmosphere, the nitride layer has a thickness of only a few tens of nanometers. As already mentioned in the previous section, the fact that the nitrogen does not diffuse deeper into the silicon matrix is attributed to segregation. This phenomenon occurs when the impurities (in this case N) are rejected by the advancing solid/liquid interface in the phase characterized by the higher solubility, i.e. the liquid, and then accumulate at the sample surface [132, 133]. A clear indication of the segregation phenomenon is reported in Fig. 7.13. The nitrogen depth profiles measured by RNRA for various number of laser shots show the same characteristic surface peak and very little nitrogen remains inside the sample. Even if during the laser melting some nitrogen diffuses in the liquid silicon, as the solid/liquid interface recedes toward the surface, the nitrogen "jumps" from the solidified portion into the liquid layer, eventually accumulating on the target surface. The analytical description of the segregation process assumes that the redistribution of impurities is governed by the diffusion equation [133]:

$$\frac{\partial C}{\partial t} = \frac{\partial}{\partial z}\left(D\frac{\partial C}{\partial z}\right), \tag{7.1}$$

where D is the diffusion constant and C is the impurity concentration. The boundary conditions are a reflecting surface:

$$\left.\frac{\partial C}{\partial z}\right|_{z=0} = 0, \tag{7.2}$$

and a moving solid/liquid interface that rejects the impurities in the liquid:

$$\left. D\frac{\partial C}{\partial z} + (1-K)v_{sl}C\right|_{z_i} = 0, \tag{7.3}$$

with v_{sl} being the solid/liquid interface velocity and z_i its instantaneous position. The segregation coefficient:

$$K = \left.\frac{C_s}{C_l}\right|_{z_i} < 1 \tag{7.4}$$

is the solubility ratio at the interface (C_s and C_l are the impurities concentrations in the solid and the liquid, respectively). Eqs. (7.1) to (7.4) can be solved analytically [134],

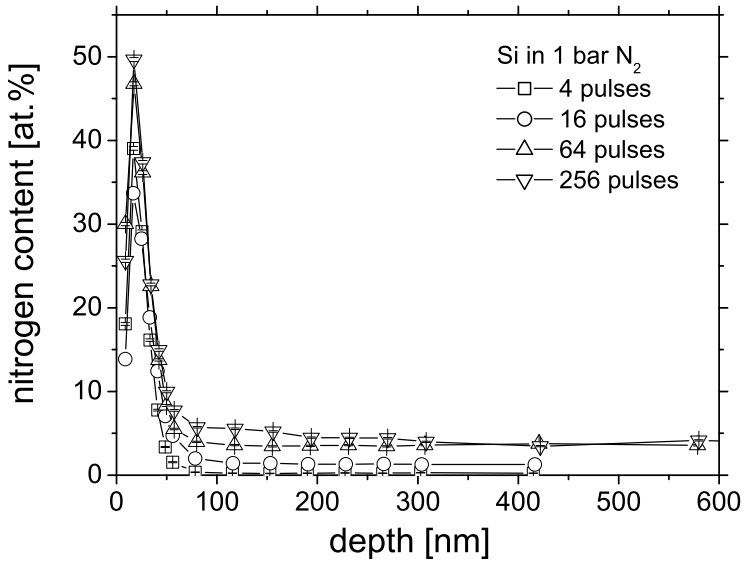

Figure 7.13: RNRA nitrogen depth profiles of Si treated as single spot with laser fluence of 5 J/cm^2 in 1 bar N_2 and various number of pulses.

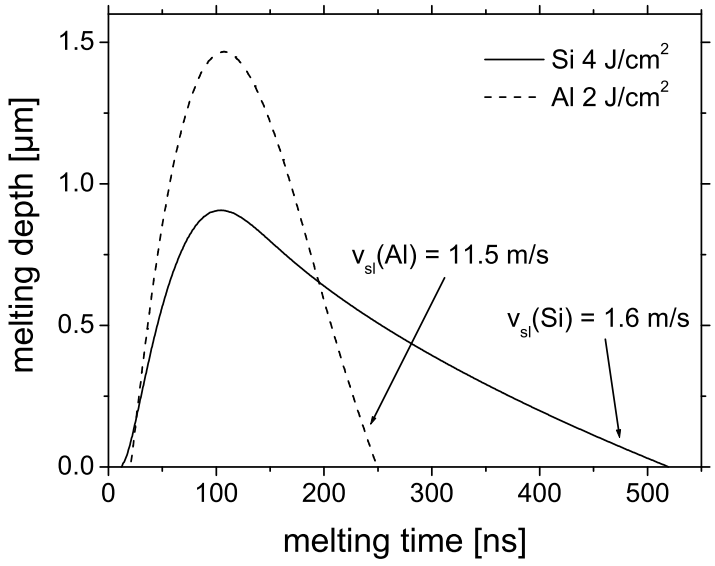

Figure 7.14: The melting depths vs. melting times of a Si substrate irradiated at 4 J/cm^2 and an Al substrate irradiated at 2 J/cm^2: the interface velocity v_{sl} is the slope of the curve calculated where indicated by the arrows.

revealing the strong influence of the interface velocity on the segregation effect. In particular, small values of v_{sl} enhance the surface accumulation of the impurities, provided that the segregation coefficient is small enough ($K < 0.1$). The segregation of several

dopants in silicon after pulsed laser irradiation has been extensively studied (see [132] and references therein), but unfortunately no data are available on the segregation of N in Si. As a further proof, Fig. 7.14 reports the comparison between the solid/liquid interface velocities of the Al substrate irradiated at 2 J/cm^2 and the Si substrate irradiated at 4 J/cm^2. The difference is almost one order of magnitude (v_{sl}(Al)=11.5 m/s, v_{sl}(Si)=1.6 m/s), indicating that in the semiconductor the segregation is more effective. A possible way to avoid the accumulation of N on the target surface is the meander scan. As already pointed out in Fig. 7.12, opposite to the single spot treatment, the meandering scan allows the migration of N (or Si_3N_4) to larger depth. In this case the origin of the nitrogen depth profiles is correlated to the strong convection induced by the piston effect [3, 28] at the edge of the laser spot: as schematically illustrated in Fig. 7.15, even if the

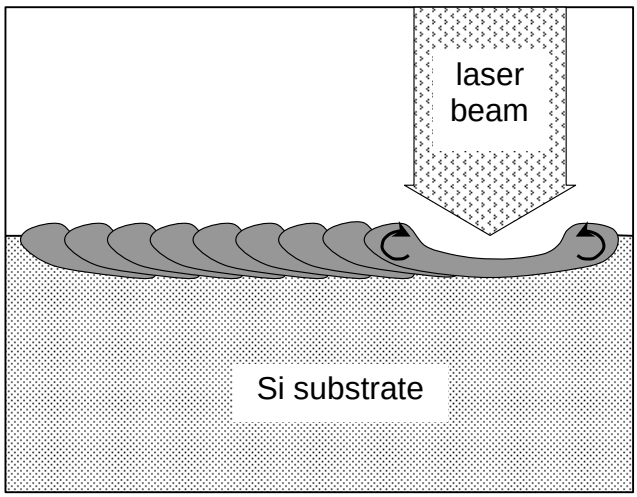

Figure 7.15: Sketch of the mass transport mechanism during the meander treatment with the raw laser beam: the convection due to the piston effect is indicated by the arrows.

segregation is present, it should interest mainly the center of the laser spot, while at the borders of the irradiated area, the mass transport should be dominated by convection. The meandering scan leads to an inevitable overlap of the laser spot borders, and the segregation effect is "masked" by the mass convection. The RNRA nitrogen profiles of the samples irradiated with the 16 × 16 scan in 1 bar N_2 at different laser fluences are reported in Fig. 7.16. Apart the very surface (within 50 nm), these depth profiles resemble the carbon profiles obtained under similar experimental conditions (meander scans with analogous laser fluence and gas pressures, see insets in Figs. 7.6 and 7.8). For a laser fluence below 3 J/cm^2 the nitriding efficiency is quite poor, but the threshold rises to 4 J/cm^2 if the homogenized beam is used. This difference is caused by the inhomogeneity of the raw beam intensity distribution: the *average* fluence is 3 J/cm^2, but the fluctuations can be as large as ±1 J/cm^2 over the laser spot. A concluding remark concerns the carbon incorporation into silicon. According to the EXAFS and the RBS analyses, the carbon does not form any sharp surface peak on the silicon surface and migrates to large depth during the single spot treatment, suggesting that the segregation is absent. As pointed out in section 2.3 the carbon atoms dissolve substitutionally in Si forming SiC, and not interstitially like nitrogen. Therefore, the impurities (C atoms) in such a case form a stable phase and they do not jump from the solid to the liquid as the interface

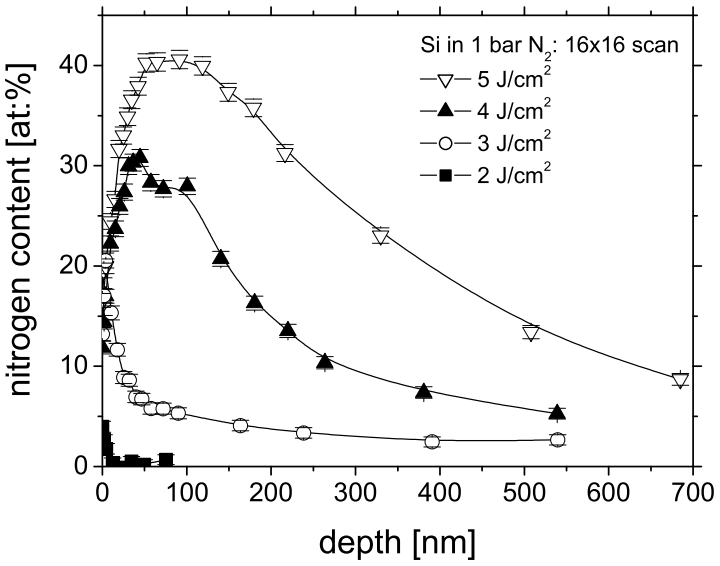

Figure 7.16: RNRA nitrogen depth profiles of the Si samples meandered with the 16×16 scan at various laser fluences (from 2 J/cm^2 to 5 J/cm^5).

moves toward the target surface.

Chapter 8

Conclusions and outlooks

The laser processing of iron, aluminum and silicon substrates in nitrogen and methane atmospheres has been the subject of this work. The mass transport mechanisms during the laser irradiation in nitrogen gas have been studied in detailed, revealing the following facts:

(i) the mobility of nitrogen inside the iron matrix can be attributed to diffusion in the liquid metal: thanks to the capability of the RNRA, the contribution of each laser pulse to the nitrogen incorporation and to the subsequent migration could be quantified, shedding light on the nitrogen incorporation mechanism and its relation with the phenomena occurring inside the target (temperature, melting time, melting depth) and on the target surface (plasma formation). Besides, the nitrogen losses due to the degassing and to the ablation effects could be revealed;

(ii) nitrogen can be efficiently incorporated in the aluminum matrix, if the excimer laser fluence exceeds 2 J/cm^2; the nitrogen transport mechanism is strongly related to the local temperature induced by the absorbed laser energy: when the irradiated sample is heated above the melting/dissociation point of AlN ($\sim$ 3000 K), atomic nitrogen can rapidly migrate in the liquid metal, forming homogeneous depth concentrations that are a direct consequence of two competing contributions: an inward flux due to the nitrogen incorporation and an outward flux due to the nitrogen outgassing; the quantification of the nitrogen content as a function of the number of laser shots and the nitrogen gas pressure has been successfully obtained. It should be mentioned that after 256 pulses in 6 bar nitrogen gas, a homogeneous AlN layer is formed. When the temperature of the irradiated sample is above the melting point of Al, but not high enough to dissociate the AlN ($\sim$ 2000 K), the latter (and not the atomic nitrogen) drifts in the molten aluminum layer due to the driving forces induced by the Brownian motion and the thermophoresis, which in turn are related to the chemical and the thermal gradients, respectively. The mechanical properties of the nitrided samples revealed a considerable increase of the surface hardness, closely correlated to the nitrogen content;

(iii) the nitrogen incorporation in the silicon substrates is strongly affected by the chemical and physical properties of the elements involved in the process. During the single spot irradiation, the segregation effect hinders the migration of nitrogen which instead accumulates on the surface of the target. The laser nitriding process becomes more efficient if

the meandering scan is employed. In this case the nitrogen/nitride transport mechanism is attributed to the mass convection induced by the piston effect. The poor crystallinity of the laser-synthesized silicon nitride and the results of the EXAFS analysis suggest the formation of the nitrogen-vacancy complex $N_2{-}V_2$.

The laser treatment in methane atmosphere has been investigated here for the first time. The attention has been focused on the structural modifications induced by the laser irradiation, and the results can be summarized as follows:

(i) the carbon incorporation in iron is effective: the phase evolution as a function of the methane pressure and the laser scan has been investigated in detail with Mössbauer spectroscopy and X-ray diffraction. At a laser fluence of 4 J/cm^2, with intermediate methane pressures (few bar) and moderate spot overlap ($\leq 11{\times}12$) a mixture of γ-Fe(C), ϵ phase and cementite (θ-Fe_3C) is obtained. Increasing the gas pressure or the meander overlap produces equivalent effects, leading to the formation of a homogeneous cementite layer, as revealed by all analytical techniques. The synthesis of θ-Fe_3C layers is technologically a rather important result: this phase is typically embedded in the metal matrix and it is hard to obtain as a single phase. Nanoindentation measurements revealed that the mechanical properties of the carburized layer are largely enhanced by the laser process;

(ii) carbon can be incorporated also in the aluminum matrix, forming amorphous aluminum carbide (a-Al_4C_3); the crystallization of the carbide phase is most probably hindered by the strong thermal gradients produced during the laser treatment. Nevertheless a considerable amount of carbon ($\sim$20 at.%) and a good increase of the surface hardness have been observed;

(iii) by irradiating silicon substrates in methane atmosphere, the formation of polycrystalline, cubic silicon carbide (β-SiC) with good degree of crystallinity has been successfully achieved, as indicated by the EXAFS results. The strong influence of the laser scan (single spot or meandering) on the carbon migration has been revealed. The surface carbon concentration is higher, if the meandering treatment is employed, but the carbon profiles are more homogeneous after single spot irradiations. Opposite to the treatment in nitrogen gas, no mass segregation has been observed, and the intriguing fact that the carbon incorporation is more effective at lower methane pressure indicates the important role of the gas pressure on the carburizing efficiency. It should be mentioned that the carbide phase is mixed with the non-reacted silicon matrix, and the optimization of the laser process aims to the maximization of the SiC relative fraction.

The detailed investigation of the carbon transport mechanism in the irradiated targets requires the use of RNRA with the $^{13}C(p,\gamma)^{14}N$ nuclear reaction at resonance energy $E_r = 1748$ keV. For this purpose, the capability of the 3 MeV Pelletron accelerator facility at the Zweites Physikalisches Institut in Göttingen should considerably increase the investigative power. This is considered one of the primary tasks for the future investigation of the laser carburazing process. Understanding the mass transport during the laser irradiation, should give important hints on the the carbon incorporation mechanism. The results of the present work also reveal the fundamental role of the phenomena occurring on the surface of the irradiated target. The vaporization of the substrate, the ionization of the ambient gas and the formation of a plasma have been predicted theoretically, but their direct observation has not been carried out yet. The investigation and characterization of these phenomena is not straightforward and requires complex experiments. For this reason, *in*

situ, time-resolved analyses by means of optical, UV and X-ray spectroscopy have been planned, in order to shed light on the plasma-vapor interaction with the substrate. On the other hand, the influence of other experimental parameters such as the duration and wavelength of the laser pulse and the use of alternative gaseous atmospheres (NH_3 instead of N_2, C_2H_2 instead of CH_4) are currently under investigation.

Acknowledgements

I'm deeply grateful to PD Dr. Peter Schaaf for his constant and unexhaustable help, and I truly thank him for the big scientific freedom he always provided, without which most of this work would not exist.

I'm also in debt to Prof. Dr. Klaus-Peter Lieb for his continuous interest and support to this topic.

I address my thanks to the former members of the group, Felix Landry, Meng Han and Steffen Wagner for their valuable help in the experimental work and for the nice atmosphere they created inside the group.

Marcus Schwickert and Felix Harbsmeier are gratefully acknowledged for being excellent officemates and good beer-drinkers. I'm in dept to Felix for introducing me to the IONAS setup and to Marcus for the numerous evening we spent in the office, working, simulating, analyzing and, lately, writing.

Many thanks to Alexander Müller and Sankar Dhar for their help and for the fruitful discussions: Sankar and his wife are gratefully acknowledged for the excellent "spicy dinner" they are capable of.

I'm grateful to the Herwig Schultz, Klaus Arndt, head of the fine mechanics workshop, Kurt Schemmerling, head of the electronic workshop, and all their coworkers for the efficient, competent and prompt job. Many thanks to Detlef Purschke for operating the IONAS facility and to Dr. Lüder Ziegler for the handling of the Mössbauer radioactive sources.

I'm in debt to Dr. Guido Schmitz from the Institut für Materialphysik in Göttingen for the preparation and the Transmission Electron Microscopy observation of the AlN samples. Dieter Plischke is gratefully acknowledged for operating the Scanning Electron Microscopy and for his patience during the experimental observations.

I'm obliged to Dr. Nikita Arnold from Linz University for the interesting and fruitful discussion concerning the laser interaction with matter and the diffusion problem. Many thanks also to Prof. Dr. Andreas Emmel from the Fachhochschule Amberg-Weiden for the nice suggestions about the laser nitriding of aluminum.

Frau Christa Wohlfahrt and Lucie Hamdi are kindly acknowledged for their continuous help with all the small and big administrative problems that a foreigner always has in a foreign country.

Dr. Anne-Marie Flank, Dr. Pierre Lagarde and Dr. Agnes Traverse are acknowledged for their assistance at the L.U.R.E. (Orsay) during our XAFS beamtime and for the illuminating advice concerning the data analysis.

My sincere thanks to all the members of the Zweites Physikalisches Institut in Göttingen, who always make the working atmosphere enjoyable and relaxed with extra-time activities (barbecues, kicker-table competitions, outdoor trips).

Finally, my thoughts inevitably go to my parents, my family and to all those persons who always, critically, constructively supported my choices and my work. To them I address my deepest gratitude and the best wishes for a brilliant continuation.

Göttingen, september 2002

Bibliography

[1] A. Sona, in *Applied Laser Tooling*, edited by O. D. D. Soares and M. Perez-Amor (M. Nijhoff, Dordrecht, 1987).

[2] E. V. Locke and R. A. Hella, IEEE J. **10**, 179 (1974).

[3] M. von Allmen and A. Blatter, *Laser-Beam Interactions with Materials* (Springer-Verlag, Berlin, 1998).

[4] W. M. Steen, *Laser Material Processing* (Springer, Berlin, 1998).

[5] D. Bäuerle, *Laser Processing and Chemistry* (Springer-Verlag, Heidelberg, 2000).

[6] H. K. Tönshoff *et al.*, Int. J. Elect. Machining **4**, 1 (1999).

[7] S. Küper and M. Stuke, Microelect. Eng. **9**, 475 (1989).

[8] M. Hegelich *et al.*, Phys. Rev. Lett. **89**, 0850021 (2002).

[9] *Physical Metallurgy*, edited by R. W. Cahn and P. Haasen (North-Holland, Amsterdam, 1983).

[10] E. Lehrer, Z. Electrochem. **36**, 383 (1930).

[11] T. Fujii, K. Yoshida, K. Suzuki, and S. Ito, Solid State Ionics **141-142**, 593 (2001).

[12] K. Tanihata and Y. Miyamoto, Int. J. Self Propagating Heat Temperature Synthesis **7**, 209 (1998).

[13] H. J. Kim and Y. G. Kweon, Wear **174**, 201 (1994).

[14] M. H. Jacobs and Y. G. Kweon, Materials and Design **14**, 33 (1993).

[15] A. L. Thomann *et al.*, J. Appl. Phys. **80**, 4673 (1996).

[16] S.-M. Oh and D.-W. Park, Thin Solid Films **319**, 189 (1998).

[17] M. Yan, J. Yan, and T. Bell, Modelling Simul. Mat. Sci. Eng. **8**, 491 (2000).

[18] V. I. Dimitrov *et al.*, Comput. Mat. Sci. **15**, 22 (1999).

[19] Y. Sun and T. Bell, Mat. Sci. Eng. **A224**, 33 (1997).

[20] E. D. Cabanillas, J. Desimoni, G. Punte, and R. C. Mercader, Mat. Sci. Eng. **A279**, 133 (2000).

[21] K. C. Walters, J. Vac. Sci. Technol. **B12**, 945 (1994).

[22] T. Reier, J. W. Schultze, W. Österle, and C. Buchal, Thin Solid Films **385**, 29 (2001).

[23] T. Telbizova *et al.*, Appl. Phys. Lett. **76**, 1404 (2000).

[24] E. C. Moreira, M. Behar, and L. Amaral, Nucl. Instr. and Methods **B148**, 836 (1999).

[25] J. Jagielski and M. Kopcewicz, J. Appl. Phys. **88**, 673 (2000).

[26] A. Königer, C. Hammerl, M. Zeitler, and B. Rauschenbach, Phys. Rev. **B55**, 8143 (1997).

[27] E. C. Paloura, C. Lioutas, and A. Markwitz, J. Appl. Phys. **80**, 2720 (1996).

[28] C. Illgner, *Untersuchungen zum Lasernitrieren von Eisen* (Cuvillier Verlag, Göttingen, 1996), doctoral thesis.

[29] F. Landry, *Lasernitrieren von Armco-Eisen und Eisenwerkstoffen* (Cuvillier Verlag, Göttingen, 1999), doctoral thesis.

[30] M. Han, *Laser nitriding of metals* (http://webdoc.sub.gwdg.de/diss/2002/han/han.pdf, Göttingen, 2001), doctoral thesis.

[31] P. Schaaf, Prog. Mat. Sci. **47**, 1 (2002).

[32] *Thin Solid Films*, edited by J. Kossut (Elsevier Science, The Netherlands, 2002), Vol. 412.

[33] *Surface and Coatings Technology*, edited by H. Bangert *et al.* (Elsevier Science, The Netherlands, 2002), Vol. 151-152.

[34] *Surface and Coatings Technology*, edited by B. Sartwell (Elsevier Science, The Netherlands, 2001), Vol. 140.

[35] *Surface and Coatings Technology*, edited by C. Mitterer *et al.* (Elsevier Science, The Netherlands, 2001), Vol. 146-147.

[36] *Thin Solid Films*, edited by H. Hosono, N. Ichinose, and Y. Shigesato (Elsevier Science, The Netherlands, 2002), Vol. 411.

[37] *Thin Solid Films*, edited by A. Slauoi, J. Poortmans, A. Jager-Waldau, and C. Brabec (Elsevier Science, The Netherlands, 2002), Vol. 403-404.

[38] *Binary Alloy Phase Diagrams*, edited by H. O. T .B. Massalski, P. R. Subramanian, and L. Kacprzak (ASM International, Ohio, 1996).

[39] M. Ron, in *Applications of Mössbauer Spectroscopy II*, edited by R. L. Cohen (Academic Press, New York, 1980).

[40] J. Häglung, G. Grimvall, and T. Jarlborg, Phys. Rev. **B44**, 2914 (1991).

[41] S. J. Li *et al.*, Thin Solid Films **316**, 100 (1998).

[42] J. Kunze, *Nitrogen and Carbon in Iron and Steel, Physical Research* (Akademie-Verlag, Berlin, 1990), Vol. 16.

[43] *Handbook of Chemistry and Physics*, edited by R. C. Weast and M. J. Astle (CRC Press, Boca Raton, 1983).

[44] *Powder Diffraction File database PDF-2* (International Centre for Diffraction Data, Newton Square, 1997).

[45] H. A. Wriedt, N. A. Gokcen, and R. H. Nafziger, in *Binary Alloy Phase Diagrams*, edited by T. B. Massalski, H. Okamoto, P. R. Subramanian, and L. Kacprzak (ASM International, Ohio, 1996).

[46] H. Okamoto, J. Phase Eq. **13**, 2 (1992).

[47] L. F. Mondolfo, *Aluminum Alloys: Structure and Properties* (Butterworth, London, 1976).

[48] L. G. D'yachkov, L. A. Zhilyakov, and A. V. Kostanovskiĭ, Thecnical Physics **45**, 115 (2000).

[49] D. P. Dandekar, A. Abbate, and J. Frankel, J. Appl. Phys. **76**, 4077 (1994).

[50] Goodfellow Metal Ltd., www.goodfellow.com.

[51] S. Strite and H. Morkoç, J. Vac. Sci. Technol. **B10**, 1237 (1992).

[52] H. Morkoç *et al.*, J. Appl. Phys. **76**, 1363 (1994).

[53] N. W. Ashcroft and N. D. Mermin, *Solid State Physics* (Saunders Company, Philadelphia, 1976).

[54] A. Zerr *et al.*, Nature **400**, 340 (1999).

[55] S. Fähler and H. U. Krebs, Appl. Surf. Sci. **96-98**, 61 (1996).

[56] J. Crank, *The Mathematics of Diffusion* (Clarendon Press, Oxford, 1975).

[57] C. A. J. Fletcher, *Computational Techniques for Fluid Dynamic 1* (Springer, Berlin, 1988).

[58] *Thermophysical Properties of Matter*, edited by Y. S. Touloukian and C. Y. Ho (Plenum, New York, 1970), Vol. 1 and 4.

[59] S. Higashi and T. Sameshima, Jpn. J. Appl. Phys. **40**, 480 (2001).

[60] M. Hatano *et al.*, J. Appl. Phys. **87**, 36 (2001).

[61] S. I. Anisimov and V. A. Khokhlov, *Instabilities in Laser-Matter Interactions* (CRC Press, Boca Raton, 1995).

[62] S. I. Anisimov, Sov. Phys. JETP **27**, 182 (1968).

[63] Y. P. Raizer, Sov. Phys. JEPT **21**, 1009 (1965).

[64] Y. P. Raizer, Sov. Phys. JEPT **31**, 1148 (1970).

[65] A. Pirri, Phys. Fluids **16**, 1435 (1973).

[66] A. A. Boni and F. Y. Su, Phys. Fluids **17**, 340 (1974).

[67] Y. P. Raizer, Sov. Phys. Usp. **23**, 789 (1980).

[68] Y. P. Raizer, Sov. Phys. Quantum Electron. **14**, 40 (1984).

[69] M. Uhrmacher *et al.*, Nucl. Instr. and Methods **B9**, 234 (1985).

[70] J. A. Leavitt and J. L. C. McIntyre, in *Handbook of Modern Ion Beam Materials Analysis*, edited by J. R. Tesmer and M. Nastasi (Material Research Society, Pittsburgh, 1995).

[71] W. H. Bragg and R. Kleeman, Philos. Mag. **10**, 318 (1905).

[72] W.-K. Chu, J. W. Mayer, and M.-A. Nicolet, *Backscattering Spectrometry* (Academic Press, Orlando, 1978).

[73] N. Bohr, Mat. Fys. Medd. Dan. Vid. Selsk. **18**, 8 (1948).

[74] J. Lindhard and M. Scharff, Mat. Fys. Medd. Dan. Vid. Selsk. **27**, 15 (1953).

[75] L. R. Doolittle, Nucl. Instr. and Methods **B9**, 344 (1985).

[76] T. Osipowicz, K. Lieb, and S. Brüssermann, Nucl. Instr. and Methods **B18**, 232 (1987).

[77] G. Schatz and A. Weidinger, *Nucleare Festkörperphysik* (Teubner, Stuttgart, 1992).

[78] *Handbook of Modern Ion Beam Materials Analysis*, edited by J. R. Tesmer and M. Nastasi (Material Research Society, Pittsburgh, 1995).

[79] N. N. Greenwood and T. C. Gibb, *Mössbauer Spectroscopy* (Chapman and Hall, London, 1971).

[80] R. L. Mössbauer, Z. Physik **151**, 124 (1958).

[81] R. L. Mössbauer, Naturwisseschaften **45**, 538 (1958).

[82] R. L. Mössbauer, Science **137**, 731 (1962).

[83] A. Abragam, *Principles of Nuclear Magnetism* (Clarendon Press, London, 1961).

[84] J. J. Spijkerman, in *The Mössbauer Effect Methodology*, edited by I. J. Gruverman (Plenum Press, New York, 1970), Vol. 7.

[85] F. E. Wagner, J. de Physique **37**, 673 (1976).

[86] J. J. Rehr and R. C. Albers, Rev. Mod. Phys. **72**, 621 (2000).

[87] D. E. Sayers and B. A. Bunker, in *X-Ray Absorption*, edited by D. C. Koningsberger and R. Prins (John Wiley and Sons, New York, 1988), Chap. 6.

[88] D. E. Sayers, E. A. Stern, and F. W. Lytle, Phys. Rev. Lett. **27**, 1204 (1971).

[89] A. L. Ankudinov, B. Ravel, J. J. Rehr, and S. D. Conradson, Phys. Rev. **B58**, 7565 (1998).

[90] W. T. Elam, J. P. Kirkland, R. A. Neiser, and P. D. Wolf, Phys. Rev. **B38**, 26 (1988).

[91] K. V. Klementev, VIPER for Windows, www.desy.de/∼klmn/viper.html.

[92] K. V. Klementev, J. Phys. D: Appl. Phys. **34**, 209 (2001).

[93] B. D. Cullity, *Elements of X-Ray Diffraction* (Addison-Wesley, Reading, 1978).

[94] H. M. Rietveld, Acta Cryst. **22**, 151 (1967).

[95] H. M. Rietveld, J. Appl. Cry. **2**, 65 (1969).

[96] J. R. Caravajal, FULLPROF, bali.saclay.cea.fr/pub/divers/fullp.

[97] R. A. Young, *The Rietveld Method* (Oxford University Press, Oxford, 1995).

[98] E. Carpene and P. Schaaf, Appl. Surf. Sci. **186**, 100 (2002).

[99] E. Carpene *et al.*, Appl. Surf. Sci **186**, 195 (2002).

[100] P. Schaaf, M. Han, K.-P. Lieb, and E. Carpene, Appl. Phys. Lett. **80**, 1091 (2002).

[101] E. Carpene, F. Landry, and P. Schaaf, Appl. Phys. Lett. **77**, 2412 (2000).

[102] E. Carpene and P. Schaaf, Appl. Phys. Lett. **80**, 891 (2002).

[103] E. Carpene, M. Kahle, M. Han, and P. Schaaf, in *Mössbauer Spectroscopy in Materials Science*, edited by M. Miglierini, M. Mashlan, and P. Schaaf (Kluwer Academic Publishers, Dordrecht, 2002), NATO Science Series "High Technologies", in print.

[104] P. Schaaf, F. Landry, and K. Lieb, Appl. Phys. Lett. **74**, 153 (1999).

[105] E. Fromm *et al.*, *Gases and Carbon in Metals* (Physik Daten FIZ Energie, Physik, Mathematik, Karlsruhe, 1982), Vol. XV.

[106] J. P. Reilly, A. Ballantyne, and J. A. Woodroffe, AIAA Journal **17**, 1098 (1979).

[107] C. Illgner *et al.*, J. Appl. Phys. **83**, 2907 (1998).

[108] G. J. Willems and H. E. Maes, J. Appl. Phys. **73**, 3256 (1993).

[109] Z. Mathalone, M. Ron, and H. Shechter, Appl. Phys. Lett. **17**, 32 (1970).

[110] B. Jönsson and S. Hogmark, Thin Solid Films **114**, 257 (1984).

[111] M. Han *et al.*, J. Appl. Phys. **89**, 4619 (2001).

[112] M. Ron and Z. Mathalone, Phys. Rev. **B4**, 774 (1971).

[113] J. Barnikel, *Nitrieren von Aluminiumwerkstoffen mit UV-Laserstrahlung* (Universität Erlangen-Nürnberg, Erlangen, 1998), doctoral thesis.

[114] E. Sicard, C. Boulmer-Leborgne, C. Andreazza-Vignolle, and M. Frainais, Appl. Phys. **A73**, 55 (2001).

[115] C. Boulmer-Leborgne *et al.*, Appl. Surf. Sci. **125**, 137 (1998).

[116] E. Carpene and P. Schaaf, Phys. Rev. **B65**, 224111 (2002).

[117] S. T. Picraux and D. M. Follstaedt, in *Surface Modifications and Alloying: Aluminium*, edited by J. M. Poate, G. Foti, and D. C. Jacobson (Plenum Press, New York, 1983).

[118] K. Huang, *Statistical Mechanics* (Wiley and Son, New York, 1987).

[119] A. I. Burshtein, *Introduction to Thermodynamics and Kinetic Theory of Matter* (Wiley and Son, New York, 1996).

[120] M. Sun, H. Geng, X. Bian, and Y. Liu, Mat. Sci. Forum **20**, 337 (2000).

[121] Y. I. Yalamov and A. S. Sanasaryan, Sov. Phys. Tech. Phys. **20**, 1351 (1976).

[122] E. R. Shchukin, Y. I. Yalamov, and O. A. Popov, Sov. Phys. Dokl. **32**, 898 (1987).

[123] W. R. L. Lambrecht and B. Segall, Phys. Rev. **B43**, 7070 (1991).

[124] E. Carpene, A. M. Flank, A. Traverse, and P. Schaaf, J. Phys. D: Appl. Phys. **35**, 1428 (2002).

[125] P. Yang, H.-K. Fun, I. Rahman, and M. I. Saleh, Ceram. Int. **21**, 137 (1995).

[126] H. Toraya, J. Appl. Cryst. **33**, 95 (2000).

[127] R. Jones, S. Öberg, F. B. Rasmussen, and B. B. Nielsen, Phys. Rev. Lett. **72**, 1882 (1994).

[128] V. V. Voronkov *et al.*, J. Appl. Phys. **89**, 4289 (2001).

[129] H. Sawada and K. Kawakami, Phys. Rev. **B62**, 1851 (2000).

[130] H. Kageshima, A. Taguchi, and K. Wada, J. Appl. Phys. **76**, 3718 (2000).

[131] K. Tanahashi, H. Harada, A. Koukitsu, and N. Inoue, J. Cryst. Growth **225**, 294 (2001).

[132] S. U. Campisano, Appl. Phys. **A30**, 195 (1983).

[133] P. Baeri and S. U. Campisano, in *Laser Annealing of Semiconductors*, edited by J. M. Poate and J. W. Mayer (Academic Press, New York, 1982).

[134] E. J. Yoffa, in *Laser and Electron Beam Processing of Materials*, edited by C. W. White and P. S. Peercy (Academic Press, New York, 1980).

Curriculum studiorum

Personal Data

- *name*: Ettore Carpene
- *birthplace*: Feltre (BL) - Italy
- *birthdate*: 22.01.1971
- *citizenship*: Italian

Education

- *1977-1985*: Elementary and Middle Schools (Italy)
- *1985-1990*: Scientific High School (Italy)
- *1990*: High School Diploma "Maturitá Scientifica"
- *1990-1996*: Physics studies at the University of Padova (Italy)
- *1996*: "Laurea" Degree in Physics
- *1997-1998*: Military Service
- *1998-1999*: Physics studies at the Old Dominion University in Norfolk, Virginia (USA)
- *1999*: Master's Degree of Science
- *1999-2002*: Physics PhD student at the II. Physikalisches Institut, University of Göttingen (Germany)

Teaching activities

- *1998-1999*: Teaching assistant at the Old Dominion University in Norfolk, Virginia (USA)
- *2002*: Fortgeschrittenenpraktikum at the II. Physikalisches Institut, University of Göttingen (Germany)